Quantifying and reducing the uncertainties in global contrail radiative forcing

by

Akshat Agarwal

B.A., M.Eng., University of Cambridge (2015)

Submitted to the Department of Aeronautics and Astronautics
in partial fulfillment of the requirements for the degree of
Doctor of Philosophy
at the
MASSACHUSETTS INSTITUTE OF TECHNOLOGY
September 2021

Author .....
Department of Aeronautics and Astronautics
4 June 2021

Certified by .....
Steven R. H. Barrett
Professor of Aeronautics and Astronautics
Chair, Thesis Committee and Supervisor

Certified by .....
Noelle E. Selin
Associate Professor, Institute for Data, Systems, and Society
Member, Thesis Committee

Certified by .....
Raymond L. Speth
Principal Research Scientist, Aeronautics and Astronautics
Member, Thesis Committee

Accepted by .....
Jonathan P. How
Professor of Aeronautics and Astronautics
Chair, Graduate Program Committee

Quantifying and reducing the uncertainties in global contrail radiative forcing

by

Akshat Agarwal

Submitted to the Department of Aeronautics and Astronautics
on 4 June 2021, in partial fulfillment of the
requirements for the degree of
Doctor of Philosophy

Abstract

Condensation trails, or contrails, are line-shaped ice clouds that form in the exhaust plume of aircraft engines under sufficiently cold and humid conditions. They can persist for several hours, growing to be indistinguishable from natural cirrus clouds. Numerical simulations of contrails (including contrail-cirrus) have estimated the global, annual average, net radiative forcing (RF) to be 50 mW/m^2 in 2011, representing 2.3% of the RF due to all anthropogenic emissions. However, these estimates are uncertain and model estimates vary by more than one order of magnitude. In this thesis, I address three major sources of uncertainty: the number of black carbon (BC) particles emitted by an engine, the accuracy of the meteorological datasets used for modeling contrails, and the approach to simulate the evolution of a contrail.

The number of BC particles emitted by an aircraft engine is required to estimate the number of crystals that form in a contrail. Decreasing the number of crystals that form by 80% could reduce the contrail RF by 50%. The first part of this thesis develops an approach to estimate the number of particles emitted by an engine. Using two complementary datasets, I relate smoke number measurements to the BC mass concentration, quantify losses in the measurement system, and connect mass emissions to particle number emissions. The method is applied to existing BC measurements achieving an R^2 of 0.80 and 0.82, respectively. Global BC emissions for all operations in 2015 were estimated to be 2.0 Gg/year (95% CI $= 1.7 - 2.3$) and 2.42×10^{26} particles/year (95% CI $= 1.58 - 3.81 \times 10^{26}$).

Contrail formation is sensitive to the background atmospheric conditions, specifically the temperature and humidity. These are estimated from reanalysis models that assimilate observations with numerical estimates of the atmosphere. Upper tropospheric water vapor has been found to be overestimated in multiple reanalyses, but the effect on the formation of persistent contrails has not been quantified. In the second part of this thesis, I quantify the error in predicting the formation of persistent contrails using two reanalysis models - ERA5 and MERRA-2. Using data from 793,044 radiosondes, persistent contrails forming at cruise altitudes in 30°N – 60°N are overestimated by factors of 2.0 and 3.5 for ERA5 and MERRA-2, respectively.

I also define the evaporation depth, which measures the depth to which a contrail can survive based on the available ice mass and is thus a measure of contrail lifetime. This metric is found to be overestimated by 17% in ERA5 and 45% in MERRA-2 suggesting the contrail lifetime is overestimated. Finally, the reanalyses incorrectly identify individual regions that could form persistent contrails 87% and 52% of the time, respectively. These results suggest that contrail models currently overestimate the number and lifetime of persistent contrails.

Global contrail models simulate contrail evolution using simplified approaches. These may not capture important physical phenomena of the contrail, such as the size distribution of contrail ice particles, that more detailed simulations can. In the final part of this thesis, I use an intermediate-fidelity model, the Aircraft Plume Chemistry, Emissions, and Microphysics Model (APCEMM), to quantify the global RF using statistical inference, where samples are randomly drawn from the distance flown by aircraft in 2016. The global, annual average, net contrail instantaneous RF in 2016 was found to be 96 mW/m^2, within 6% of other literature estimates. The contrail energy forcing per unit flown was highest for flights over Western Europe, which was 39% and 66% higher than that for flights over the contiguous United States and South and East Asia, respectively. I also used the particle emissions approach as an input to APCEMM and found it had a correlation coefficient of 0.53 with the initial number of crystals that form in the contrail. In comparison, it had a smaller correlation coefficient of 0.10 with the energy forcing per contrail, suggesting that reducing particle number emissions may not have a strong effect on contrail RF. Finally, the effect of the overestimate in PCC in the MERRA-2 data was studied and found to reduce the global, annual average, net RF by a factor of 2.8 from 96 mW/m^2 to 30 mW/m^2. This difference could have important implications in identifying the most important climate forcers to focus on to reduce aviation's climate impact, but further research is required to quantify it more thoroughly.

Chair, Thesis Committee and Supervisor: Steven R. H. Barrett
Title: Professor of Aeronautics and Astronautics

Member, Thesis Committee: Noelle E. Selin
Title: Associate Professor, Institute for Data, Systems, and Society

Member, Thesis Committee: Raymond L. Speth
Title: Principal Research Scientist, Aeronautics and Astronautics

Acknowledgments

The PhD journey, as it is, is long and arduous, but intellectually stimulating and complete only because of the individuals and groups that have walked by my side. It is difficult to do complete justice to everyone involved, but I will try my best below.

To begin with, I would like to thank Steven, first for giving me the opportunity to study at MIT and in his laboratory, working on a range of projects that have wide-ranging and real world impacts, and also for mentoring me to improve the quality and impact of my research, as well as improving my ability to communicate the work. I am also grateful for having a diverse mix of members in my thesis committee, Noelle and Ray, who have recognized the challenges in my research and helped me overcome a number of issues. I am still in awe that they are able to drive improvements in my work despite only seeing it once or twice a semester. Also, thank you Seb and Dr. Sabnis for being readers of my thesis despite the intensities of research and teaching requirements at MIT.

I would also like to thank both NASA and the FAA for funding me throughout various parts of my thesis. My work on supersonic aicraft with NASA culminated in an exciting report studying the environmental impacts of a future fleet of supersonic aircraft - something that looks like it could happen in the next few years! At the FAA, I've been honored to be part of the international regulation making process, contributing towards the design and implementation of a soot regulation for aircraft engines. Thank you, in particular, to Daniel and Rick for guiding me throughout this world and for pushing my work to be accepted in these groups.

I am also grateful to everyone in the LAE for pushing me towards a high-quality and complete set of work. First, I think everyone in the lab leadership team has supported and guided me in some way throughout my time at MIT. Ray and Seb - thank you for diving into the murky world of contrails and putting up with me in a cramped office every week for the past 6 years. Without a shadow of doubt, your detailed insights have infinitely improved my work and allowed me to make a stamp on my field. Dr. Sabnis - thank you for all the last minute discussions on gas turbines

and for the incredible career stories that made our meetings exciting and always left me thinking deeper about these topics. Lastly, Florian - thank you for being the rogue economist and explaining weird things like discount rates and net present value, as well as being available to listen after a tough meeting.

The lab wouldn't be complete without its students, both current and alum. Through both technical discussions contributing towards my thesis and random urges to understand unrelated topics, to lunch time discussions on random political issues, it has been an honor to participate in the academic program. I would like to thank all the students who have been at MIT with me, but a few specific mentions are also needed. First, alums: To Akshay, thank you for always being ready for dinner at GEOS-Chem (by the way, your English accent needs work, my friend); To Irene, thank you for guiding me on dealing with academic problems, human or otherwise; To Chris, for being my complaint buddy and for letting me fly his plane; To Liam, for being so cheerful but having average banter. Second, current students: To Prashanth, thank you for always being positive; To Carla, thank you for being so insightful; To Ines, thank you for dealing with my Spanish; To Vincent, thank you for not comparing my work to your observations before I finish; To Thibaud; thank you for being so patient and helpful with APCEMM and AEIC.

Cricket has also been a huge part of my life since I was a child. Anyone that knows me knows my obsession with this sport. During my time at MIT, I've been fortunate to be part of two cricket teams. First, the MIT cricket team - thank you for dragging me back into cricket and creating a community that first made me feel at home in the USA. From training on Barry's, to grabbing kit bags from deep within the Z-center, to meetings with Jamie, it's not just the competitive games and tours to Texas, Florida, and New York that have made MIT Cricket a limitless set of memories. It's so difficult to name all the people that have joined me throughout, but thank you to Jango, Anirudh, Keshav, Taranjit, Vaik, Bharath, Kishore, Manraj, Moiz, Murthy, Pradeep, Samarth, Sumit, Usman, Vishrant, and the ever elusive Ravi. Second, the Cavaliers cricket team - thank you for giving me a community outside of the MIT bubble and allowing me to play with a set of talented cricketers and

great individuals. The Cavaliers have reminded me of what I'm missing back home - the banter, the competition, and the camaraderie. Thank you to Jazzy and Neha, Jacques (a.k.a Uuuge), the Newmans (particularly Ella), Raghu, Vidit, AK, Muks, the Green monster, the Hulk, Dhruv, and Veda.

I would also like to thank a huge number of friends from back and that I've made through weird and wonderful ways. First, thank you to my friends from Cambridge for always planning to, but never actually, playing board games over Zoom - Imrat, Sai, GK, and Danidu. A humongous thank you to Dan for reading my thesis and always being there for me. Cheers to governors Kishan and Sathvika for exposing me to parts of Boston that I probably never would have seen and also loving Disney movies, and Bollywood movies. Finally, a huge thank you to our friends at HBS for accepting me as a partner to their community. Thank you Prerna, Anoothi, Harsha, Suraj, VJ, Ayushi, Poorvi, Apurv, Ayush, Shriti for being my extended family. Also, thank you to the HBS cricket team, particularly, Shouvik, Shrey, Burjis, Vipul, Shreyas, and Rohan for the hyper-competitive games. Finally, thank you to Chandani and Pragya for always being the closest of friends.

Finally, I would like to thank my family. Thank you to my parents and sister for instilling in me a set of values I will always carry with me. There have also been a number of major life events during my PhD. Through this time, I have welcomed a brother-in-law, a second set of parents, a younger sister, and a mischeavous and adorable nephew, who definitely loves me more thank anyone else! I'd also can't thank my wife enough, for supporting me throughout, but particularly for pushing me through the last 2 years of my PhD and trying to work through some of the challenges I faced.

Contents

List of Figures

List of Tables

Chapter 1

Introduction

1.1 Contrail climate impacts

Global climate change is a major environmental concern [1]. Aircraft operations are estimated to contribute 4% of the global climate impact using the radiative forcing metric [2]. As air transportation becomes more affordable and populations more wealthy, aviation is one of the fastest growing industries at approximately 5% growth in operations per year [3, 4]. The two major sources of aviation's climate impact are CO_2 emissions and contrails (including contrail-cirrus) contributing approximately 34% and 57% of the overall impact, respectively [5].

Condensation trails, or contrails, are line-shaped ice clouds that form in the exhaust plume of aircraft engines under sufficiently cold and humid conditions. The formation process follows the Schmidt-Appleman criterion (SAC), which requires that the mixing between the exhaust plume and ambient air lead to water supersaturated conditions, before the ice crystals freeze in ice supersaturated conditions [6–8]. If linear contrails persist for several hours, they can grow into large, diffuse contrail-cirrus clouds that are "indistinguishable from natural cirrus clouds" [9–13]. Contrails lead to a climate impact by interacting with incoming solar radiation (ISR) and outgoing thermal radiation (OTR) [14], by changing the difference between the radiation absorbed versus radiated out by the Earth, referred to as the radiative forcing (RF). Contrail ice crystals scatter some portion of the ISR back into space leading to a cool-

ing effect. The ice crystals also absorb OTR emitted from the surface of the Earth and re-emit this at a lower temperature leading to a warming effect. The two effects sum together to lead to a net warming effect across all contrails. Global simulations of contrails have estimated the annual average net radiative forcing to be 50 mW/m^2 in 2011. However, these estimates vary by almost an order of magnitude [15].

This uncertainty is due to a number of factors from the engine emissions and operation [16] to the expected ice crystal habit [17, 18]. In this thesis, I address three sources of uncertainty: the number of black carbon (BC) particles emitted by the engine, the accuracy of the meteorological datasets used for modeling contrails, and the approach to simulate the microphysical evolution of a contrail.

The number of BC particles emitted by aircraft engines is not well understood due to the challenge of sampling particles from an aircraft exhaust and subsequently counting the particles (see e.g.; [19, 20]). The number emitted by an engine must be estimated for contrail modeling as they form the nuclei upon which ice can freeze as the contrail forms [12]. They thus have an effect on the lifetime and optical properties of a contrail. For example, Burkhardt, Bock, and Bier [21] found that reducing the initial number of ice crystals by 80% could reduce the global climate impact of contrails by 50%, however the size and direction of this effect is sensitive to the assumed ice crystal habit [17]. To understand why this happens, consider a contrail in fixed background conditions. Decreasing the number of BC particles emitted leads to fewer, larger ice crystals, and this has two effects. First, each individual crystal will be heavier and have a higher settling velocity. These crystals reach lower, warmer altitudes where they can evaporate faster, reducing the overall lifetime of the contrail and decreasing the integrated radiative forcing over its life. Second, the larger crystal size and lower number concentration reduces the total cross-sectional area of the crystals per unit contrail mass, which reduces the contrail's optical depth [22], though the effect on the global, annual average radiative forcing is less well understood [17]. An accurate representation of BC particle number emissions is therefore necessary to model individual contrails. However, most global contrail simulations have assumed a fixed number of BC particles emitted per mass of fuel [15, 23–26].

Next, I quantify the dependence of contrail formation on the background atmospheric conditions, specifically the temperature and humidity. Global contrail models use meteorological reanalysis from data assimilation systems such as the NASA Modern Era Retrospective analysis for Research and Applications V2 (MERRA-2) [27]. These models assimilate observations with numerical estimates of the atmosphere. Recent studies have shown that reanalyses tend to overestimate upper tropospheric water vapor concentrations, in some cases by up to 150% [28, 29]. Overestimates have also been observed when comparing the probability of a persistent contrail forming from meteorological data against satellite measurements [30, 31]. These studies, however, do not provide a comprehensive and quantitative comparison between simulation data and measurements.

Global contrail simulations model the evolution of contrails using simplified approaches [17, 23, 25, 26]. One approach is to track contrail cross-sections and assume they evolve as a Gaussian plume in homogeneous, idealized conditions, and that all ice particles are the same size at any given time (monodisperse). The size of contrail ice particles can vary by up to an order of magnitude, with the largest particles carrying a large fraction of the ice mass to lower, warmer altitudes where they melt [32, 33]. This leaves behind a smaller number of particles representing a smaller amount of ice, which settle more slowly and last longer. A Gaussian plume cannot reproduce this behavior and the contrail is assumed to evolve with uniform properties and all particles settling identically. Given the sensitivity of contrail impacts to the particle size and internal structure of the contrail, this opens questions regarding the Gaussian model's ability to reproduce variability in contrail behavior and radiative forcing. On the other hand, large-eddy simulations (LES) are able to capture the physics of contrail evolution, but are computationally intensive to be used for global simulations. It is therefore necessary to develop a new approach to simulate contrails that can accurately model their evolution, but is efficient enough to be applied globally.

1.2 Thesis components

In this thesis, I address the three sources of uncertainty issues discussed previously: BC particle emissions, background atmospheric conditions, and the modeling approach. The main contributions of this thesis are:

1. **Quantifying BC particle emissions from aviation engines using existing measurements.** In Chapter 2, I develop an approach to estimate the emissions of BC particles from the exhaust of aircraft engines. This is achieved using a set of complementary datasets that (1) allow the conversion of smoke number, a filter-based approach to measuring the opacity of the exhaust plume, to BC mass concentration; (2) relate mass emissions to particle number emissions; and (3) correct for the loss of particles in the measurement process and estimate the size of particles. Using the estimated mass concentration and particle size, I estimate the number of BC particles emitted by the engine. This work was published in *Environmental Science and Technology* in 2019 [34].

2. **Quantifying the error in using reanalysis data for modeling persistent contrail formation.** Given the overestimate of upper tropospheric water vapor found in multiple reanalyses [28, 29], I quantify this error in using two reanalysis datasets, the NASA Modern Era Retrospective analysis for Research and Applications V2 (MERRA-2) [27] and the European Center for Medium-Range Weather Forecasts (ECMWF) ERA5 [35], in the prediction of the formation of persistent contrails. This work shows that errors in simulated humidity are the main cause of this overestimate and could lead global estimates of contrail coverage to be overestimated by 100% - 250%.

3. **Inferring global contrail radiative forcing using an intermediate fidelity model.** Finally, I develop a new approach to model contrails on a global scale using a statistical inference approach. This approach randomly samples from the distance flown by aircraft in 2016 and models the potential contrail formation and evolution using the Aircraft Plume Chemistry, Emis-

sions, and Microphysics Model (APCEMM) [36]. APCEMM is a 2-dimensional model capable of simulatng the formation of contrail ice crystals on the surface of sulfate-coated BC particles, as well as the subsequent diffusion, settling, and growth (evaporation) of ice crystals in supersaturated (subsaturated) conditions. APCEMM is specifically able to capture the internal structure of the contrail and resolve the size distribution of ice crystals over the contrail lifetime, neither of which have previously been captured in global scale contrail modeling. As an intermediate fidelity model, APCEMM can be run on several thousand contrail samples and global contrail properties can be inferred from the mean properties over all samples. Finally, the Rapid Radiative Transfer Model (RRTM) [37] is used with a two-habit particle model for ice crystals [38, 39] in order to estimate contrail RF.

Overall, this thesis improves upon current global contrail models by developing new approaches to estimate particle emissions, quantifying existing biases in meteorological reanalyses, and developing a new method to estimate global contrail properties using intermediate fidelity models. Having a deeper understanding of the uncertainties and improving upon current modeling approaches is critical to inform mitigation efforts.

Chapter 2

Development of a method to estimate aviation BC particle emissions

2.1 Introduction

Global commercial aviation activity has been forecast to grow by 1.5-4.1% annually between 2020 and 2050 under a range of IPCC scenarios [40]. The upper end of this range is consistent with industry projections that forecast requiring almost double the fleet size by 2036 [3, 4]. Emissions from aircraft engines near airports and at cruise lead to a variety of climate impacts [5] and can increase surface-level particulate matter (PM) and ozone (O_3) concentrations, which can lead to adverse health impacts [41–45].

Aviation BC emissions have three major effects on global warming. First, BC particles absorb outgoing longwave radiation leading to a direct warming effect [5, 45]. Second, BC particles emitted at cruise altitudes serve as ice nuclei to promote the formation of contrails. Contrails are considered to be one of the largest of aviation's climate impacts [46, 47] and have been found to be sensitive to the number of BC particles. For example, Kärcher and Yu [12] found that the number of ice crystals that

form is proportional to the number of BC particles emitted by the engine at emission levels above approximately 10^{14} particles/kg, depending on the ambient conditions [12, 17]. Burkhardt, Bock, and Bier [21] found that reducing the initial number of ice crystals by 80% could reduce the global radiative forcing of contrails by 50% for hexagonal ice crystals. Caiazzo et al. [17], when assuming hexagonal ice columns, found a smaller reduction of 9% in the contrail radiative forcing over the contiguous United States for a 66% reduction in particle emissions. However, they also found that the size and direction of this effect is sensitive to the assumed ice crystal habit [17]. Finally, BC particles can also affect natural clouds as they promote heterogeneous nucleation, where droplets and ice crystals can form on them. For example, Penner et al. [48] found that aircraft BC emissions cause a 200 mW/m^2 cooling effect since the availability of BC particles can act to reduce the number of ice crystals that form compared with the homogeneous nucleation of cirrus ice crystals. Being able to quantify the number of BC particles emitted by an engine is thus crucial to assessing the climate impact of aviation.

In addition to global warming, PM emissions can lead to adverse air quality and health impacts. While current epidemiological evidence is based on mass concentrations of PM emissions, increasing toxicological evidence points to the importance of number (or surface area) as a metric of importance for adverse health impacts [49]. This is a particular concern for aircraft engines due to their emissions of "ultra-fine" PM, with aerodynamic diameter below 100 nm [19, 50–54]. Ultra-fine particles can increase the ambient particle number concentrations, where decreases in the average particle size can increase lung deposition fractions [55–58]. Median estimates for premature mortalities attributable to all aviation emissions in 2006 vary between 9,000 [59] and 16,000 [41], which represents $\leq 2\%$ of premature mortalities caused by outdoor air quality degradation due to anthropogenic emissions. BC emissions account for 0.2% of this health impact due to full flight, global emissions [60]. However, this result does not account for differences between fine and ultra-fine PM, and the BC contribution may be higher at a regional level [42].

These concerns have led the International Civil Aviation Organization's (ICAO)

Committee for Aviation Environmental Protection (CAEP) to develop emissions standards for aircraft engines, which currently include limits on NO_x, unburned hydrocarbons, and carbon monoxide emissions during a standard landing and takeoff (LTO) cycle [61]. Aircraft engine black carbon (BC) emissions have also been regulated indirectly through the Smoke Number (SN) standard adopted in 1981.

The SN standard was developed to limit the visibility of the black soot from aircraft engine exhaust plumes. It is measured by capturing the BC in the exhaust stream on a filter and measuring its change in reflectance [62]. While the SN is useful for estimating the visibility of the plume, it is not a suitable metric to quantify air quality impacts on human health or climate impacts. Advanced measurement systems have therefore been developed to measure BC emissions from aircraft engines. The systems have evolved over a series of engine measurement campaigns, including the Aircraft Particle Emissions Experiment (APEX) [63], the Aviation-Particulate Regulatory Instrumentation Demonstration Experiment (A-PRIDE) [50], and an additional study demonstrating the method for smaller engines [19]. This work has culminated in an Aerospace Recommended Practice (ARP) that provides guidelines for the measurement of BC emissions [64].

In addition to improvements in the measurement systems, reporting requirements and a mass concentration standard for engines produced after 1 January 2020 were established at the 10th meeting of CAEP. While this reporting requirement is useful for quantifying future emissions of mass and number of BC particles, there remain a range of engines that are expected to continue active operation with no BC measurements available. For this reason, various correlations have been developed that relate SN with BC mass concentration, including the FOA3 method [65] and a correlation developed by Stettler et al. [66]. These have been used as the basis of estimates for several air quality studies, however they can vary by a factor of 4 in estimating total global BC emissions [67].

In this thesis, I use a dataset of simultaneous SN and mass concentration measurements to improve the estimation of aircraft engine BC mass concentration from SN data (dataset-1). While similar in form to the original dataset used to develop

FOA3 [65], the measurements used here were taken using a standardized measurement system defined in ICAO Annex 16 Vol. II [61] and the SN and mass concentration measurements were acquired simultaneously. The FOA3 method was developed using certification SN data, with mass concentration measured independently using in-service engines. Thus, dataset-1 is expected to lead to a more reliable correlation than these previous studies. Despite the advancements in measurement systems, the long sampling lines required to transport the BC from engine exit to measurement devices lead to particle losses as, for example, particles are deposited on the walls of the sampling lines. These losses have been discussed in various measurement campaigns [51, 63] and can be in excess of 50%, increasing as the GMD of particles decreases [68]. Using a dataset of simultaneous BC mass and particle number emissions (dataset-2), I have developed a correlation to estimate mass system loss correction factors when only mass concentration data is available. Using this same dataset, I also developed a method to predict the number of BC particle emissions by assuming a lognormal size distribution and correlating the GMD with a function of measured mass concentration and the pressure at the combustor exit. These correlations and the method to convert them to total BC mass and number emissions is referred to as the Smoke COrrelation for Particle Emissions - CAEP11 (SCOPE11), and will be used by airports and ICAO-CAEP in developing international standards for the regulation of aircraft engine BC emissions. In addition, this work can be used by modelers to improve estimates for aviation BC emissions and evaluations of aviation's environmental impact.

2.2 Materials and methods

2.2.1 SN to BC mass concentration correlation

I use a dataset of 1407 paired BC mass concentration (C_{BC}) and SN measurements referred to as dataset-1. These measurements were taken in order to support the CAEP process, and comprise measurements of 24 aircraft engine models from 6 man-

ufacturers over a range of engine thrust settings. The SN and C_{BC} measurements were made using standardized measurement systems as defined in ICAO Annex 16 Vol. II [61] and the data represents measurements at the instrument ($C_{\mathrm{BC},i}$), rather than at the engine exit plane ($C_{\mathrm{BC},e}$), but does include corrections for thermophoretic losses [61, 62]. The measurement system involves three sections: collection, transfer and measurement. The collection of BC particles occurs through a single- or multi-point rake with sampling probes, after which the sample flows through a heated sample line. The sample is then transferred to a diluter to reduce further coagulation and thermophoretic losses, before being passed through a 1 µm cyclone separator in order to remove large particles that are assumed not to be generated by combustion. Finally, BC mass measurements are made using either an AVL Micro Soot Sensor (MSS) or Laser Induced Incandescence (LII), and number measurements are made using an AVL Particle Counter (APC), which also requires a volatile particle remover (VPR) to condition the sample for non-volatile particle number measurements. Major sources of uncertainty are found in the measurement instruments, estimated to be 25% for both mass and number, as well as errors due to temperature and pressure measurements, and errors due to dilution factor measurements [50].

By using standardized, certification-compliant measurement systems, dataset-1 contains high quality measured data from a wide variety of engines, which has previously been unavailable. The measurement points are shown in figure 2-1 (blue circles). Note that while the data has a general exponential trend for SN ≥ 5 (linear in semi-logarithmic axes), the behavior below this SN is not as clear. In the SN $<$ 5 regime, there is significant spread in the data, such that at SN $= 0$, the $C_{\mathrm{BC},i}$ can vary by approximately 3 orders of magnitude. To help visualize the trends, I have separated the data into 25 distinct bins by range of SN and plotted the median mass concentration for each bin (orange, unfilled circles). The median set of data reveals an exponential trend for SN ≤ 5 that has a steeper gradient than that for higher SNs.

To account for the observed shape and the changing trend between low and high SN, I develop a correlation using the product of an exponential function (governing the behavior for high SN) and a logistic function (governing the behavior for low SN):

$$C_{\mathrm{BC},i} = \frac{k_1 e^{k_2 \mathrm{SN}}}{1 + e^{k_3(\mathrm{SN}+k_4)}} \tag{2.1}$$

where k_i are constants that are determined by a two-step nonlinear least-squares fit. In each step, the fit is carried out on the logarithm of $C_{\mathrm{BC},i}$ in order to produce a fit that is applicable across the full range of SNs. In the first step, the constants k_1 and k_2 are found by fitting the data for SN ≥ 5 to the exponential function $C_{\mathrm{BC},i} = k_1 e^{k_2 \mathrm{SN}}$. In the second step, the full data set is fit to the combined equation, holding k_1 and k_2 constant, in order to find k_3 and k_4.

To quantify the variability within the data, I also calculate prediction intervals. These are the intervals between which I have a specified probability (e.g. 90%) that a new concurrent SN and $C_{\mathrm{BC},i}$ measurement would lie. To determine these bounds, I hold k_2 and k_3 fixed. k_1 is found using an optimization routine that uses the SN $\geq$ 5 data and ensures 5% of the data above and 5% of the data below the upper and lower bounding lines, respectively. The same method is used to find k_4, but using the data for SN ≤ 5.

2.2.2 System loss corrections

As with any sampling-based particle measurement, there are particle losses in the standardized measurement system which lead to differences between the BC emissions measured at the instruments versus those actually emitted from the engine at the exit plane. Losses occur due to changes in flow direction that cause particles to embed on internal surfaces. This loss can occur due to bends in the sampling lines and the lack of penetration of particles through individual components. The losses of particles in individual components can also be a function of size. For example, losses in the VPR are determined to be around 60% for particles with 15 nm aerodynamic diameter, and 30% at a diameter of 50 nm [19], consistent with trends from measurements for automotive vehicle emissions [69]. These losses, referred to as system losses, have been found to reduce the measured mass of emissions by up to a factor of 2, while losses for number emissions can be greater than a factor of 50 [68]. Losses depends

on particle size due to device-specific penetration functions and the higher diffusion of smaller particles that can be absorbed on the line walls. These losses can be estimated by using a system loss calculator developed by SAE [68], which requires input on the exhaust gas temperature, sampling line lengths and temperatures, and measured values.

Given that dataset-1 contains measurements at the instrument, I must correct for system losses to estimate emissions at the engine exit plane. Using a set of simultaneous BC mass and particle number data measured using the standard-compliant measurement systems [70] (dataset-2) and corrected for differences in fuel hydrogen content, system loss correction factors for mass (k_{slm}) have been estimated using the SAE system loss calculator [68]. I find that the mean particle size, or the geometric mean diameter (GMD), tends to increase with increasing combustor mass concentration due to coagulation (see subsequent subsections) and thus can be used to predict k_{slm}. To allow for a closed-form equation for k_{slm}, I use the mass concentration per unit volume of core flow at the instrument, which has also been found to be a good predictor of the GMD and thus k_{slm}.

The system loss correction factors have been correlated with BC mass concentration using the functional form:

$$k_{\mathrm{slm}} = \ln\left(\frac{a_1 C_{\mathrm{BC},i}(1+\beta_{\mathrm{mix}}) + a_2}{C_{\mathrm{BC},i}(1+\beta_{\mathrm{mix}}) + a_3}\right) \tag{2.2}$$

where β_{mix} is equal to the bypass ratio for mixed-flow engines and zero otherwise. The factor $1+\beta_{\mathrm{mix}}$ corrects the exit plane mass concentration for mixed-flow engines to a core-equivalent value. The form of the equation was chosen to obtain the expected asymptotic behavior at high mass concentrations or high GMDs ($k_{\mathrm{slm}} \to \ln a_1$) and a bounded value at low concentrations or low GMDs ($k_{\mathrm{slm}} \to \ln \frac{a_2}{a_3}$).

The fit is conducted using non-linear regression, with 34 of the data points discarded as they were either below the mass measurement limit of detection ($C_{\mathrm{BC,lim}} = 1.0$ µg/m^3), were considered anomalous due to measurement errors, or system loss correction data was not available. k_{slm} can be applied as a multiplicative factor on

the emissions index for the mass of BC, $\mathrm{EI}_{m,i}$(BC), which measures the mass of BC produced per mass of fuel burnt [mg/kg-fuel]. I use the Python package Kapteyn [71], which uses a linear approximation of eq 2.2 to estimate the confidence and prediction intervals. To prevent unrealistic values, I constrain the intervals to have a value greater than or equal to 1.

2.2.3 Calculating emissions indices

Using the SCOPE11 correlation, I can estimate C_{BC} from SN data. This can be converted into an emissions index following the method described by Wayson et al. [65]. $\mathrm{EI}_{m,i}$ (BC) is calculated by multiplying $C_{\mathrm{BC},i}$ with the volumetric flow rate, Q [m^3/kg-fuel]. By assuming a fuel hydrogen content of 13.8% by mass, this is calculated as:

$$\begin{aligned} Q_{\mathrm{unmixed}} &= 0.776\mathrm{AFR} + 0.767 \\ Q_{\mathrm{mixed}} &= 0.776\mathrm{AFR}(1+\beta) + 0.767 \end{aligned} \tag{2.3}$$

where, Q_{unmixed} is the volumetric flow rate for engines with an unmixed exhaust nozzle and Q_{unmixed} is for engines with mixed nozzles that require a correction for the bypass ratio, β. The derivation of these results is provided in Appendix A. These equations require an estimate of the overall air to fuel ratio (AFR). Wayson et al. [65] provide estimates for AFR at the four ICAO LTO thrust settings of 106 at idle (7% of rated thrust), 83 at approach (30% of rated thrust), 51 at climb-out (85% of rated thrust) and 45 at take-off (100% of rated thrust), which is also presented in Table 2.1. I then apply the system loss correction factors to $\mathrm{EI}_{m,i}$(BC) to estimate the emissions at the engine exit plane.

2.2.4 Estimating the number of BC particles at the engine exit plane

The number of BC particle emissions index at the engine exit plane, $\mathrm{EI}_{N,e}$(BC), can be calculated using $\mathrm{EI}_{m,e}$(BC) and an estimate of the geometric mean diameter (GMD)

at the same plane. Assuming a log-normal size distribution, the relationship between these variables can be shown to be [72]:

$$\mathrm{EI}_{N,e}(\mathrm{BC}) = \frac{6\mathrm{EI}_{m,e}(\mathrm{BC})}{\pi\rho\mathrm{GMD}^3 e^{4.5(\ln\sigma)^2}} \tag{2.4}$$

where ρ is the effective density of soot assumed to be 1000 kg/m^3 and σ is the geometric standard deviation (GSD), which has been found to be around 1.8 from experimental observations [52, 73].

In order to apply this equation, I require an estimate for the GMD at the engine exit plane. This value is a complex function of production rates in the combustor primary zone, oxidation of BC in the secondary zone and coagulation of particles as they grow downstream of these regions. Measurement campaigns have also shown that the GMD tends to increase with thrust rating [47, 60], which is due in part to the increase in pressure (and therefore density) at higher relative thrust that drives coagulation rates. As such, I use a measure of the BC mass concentration at the combustor exit, $C_{\mathrm{BC},c}$, which is a function of both $C_{\mathrm{BC},e}$ and the conditions at the combustor exit.

The data required for this correlation is estimated from measurements in dataset-2. $C_{\mathrm{BC},e}$ is found by converting the $\mathrm{EI}_{m,e}(\mathrm{BC})$ in dataset-2 to a concentration using the volumetric flow rate calculated via eq 2.3. The exit plane concentration is converted to an estimate of $C_{\mathrm{BC},c}$ using the method outlined below. The GMD at the engine exit plane is then estimated using eq 2.4. This first requires converting instrument measured mass and particle number emission indices to exit plane values. The loss correction factor for mass emissions ranges between 1.1 and 2.4 and that for particle number between 1.3 and 20.7. Finally, I assume an effective soot density of 1000 kg/m^3 and GSD of 1.8. Using dataset-2, I have developed a correlation of the form:

$$\mathrm{GMD} = aC_{\mathrm{BC},c}^{b} \tag{2.5}$$

where a and b are constants to be determined. $C_{\mathrm{BC},e}$ is scaled to the concentration at the combustor exit using the ratio of the combustor exit to ambient density:

$$C_{\mathrm{BC},c} = C_{\mathrm{BC},e}(1 + \beta_{\mathrm{mix}})\rho_{t4}/\rho_a \tag{2.6}$$

where $C_{\mathrm{BC},c}$ is the predicted BC mass concentration at the combustor exit, $C_{\mathrm{BC},e}$ is the mass concentration at the engine exit plane, scaled to standard temperature and pressure, β_{mix} is the same parameter as used in eq 2.2, ρ_a is the density of ambient air (1.2 kg/m^3) and P_{t4} is the total density of air at the combustor exit. ρ_{t4} is dependent on the pressure at the combustor exit, increasing with the thrust level, and can be found using the ideal gas law:

$$\rho_{t4} = \frac{P_{t4}}{R_{\mathrm{air}} T_{t4}} \tag{2.7}$$

where subscript $t4$ represents the turbine inlet/combustor exit location, P is the pressure, T is the temperature and R_{air} the specific gas constant of air. The pressure and temperature at the turbine inlet can be estimated by assuming no pressure loss in the combustor and using a first order energy balance across the combustor.

$$\begin{aligned} P_{t4} &= P_{t2}(1 + (\pi_{00} - 1)\frac{F}{F_{00}}) \\ T_{T4} &= \frac{\mathrm{AFR} c_{p,a} T_{t3} + \mathrm{LCV}}{c_{p,e}(1 + \mathrm{AFR})} \end{aligned} \tag{2.8}$$

where π_{00} is the overall pressure ratio in the engine at rated thrust, $^F/_{F_{00}}$ is the fractional thrust, AFR is the air to fuel ratio, $c_{p,a} = 1.005$ kJ/kg/K is the heat capacity at constant pressure of air and $c_{p,e} = 1.250$ kJ/kg/K is that for the combustion products, LCV = 43.2 MJ/kg is the lower calorific value of the fuel and T_{t3} is the temperature at the inlet to the combustor. T_{t3} can be estimated assuming a constant polytropic efficiency, η_p, of 0.9 for the flow through the core fan and compressor:

$$T_{t3} = T_{t2}\left(\frac{P_{t3}}{P_{t2}}\right)^{\frac{(\gamma-1)}{\gamma\eta_p}} \tag{2.9}$$

where T_{t2} and P_{t2} are the total temperature and pressure at inlet to the gas turbine and γ is the heat capacity ratio of air (taken to be 1.4). Using these relationships, I can find the BC mass concentration at the combustor exit and subsequently conduct

a linear regression on the logarithm of eq 2.5. The regression was conducted using the Statsmodel package in Python [74], which also estimate the confidence and prediction intervals. When conducting the regression, I discard the same data points that were discarded in the regression conducted for system loss corrections.

2.2.5 Estimating global BC emissions

LTO BC emissions for commercial, passenger aviation activity in 2005 and 2015 can be estimated directly from the number of aircraft operations and the type of aircraft for each origin-destination pair. The Official Airline Guide (OAG) supplies schedule data with information on airport pairs that includes both sets of information for a full year. Matching the aircraft to an engine allows me to estimate SN and fuel flow rates by identifying the engine in the ICAO engine emissions database [75]. This can be used with the ICAO LTO cycle [61], reflective of aircraft operations up to 915 m above ground level, as shown in Table 2.1 and the correlations for $\mathrm{EI}_m(\mathrm{BC})$, k_{slm} and $\mathrm{EI}_N(\mathrm{BC})$ developed in this paper to calculate the exit-plane mass and number of BC particle emissions for a specified aircraft engine. Further details on the OAG data and aircraft-engine pairs can be found in Stettler et al. [76].

Table 2.1: The power setting, time in mode, and AFR from the ICAO LTO cycle [61]

	Power setting (% of max thrust)	Time in mode (min)	AFR
Taxi/Idle	7	26	106
Approach	30	4	83
Climb out	85	2.2	51
Takeoff	100	0.7	45

Although the SCOPE11 method is developed for ground operations only, emissions during cruise can be estimated using Dopelheuer and Lecht [77]. Their correlation scales a reference ground emission at a thrust setting of 100% using the air-fuel ratio (AFR), combustor inlet pressure, P, and the combustor flame temperature T_f as

$$C_{\mathrm{BC,cruise}} = C_{\mathrm{BC,ref}} \left(\frac{\mathrm{AFR}_{\mathrm{ref}}}{\mathrm{AFR}_{\mathrm{cruise}}} \right)^{2.5} \left(\frac{P_{\mathrm{cruise}}}{P_{\mathrm{ref}}} \right)^{1.35} \frac{e^{-20000/T_{f,\mathrm{cruise}}}}{e^{-20000/T_{f,\mathrm{ref}}}} \tag{2.10}$$

where C_{BC} is the Black Carbon mass concentration, subscript cruise and ref refer to the cruise and ground reference value, respectively, and T_f, in Kelvin, is calculated as

$$T_f = 0.9T_{t3} + 2120 \tag{2.11}$$

where T_{t3} is the combustor inlet temperature in Kelvin. Further details on the method to calculating the AFR, pressures, and temperatures can be found in [78].

2.2.6 Propagating uncertainties

For all the correlations that have been conducted, I include confidence and prediction intervals. Confidence intervals provide the range between which the true regression line is expected to be found with probability $(1 - \alpha_c)$. This can inform on the uncertainty in estimating the mean results. Prediction intervals provides the range between which an individual observation may lie with probability $(1 - \alpha_p)$. This interval includes the uncertainty in the mean result, as in confidence intervals, as well as the scatter in the underlying data, leading to a wider interval. These two intervals encompass the uncertainties inherent in all of the methods. For example, in the SN to $C_{\mathrm{BC},i}$ correlation, the uncertainty increases as the SN decreases. For k_{slm}, differences between measurement systems and their setup and calibration can lead to variations in the mass system loss correction. Finally, the GMD to $C_{\mathrm{BC},c}$ correlation relies on assumptions on the effective soot density and GSD. Given sufficient data, all of these uncertainties as well as the underlying measurement uncertainties will be reflected in the variation of the measurements around the best fit line. In turn, this variability is accounted for in the confidence and prediction intervals.

The confidence intervals can be used to estimate the uncertainty in the global BC estimates for both LTO and cruise operations. I apply the lower and upper confidence intervals for each correlation to get a lower and upper estimate of the uncertainty in these estimates. The prediction intervals can be used to estimate the uncertainty in individual predictions of $\mathrm{EI}_{m,i}(\mathrm{BC})$, $\mathrm{EI}_{m,e}(\mathrm{BC})$ and $\mathrm{EI}_{N,e}(\mathrm{BC})$.

2.3 Results

2.3.1 SN to $C_{BC,i}$ correlation

The two step, nonlinear least squares fit leads to the following best fit relationship:

$$C_{BC,i}\left[\frac{\mu g}{m^3}\right] = \frac{648.4e^{0.0766SN}}{1+e^{-1.098(SN-3.064)}} \tag{2.12}$$

This is shown by the black, solid line in figure 2-1. The 95% confidence intervals in the parameters are:

$$\begin{aligned} k_1 &= 648.4 \pm 44.9\ \mu g/m^3 \\ k_2 &= 0.0766 \pm 0.0038 \\ k_3 &= -1.098 \pm 0.120 \\ k_4 &= -3.064 \pm 0.277 \end{aligned} \tag{2.13}$$

The prediction intervals within which future measurements would lie with 90% probability is also found using a similar two-step method. The resulting intervals are:

$$\begin{aligned} \text{Lower: } C_{BC,i}\left[\frac{\mu g}{m^3}\right] &= \frac{378.5e^{0.0766SN}}{1+e^{-1.098(SN-5.066)}} \\ \text{Upper: } C_{BC,i}\left[\frac{\mu g}{m^3}\right] &= \frac{1146.2e^{0.0766SN}}{1+e^{-1.098(SN-1.480)}} \end{aligned} \tag{2.14}$$

These equations, along with the best fit line, are shown in figure 2-1. The gradients of the high SN and low SN limits are equal for the lower, upper and best fit lines. However, the transition point between these regions moves from 1.480 for the upper line to 5.066 for the lower line.

Figure 2-2 provides a comparison of the SCOPE11 correlation to the FOA3 [65] and Stettler et al. [66] correlations. The FOA3 relationship [65] was developed using a dataset similar to dataset-1, where the measurements were not taken using a standardized measurement system, which consisted of fewer than 75 points (compared to 1406 data pairs used here), and used SN and mass concentration measurements which were not taken concurrently. Due to these differences, the FOA3 relationship

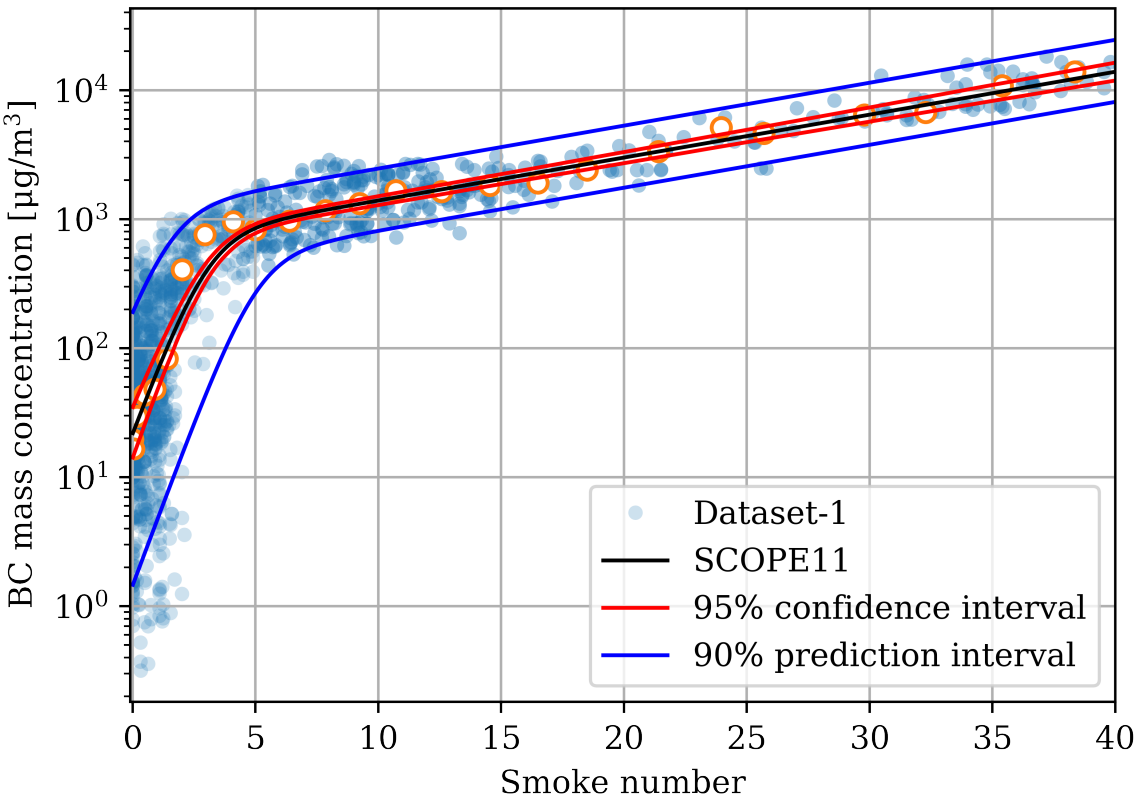

Figure 2-1: SCOPE11 best fit line (black) with 95% confidence intervals (red) and 90% prediction intervals (blue). The unfilled orange circles represent the median values of binned dataset-1 values.

tends to predict lower $C_{\mathrm{BC},i}$ than the SCOPE11 correlation, except at a SN $\approx$ 2 and between 15 and 20. In addition, the FOA3 model assumes that that $C_{\mathrm{BC},i} = 0$ when SN =0, whereas the data shows a median of $C_{\mathrm{BC},i}$ = 19.6 µg/m^3 and a variation spanning 3 orders of magnitude at SN = 0.

Stettler et al. [66] used an inverse diffusion flame to generate BC, following a standardized procedure for measuring SN. However, their methods to measure BC mass differ from the certification-compliant system. They developed SN – BC mass concentration relationships for GMDs between 20 and 30 nm and for GMDs of around 60 nm, advising use of the former correlation for aircraft engines. This correlation tends to predict higher mass concentrations for a wide range of SN than the SCOPE11 correlation, lying outside of the range of the data found in dataset-1 for SNs between 10 and 25. Stettler et al. [66] also use a functional form which assumes that $C_{\mathrm{BC},i} = 0$ when SN = 0.

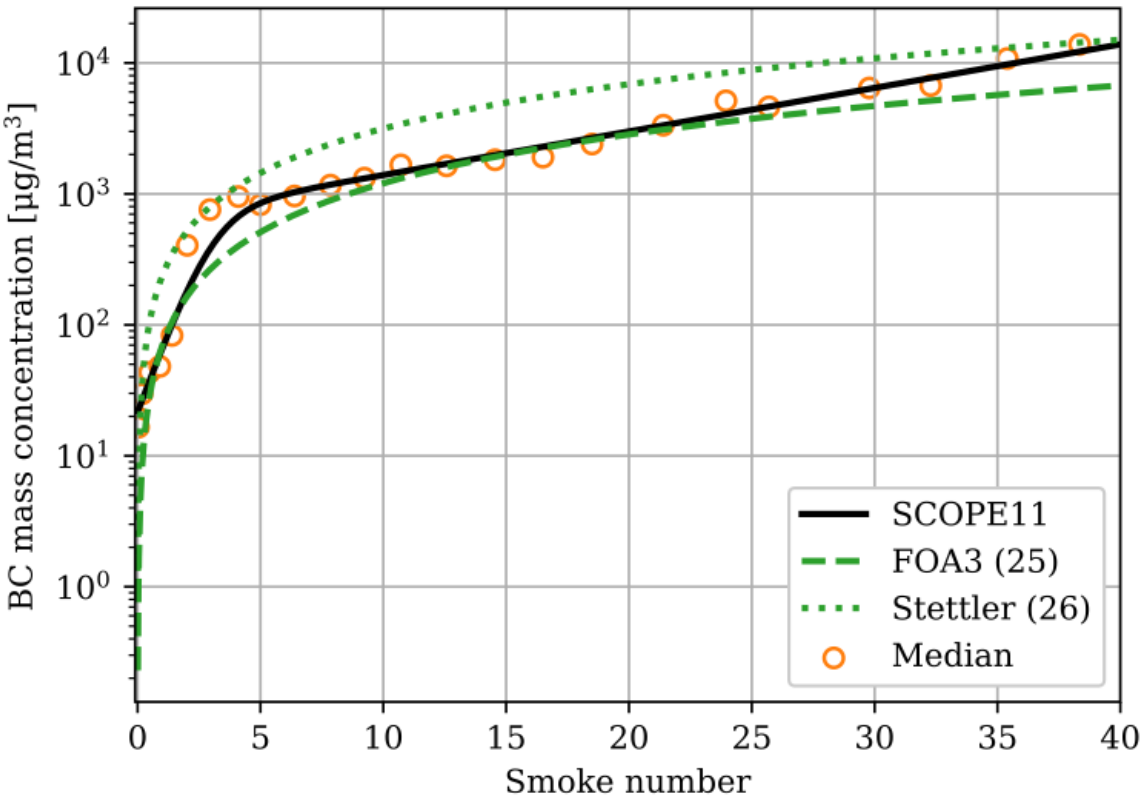

Figure 2-2: Comparison between SCOPE11 (black), FOA3 [65] (dashed, green line) and the Stettler et al. [66] correlations (dotted, green line).

2.3.2 System loss corrections

The median relationship to estimate k_{slm} from $C_{\text{BC},i}$ is shown in eq 2.15. The 95% confidence intervals for each of the constants is also shown in the set of eq 2.16.

$$k_{\text{slm}} = \ln \frac{3.219 C_{\text{BC},i}(1+\beta_{mix}) + 312.5}{C_{\text{BC},i}(1+\beta_{\text{mix}}) + 42.6} \tag{2.15}$$

$$\begin{aligned} a_1 &= 3.219 \pm 0.135 \\ a_2 &= 312.5 \pm 119.1 \ \mu\text{g/m}^3 \\ a_3 &= 42.6 \pm 19.4 \ \mu\text{g/m}^3 \end{aligned} \tag{2.16}$$

The results of this fit and the associated data is shown in figure 2-3. This functional form predicts that as $C_{\text{BC},i}$ continues to increase, k_{slm} tends towards a constant value of 1.169 ± 0.041. This is analogous to the tendency of k_{slm} to approach a constant

value as the GMD increases [68]. In addition, for $C_{\mathrm{BC},i}$ tending towards 0, I find $k_{\mathrm{slm}} = 1.99$, which is a typical value for GMD $\approx$ 10 nm, the minimum size which the measurement system can reliably capture. The spread in the measurement points are caused by two effects. First, there are differences between the systems used by each manufacturer, permitted within the measurement guidelines. These differences can include, for example, specifications of components such as the VPR, or differences in instrument calibration. Second, variations in the engine exhaust temperature can change the degree of thermophoretic losses that occur along sampling lines, which is estimated via an analytical form, also affecting k_{slm}.

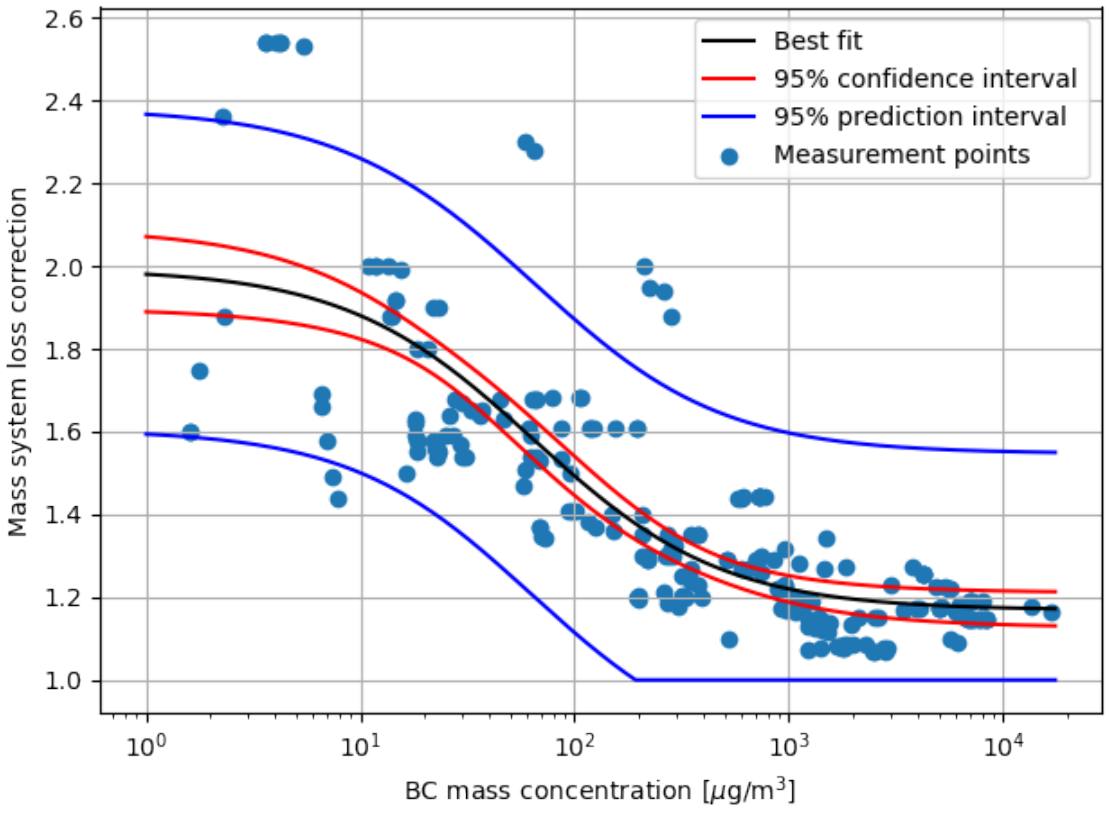

Figure 2-3: Measured BC mass concentration versus k_{slm} estimated using the line loss calculator.

2.3.3 Exit plane GMD

The results of the linear least squares regression on the power law relationship between $C_{\mathrm{BC},c}$ (in µg/m^3) and GMD is shown in eq 2.17 with associated 95% confidence intervals for each constant in eq 2.18.

$$\mathrm{GMD\ [nm]} = 5.08 C_{\mathrm{BC},c}^{0.185} \tag{2.17}$$

$$\begin{aligned} a &= 5.08 \pm 0.55 \text{ nm} \\ b &= 0.185 \pm 0.015 \end{aligned} \tag{2.18}$$

The results of this fit and the associated data are shown in figure 2-4. The adjusted R-squared was found to be 0.72 and p-values < 0.001. This relationship can thus be used to estimate the $EI_{N,e}$(BC) using eq 2.4.

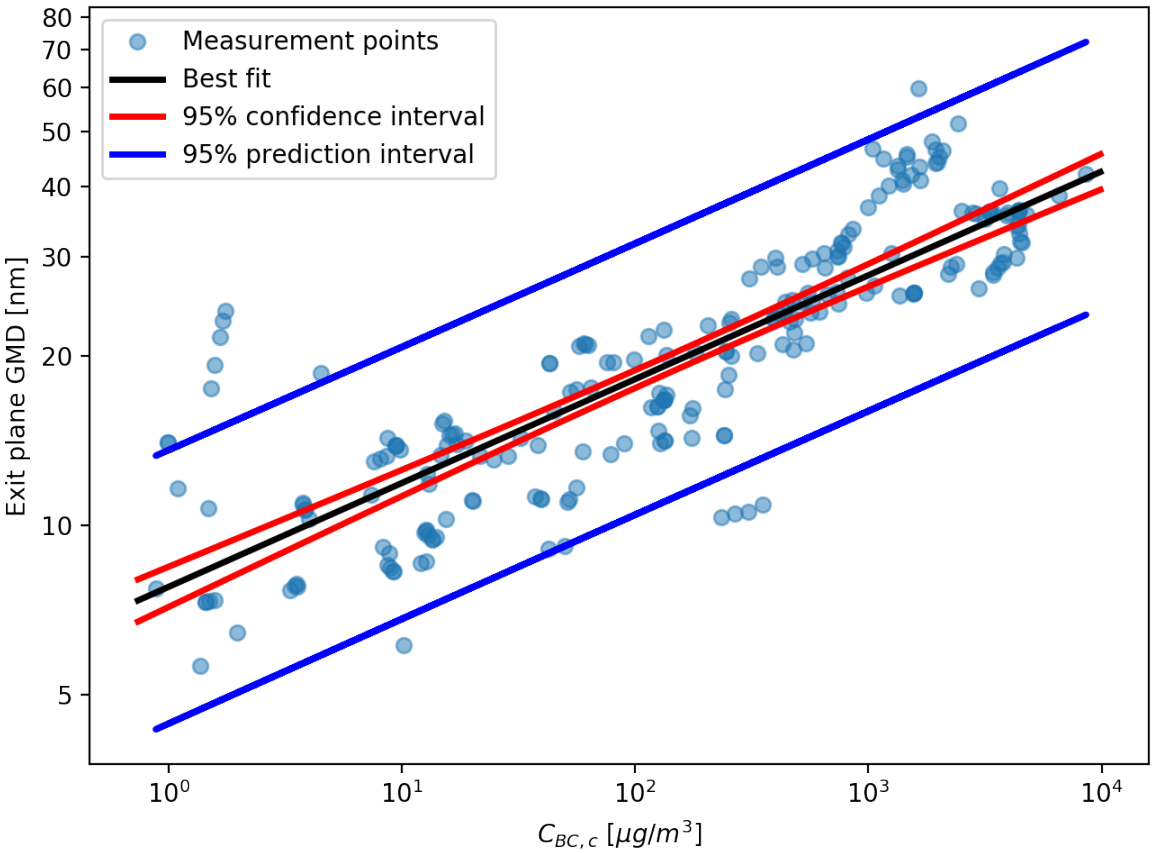

Figure 2-4: Combustor exit BC mass concentration vs GMD in logarithmic axes.

The correlation to predict GMD is dependent on the choice of the effective soot density and GSD. These are both uncertain parameters and I only use estimates of their mean value to produce this correlation. While the choice of these variables is important in estimating the GMD, they are not critical to estimating $EI_{N,e}(BC)$, since the regression constants will vary according to the assumed density and GSD, leading to a similar estimate in the $EI_{N,e}(BC)$ but with a different estimate for the GMD.

2.3.4 Comparison of measured and predicted EI

Using the results presented in the earlier sections, I can estimate $EI_{m,i}(BC)$, $EI_{m,e}(BC)$ and $EI_{N,e}(BC)$ for engines found in dataset-2, beginning with the SN at each mode of operation. Figure 2-5 shows the comparisons for $EI_m(BC)$ both with (B) and without system loss corrections (A). $EI_{N,e}(BC)$ is shown with system loss corrections only (C). The R^2 and root mean square error (RMSE) for each mode of operation as well as overall are shown in Table 2.2. These values show that the overall R^2 is around 0.8 for all cases, however the values for taxi operations for $EI_{m,i}(BC)$ and $EI_{m,e}(BC)$ tend to be lower than the other modes. RMSE values vary between 62.9 mg/kg-fuel and 74.7 mg/kg-fuel for $EI_{m,i}(BC)$ and between 76.4 mg/kg-fuel and 87.6 mg/kg-fuel for $EI_{m,e}(BC)$. Table 2.2 also includes the R^2 and RMSE values when using the FOA3 [65] or the Stettler et al. [66] correlation in place of SCOPE11, to estimate $EI_{m,i}(BC)$. While the R^2 values are all similar, this method tends to produce a higher R^2 than both, except at taxi thrust. The RMSE is lower using the SCOPE11 than the FOA3 method for all modes except taxi by 10-15%. The RMSE using the Stettler et al. [66] correlation are 168% larger than using the SCOPE11 method overall, increasing as a function of mode.

Figure 2-5(D) shows the uncertainty in the particle number emissions index for the highest thrust variant for each engine studied. Here the uncertainty distribution represents the 95% interval by propagating prediction intervals from each correlation. Each correlation is assumed to follow a normal distribution around the best fit and I propagate this distribution to the EI using a monte carlo sampling approach. The uncertainty is represented by the 95^{th} percentiles over all samples for each EI. I found

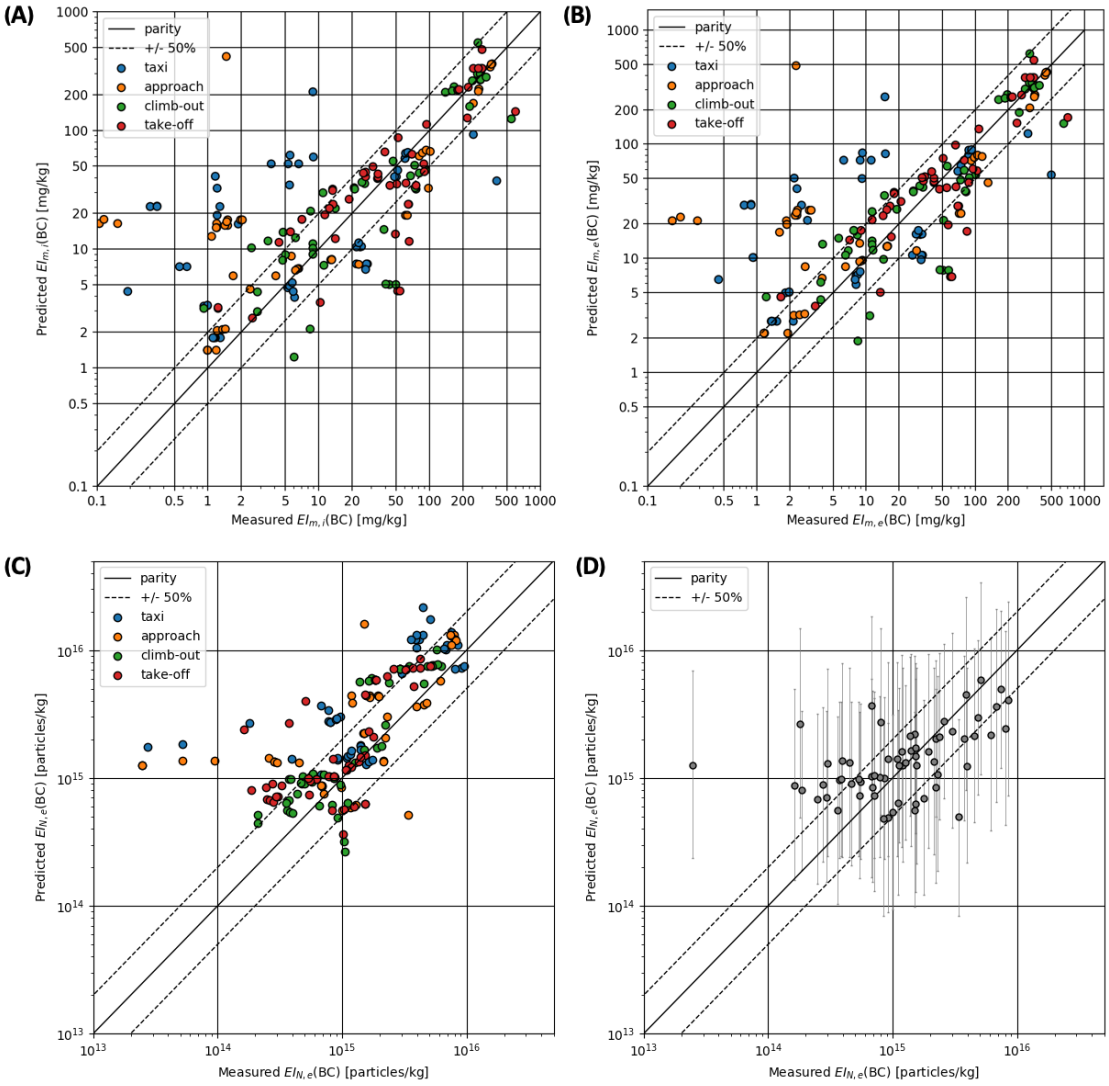

Figure 2-5: Parity plots of predicted versus measured results for (A) $\mathrm{EI}_{m,i}$(BC), (B) $\mathrm{EI}_{m,e}$(BC) and (C) $\mathrm{EI}_{N,e}$(BC), where each color represents the four ICAO LTO mode settings where measurements were taken (Table 2.1). The R^2 in each case are 0.79, 0.80 and 0.82, respectively. Figure (D) is a parity plot of predicted versus measured $\mathrm{EI}_{N,e}$(BC) for the highest thrust variant of each engine studied and the error bars represent the 95% prediction interval.

Table 2.2: R^2 and RMSE values for instrument mass emissions index ($EI_{m,i}$(BC)), exit-plane mass emissions index ($EI_{m,e}$(BC)), and exit-plane number emissions index ($EI_{N,e}$(BC)), separated by mode of operation and overall. For the exit-plane mass emissions, the SCOPE11 method is compared to the FOA3 [65] and Stettler et al. [66] methods.

		$EI_{m,i}$(BC)			$EI_{m,e}$(BC)	$EI_{N,e}$(BC)
		SCOPE11	FOA3 [65]	Stettler et al [66]	SCOPE11	SCOPE11
Taxi	R^2	0.26	0.35	0.36	0.31	0.77
	RMSE	65 mg/kg	61 mg/kg	102 mg/kg	78 mg/kg	3.1×10^15 particles/kg
Approach	R^2	0.83	0.76	0.78	0.83	0.84
	RMSE	63 mg/kg	73 mg/kg	149 mg/kg	86 mg/kg	2.6×10^15 particles/kg
Climb out	R^2	0.83	0.79	0.81	0.84	0.89
	RMSE	74 mg/kg	84 mg/kg	224 mg/kg	86 mg/kg	1.8×10^15 particles/kg
Take-off	R^2	0.75	0.73	0.75	0.80	0.85
	RMSE	75 mg/kg	82 mg/kg	249 mg/kg	86 mg/kg	8.2×10^14 particles/kg
Overall	R^2	0.79	0.75	0.76	0.80	0.82
	RMSE	69 mg/kg	75 mg/kg	186 mg/kg	82 mg/kg	1.6×10^15 particles/kg

that 2000 samples was sufficient for convergence, but used 10,000 samples for the results in figure 2-5. All uncertainty ranges span at least one order of magnitude and this uncertainty tends to reduce as the emissions index increases. This trend is caused by the uncertainty in the SN to $C_{BC,i}$ correlation, where the uncertainty range grew at the transition point below a SN of around 3.

2.3.5 Global BC emissions

Estimates of annual emissions of BC due to LTO activity for 2005 and 2015 are presented in Table 2.3. Using the SCOPE11 correlation, I estimate LTO BC mass emissions to be 0.85 Gg/yr (95% confidence interval (CI): 0.72 — 0.95) in 2005 and 0.76 Gg/yr (95% CI: 0.66 — 0.87) in 2015. I also find LTO BC particle number emissions to be 3.23×10^{25} particles/yr (95% CI: 2.15 — 5.02 $\times10^{25}$) and 2.89×10^{25} particles/yr (95% CI: 1.89 — 4.55 $\times10^{25}$) in 2005 and 2015, respectively.

The difference in annual LTO BC mass emissions between methods shows a similar trend to that found in figure 2-1 for the correlation between SN and C_{BC}. The

Table 2.3: Comparison of global LTO BC estimates. For SCOPE11-estimated BC mass and number emissions, I include estimates of the 95% confidence intervals in parentheses.

Method	LTO BC Mass [Gg/yr]		Fleet average LTO EI_m(BC) [mg/kg]	
	2005	2015	2005	2015
SCOPE11	0.85 (0.72 - 0.95)	0.76 (0.66 - 0.87)	55 (47 - 63)	40 (35 - 46)
FOA3 [65]	0.55	0.51	37	28
Stettler et al [66]	1.48	2.63	98	75
	LTO BC Number [$\times 10^{25}$ particles/yr]		Fleet average LTO $EI_{N,e}$(BC) [$\times 10^{14}$ particles/kg-fuel]	
SCOPE11	3.23 (2.15 - 5.02)	2.89 (1.89 - 4.55)	21 (14 - 33)	15 (10 - 24)

SCOPE11 method predicts around 31% higher BC mass emissions than FOA3 and around 86% lower than the Stettler et al. [66] correlation for 2015, and the trend is similar for 2005. I also find that the fleet-average EI_m(BC) using the SCOPE11 method is found to lie between the estimates using the other two methods, with similar relative differences for each year.

I also note that SCOPE11-estimated mass emissions decreased by 11% between 2005 and 2015. The FOA3 [65] and Stettler et al. [66] correlations also predict a decrease in mass emissions of 7% each. However, the total LTO fuel burn in 2015 was 22% higher than in 2005. This corresponds to a decrease in the fleet average LTO EI_m(BC) [67] correlation between 23 — 27% from 2005 to 2015. I also notice a similar trend in number emissions, which decrease by 12% from 2005 to 2015, also reflecting a decrease in fleet average EI_N(BC) of 29%.

The Aviation Emissions Inventory Code (AEIC) [78] estimates landing and take-off (LTO) emissions by mode of operation, which include taxi, approach, climb-out and take-off. This allows me to estimate BC mass and number emissions by mode of operation and I can use the upper and lower bound estimates to understand how the uncertainty changes by mode of operation.

Table 2.4 shows BC mass and number emissions for each LTO mode of operation and for all operations for the SCOPE11, FOA3 [65] and Stettler [66] correlations in 2015. As with the total LTO emissions, the SCOPE11 method predicts mass emissions between the FOA3 and Stettler correlations for both LTO and cruise operations.

I also include the uncertainty in the SCOPE11 results for both mass and number emissions. The relative uncertainty (difference between the 95th and 5th percentiles over the mean) increases from between 22% - 27% for approach, climb-out and take-off operations to 45% for taxi operations. This is because taxi operations typically have lower measured SN and this leads to the higher uncertainty from the SN – C_{BC} correlation. The total LTO emissions are driven by the climb-out and take-off modes and thus the relative uncertainty is 28%, following the relative uncertainty in these two modes. Around 62% of all BC mass emissions occur during cruise emissions and this is comparable to results using the FOA3 and Stettler et al. [66] approaches (61% and 58%, respectively). For particle number emissions, the trend is similar with taxi operations having a relative uncertainty of 108%, approach of 94%, climb-out of 67% and take-off of 64%. In this case, however, cruise emissions contribute 88% of particles emitted for all operations, 16 percentage points higher than that for BC mass emissions. The cruise, fleet-average BC mass emissions index is 18.9 mg/kg, a factor of 2.1 lower than that for LTO emissions, and the fleet-average BC particle number emissions index is 11.4×10^{14}, only 26% lower than that for LTO emissions. The difference between the reduction in mass EI versus particle number EI occurs because the particle GMD is found to reduce at cruise conditions (commensurate with the reduction in BC mass emissions index) leading the particle number EI to reduce less than the mass EI.

Table 2.4: Global LTO BC mass and number emissions by mode of operation in 2015.

	BC Mass [Gg/yr]				
	Taxi	Approach	Climb out	Takeoff	All (cruise + LTO)
SCOPE11	0.11	0.08	0.41	0.15	2.0
(5th - 95th percentile)	(0.08 - 0.13)	(0.07 - 0.09)	(0.37 – 0.46)	(0.13 – 0.17)	(1.7 – 2.3)
FOA3 [65]	0.06	0.04	0.30	0.11	1.3
Stettler et al [66]	0.20	0.13	1.65	0.28	6.9
	BC Number [$\times 10^{25}$ particles/yr]				
	Taxi	Approach	Climb out	Takeoff	All (cruise + LTO)
SCOPE11	1.30	0.54	0.72	0.25	24.2
(5th - 95th percentile)	(0.79 – 2.20)	(0.35 – 0.86)	(0.53 – 1.01)	(0.18 – 0.34)	(15.8 - 38.1)

2.4 Discussion

The SCOPE11 SN - C_{BC} correlation reduces the error in estimating BC emissions from aircraft engines in comparison to both the FOA3 [65] and Stettler [66] correlations. This improvement stems from the use of (i) a new database of simultaneously-acquired SN and BC mass concentration measurements taken using certification-compliant measurement systems from a representative sample of modern aircraft engines; (ii) a new functional form that better follows the trends between the SN and BC mass concentration relationship at SN ≤ 5; and (iii) a more complete approach to characterize the prediction uncertainty. In addition, I have extended the method to predict emissions at the engine exit plane, which accounts for measurement system losses. If system losses are not accounted for, LTO BC emissions may be systematically underestimated by around 20%. Given the direct climate and air quality impacts of aviation BC emissions, it is important to account for measurement system losses when developing emissions inventories. I have also developed a method for estimating BC number emissions at the engine exit plane, by assuming a lognormal size distribution and estimating the GMD from a measure of the BC mass concentration at the combustor exit, and applied this to the development of an inventory of LTO number emissions. Cruise emissions were also estimated using the Dopelheuer and Lecht correlation. To the best of our knowledge, this is the first estimate of BC number emissions from global commercial aircraft operations.

In order to quantify and propagate uncertainty, confidence and prediction intervals have been determined for each correlation and are shown in the figures. By propagating confidence intervals through the calculation, lower and upper bounds on the mean global LTO BC emissions are determined. These intervals depend not only on the form of the fitting equation, but also on the spread in the underlying data. This spread depends on variables for which information is available and includes uncertainty in inputs and constant parameters such as the SN, effective soot density and GSD that are required to apply the SCOPE11 method. The latter two variables are of particular importance in the number estimation. While variations in the assumed

mean values affects the prediction of the GMD, this has only a second-order effect on the $EI_{N,e}(BC)$ as the regression constants would also change if different values of the effective soot density and GSD were used. The uncertainty ranges calculated highlight the limited degree of correlation between SN and BC concentration at lower emission levels, demonstrating the benefit of developing future emissions standards on mass concentration and particle number bases and that direct measurements should be used for assessment purposes where they are available.

While this work uses the Dopelheuer and Lecht correlation to estimate cruise BC emissions [77], additional approaches that use the results of recent cruise flight measurement campaigns [79] should be developed. Given the infrequent opportunities to collect BC emissions data at cruise altitude, the development of comprehensive, full-flight inventories of BC mass and number emissions must be based on ground-level emissions estimates, such as those provided by the SCOPE11 method. Such inventories are important components which enable the assessment of aviation's environmental impacts. The ability to predict the size distribution of emissions at the engine exit plane, as in the method developed here, is particularly important for understanding the evolution and radiative impact of contrails, and in modeling the indirect effects of BC particles on natural clouds [24], both of which are among the most uncertain of aviation's climate impacts.

Chapter 3

Quantifying the error in using reanalysis data for modeling persistent contrail formation

3.1 Introduction

Condensation trails, or contrails, are line-shaped ice clouds that form in aircraft exhaust under sufficiently cold and humid conditions. They are estimated to cause an effective radiative forcing (ERF) of 17 – 98 mW/m^2 for 2011, around half of the total aviation-attributable ERF [5]. The uncertainty is based on the dependence of contrail ERF on black carbon emissions [34, 80, 81], how contrails are simulated [17, 18, 23, 82–84], and the background atmospheric conditions [16, 85].

To date, global contrail ERF estimates have relied on models using global atmospheric simulations to estimate upper tropospheric conditions. Two key variables required to simulate contrails are the local temperature and humidity [8, 32]. These variables are provided by meteorological reanalysis from data assimilation systems like the NASA Modern Era Retrospective analysis for Research and Applications V2 (MERRA-2) [27] and the European Center for Medium-Range Weather Forecasts (ECMWF) ERA5 [35], which assimilate observations. The accuracy of the meteorol-

ogy therefore affects the accuracy of contrail simulations.

Reanalysis data can be used for global climate monitoring, initializing weather forecasts, and climate predictions, being used for applications including wildfire monitoring [86], storm-surge modeling [87] and offline air quality simulations [88]. Studies have shown improvements of reanalyses in both tropospheric and stratospheric conditions over the past several decades [89–92]. However, recent studies have shown that reanalyses tend to overestimate upper tropospheric water vapor by up to 150% [28], limiting their suitability for studies focused on these altitudes [29]. Such trends have also been observed in studies [30, 31] comparing the likelihood of persistent contrail formation from climate simulations and ECMWF's Integrated Forecast System against satellite measurements. These studies, however, do not provide a comprehensive and quantitative comparison between simulation data and measurements.

The frequency of occurrence and size of ice supersaturated (ISS) regions, in which contrails can persist, has been studied using radiosondes in many studies [85, 93–96]. These have typically used the RS80 sensor, which has a temperature-dependent time lag (approximately 80 s at -50°C). This time lag means that peaks in the relative humidity may not be picked up by RS80 sensors, leading to undetected ISS regions. This lag is around a factor of $2-3$ smaller for the RS92 sensor, reducing the likelihood of missing ISS regions [97]. The sensor is also affected by radiative heating that can lead to a dry bias during the daytime. Comparisons with frost-point hygrometers, an accurate approach to measure upper tropospheric humidity, suggest a mean dry bias of up to 5% in the RS92 sensor at humidities between 29% - 99% in the day and up to 40% in the night [98]. Aircraft and satellite-derived estimates of upper tropospheric humidity can also be used. Satellite-based measurements have a coarse vertical resolution (e.g.; Aura microwave limb sounder has a vertical resolution of $1.3-3.6$ km [99]), so are unable to detect contrail forming regions shallower than approximately 1 km. Aircraft-based measurements are unable to match the consistent global coverage of radiosonde launches and do not provide vertical snapshots of the atmosphere.

This thesis estimates the bias in using reanalysis data to simulate contrails. I

quantify the likelihood of persistent contrail formation in 793,044 profiles – measurements from a given sonde launch – from the Integrated Global Radiosonde Archive [100], comparing this to results based on MERRA-2 and ERA5 data. I cover a five-year period from 2012 – 2016 (inclusive), using only RS92 sensor data to minimize systematic biases. For each launch, I extract the corresponding vertical temperature and humidity profile from reanalysis data based on the sonde launch location, permitting fair comparison.

I first quantify the likelihood a persistent contrail would form in each profile if an aircraft passed through it. I estimate whether each vertical profile – observed and simulated – satisfies the persistent contrail condition (PCC). The PCC requires that the air meet the Schmidt-Appleman Criterion [6–8] (SAC), permitting contrail formation, and that the air is ISS, permitting contrail persistence. To provide an estimate of overall likelihood of persistent contrail formation, I integrate the PCC profile weighted by the global mean aviation fuel burn (see Methods).

I also provide estimates of contrail longevity by computing an "evaporation depth" metric for each profile at 10 km. This measures the vertical distance newly formed ice crystals could fall before evaporating, a proxy for contrail lifetime. Each of these quantities is calculated using the sonde data as an approximate "ground truth", and then using collocated reanalysis data.

3.2 Method

3.2.1 Integrated global radiosonde archive (IGRA)

For this thesis, I use radiosonde data from the IGRA V2 from 2012 to 2016 [101, 102]. The soundings are generated from 2,788 stations globally, 1,081 of which contribute between 2012 to 2016. The instruments used in each sounding can vary depending on year and country. To be consistent between stations and times, I use only those stations which use the Vaisala RS92 sensor. This choice is a compromise between the need for a widely used sensor, to ensure sufficient coverage, and the need for accurate

readings. The RS92 is used at 360 of the 1,081 contributing stations, providing global coverage (see Figure 3-1). This sensor has also been shown to measure temperature and relative humidity - the two measurements required for estimating contrail formation and persistence - to within ±1 K and 10%, respectively [98, 103]. The RS92 sensor is known to have a daytime dry bias due to radiation error of around 30% at 10 km and 50% at 15 km for humidity [104]. Information on sensors used by station is available from the WMO [105].

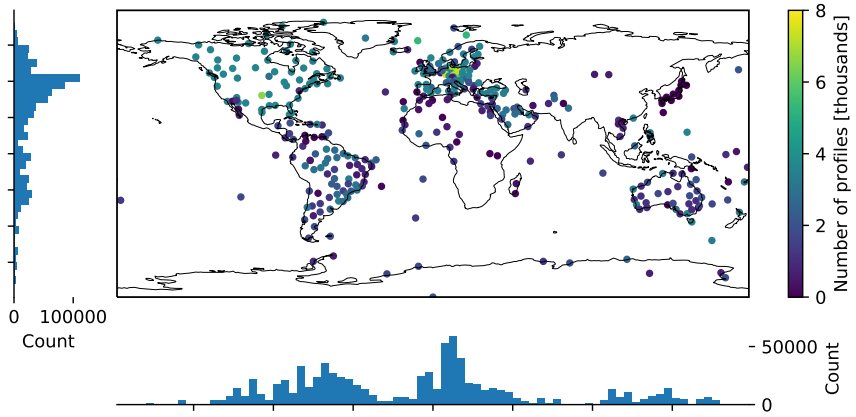

Figure 3-1: Number of profiles by stations using the RS92 sensor in 2012 – 2016. Main panel shows the locations colored by the number of profiles over the five-year period. Left panel shows the distribution of profiles by latitude and the lower panel the distribution by longitude.

The number of RS92 sonde launches for each station globally between 2012 and 2016 is shown in Figure 3-1. The 360 stations using the RS92 sensor and providing humidity readings globally launched 930,091 sondes ("profiles") in this time period. Observations with not-an-number (NaN) readings for any of pressure, temperature or dewpoint depression are removed. Profiles where the vertical distance between observations is greater than 3 km or where all observations are below 12 km are removed. These two requirements account for 14.7% of profiles and our results use the remaining 793,044.

The distribution of stations and profiles varies by latitude band as seen in Figures 3-1 and 3-2. 48% of profiles are in the northern mid-latitudes (30°N – 60°N). The

number of profiles increases by 9.8% from 2012 to 2016 and the number of profiles varies by up to 13% between seasons. By latitude band, I find the distribution of profiles is heavily skewed towards the Northern Hemisphere representing 75% of profiles, with the fewest profiles in the Antarctic (2.0%) and Southern mid-latitudes (6.5%). Finally, 54% of the sondes are launched during the day, with this proportion increasing from 53.6% in 2012 to 54.6% in 2016. Sondes are typically released twice a day at noon and midnight. This is reflected in the IGRA data where 98.5% of sondes are launched at 3-hour intervals (i.e. 3 AM UTC, 6 AM UTC, 9 AM UTC etc.), matching the output time of both reanalysis data.

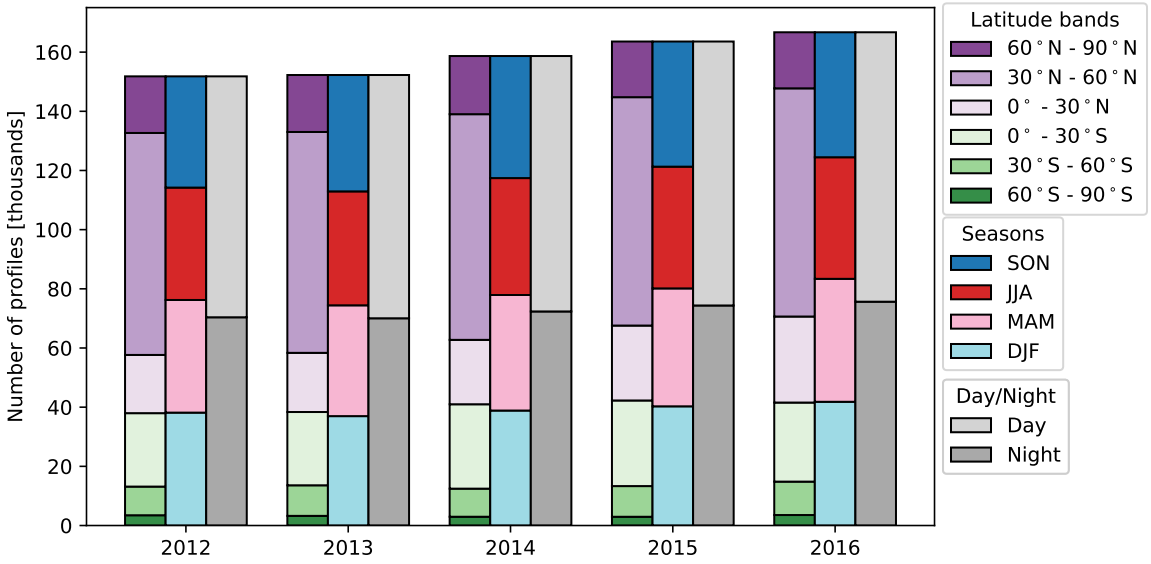

Figure 3-2: Profile distribution for each year, separated by latitude band, season and day versus night. Left stacked bars for each year show the distribution by latitude bands. Northern Hemisphere bands are shown in purple and Southern Hemisphere in green, with darker colors representing higher latitudes. The middle stacked bars show the distribution by season where blue is September, October and November (SON), red is June, July and August (JJA), pink is March, April and May (MAM) and light blue is December, January and February (DJF). The right stacked bars show the distribution by day versus night, where day is defined by a positive solar zenith angle.

The selected locations of sondes are not uniformly distributed around the globe. This means that they may not be representative of the overall meteorological conditions. To assess whether they are representative, I use the persistent contrail criteria

(PCC). The PCC quantifies the likelihood of a persistent contrail forming if an aircraft passed (see Section 3.2.4 for further information) for the purposes of the PCC distribution, Figures 3-3 and 3-5 show the percentage PCC in the northern mid-latitudes for DJF and JJA comparing the sonde data with collocated ERA5 profiles, all ERA5 profiles in the given latitude band and season, and all ERA5 profiles on land locations also in the given latitude band and season. The mean cruise-altitude PCC in DJF is 10% lower than the data at sonde locations for ERA5 and 12% lower for MERRA-2. In comparison, in JJA, the mean cruise-altitude PCC is 46% higher than the simulated value for ERA5 and 34% higher for MERRA-2. This suggests a seasonal bias in how representative the temperature and humidity data of the sonde data is for persistent contrail formation. Including the PCC distribution for land locations only does not explain the differences between reanalysis data at sonde versus all locations.

Humidity measurements in the sonde data are provided as a dew point depression ($T - T_d$), which measures the difference between the ambient temperature, T, and the dew point temperature, T_d. The dew point temperature measures the temperature to which air must be cooled to become saturated with respect to water. The dew point temperature can be converted to the water vapor partial pressure as

$$p_{\text{wv}} = ae^{\frac{bT_d}{c+T_d}} \tag{3.1}$$

where p_{wv} is the water vapor partial pressure, T_d is the dewpoint temperature and $a = 611.2$ Pa, $b = 17.67$ K^{-1} and $c = 243.5$ K are fitted coefficients [106]. This is converted to a relative humidity by estimating the saturation water vapor partial pressure as [106]

$$p_{\text{wv}}^{\text{sat}} = 100e^{\frac{-6096.9385}{T}+16.635794-0.02711193T+1.673952\times10^{-5}T^2+2.433501\log(T)} \tag{3.2}$$

I estimate altitude based on pressure data. Each data point is considered to represent a layer with constant temperature from the lower to upper edge of the layer. A layer is defined by the geometric mid-point between consecutive observations. The

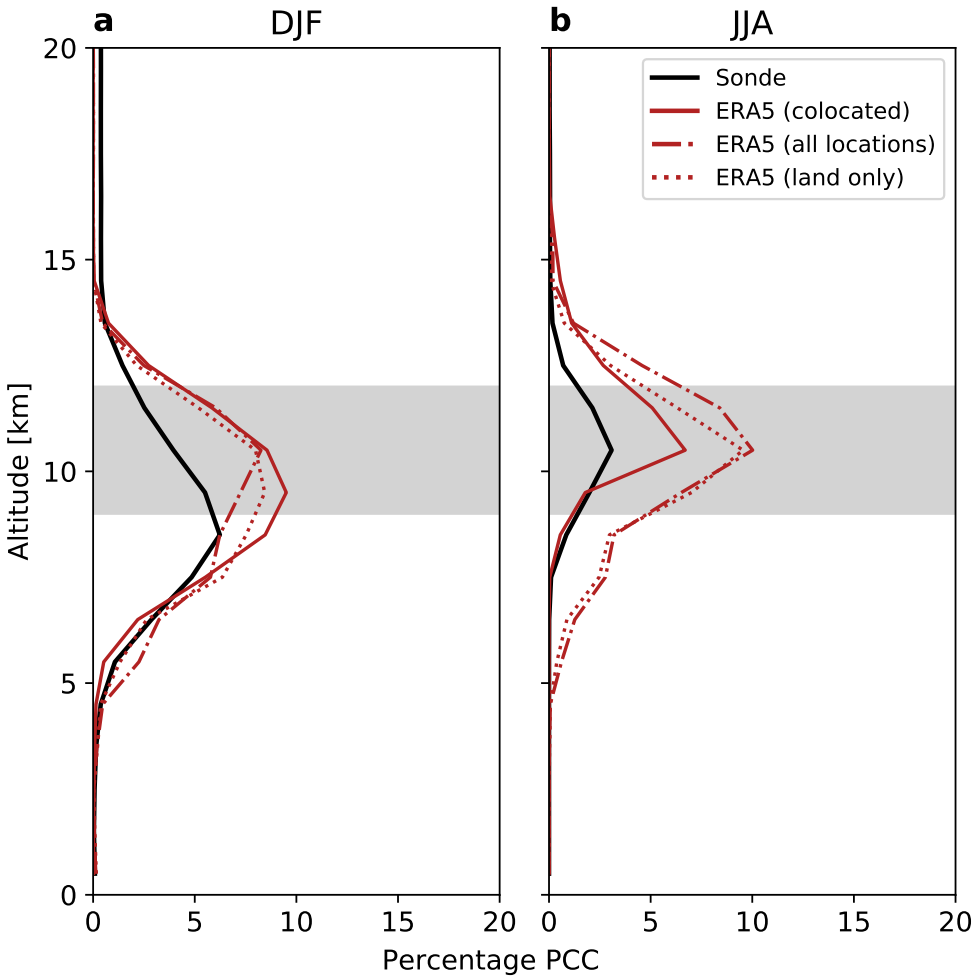

Figure 3-3: Percentage of profiles that satisfy the PCC for 30°N – 60°N for (a) DJF and (b) JJA. Sonde observations are shown in the black, solid lines, ERA5 at matching sonde locations in the red, solid lines, ERA5 at all locations in 30°N – 60°N and the respective season in the red, dash-dotted lines, and ERA5 at all land locations in 30°N – 60°N and the respective season in the red, dotted lines. The grey shaded region represents the range of aircraft cruise altitudes (9 – 12 km).

barometric formula with constant temperature is used to estimate the difference in altitude between the upper and lower edge of the layer. The altitude is initialized assuming the highest recorded pressure value is at the surface. I therefore calculate

$$z_+ = z_- + \frac{RT}{gM} \log\left(\frac{p_-}{p_+}\right) \tag{3.3}$$

where z_+ and z_- are the altitude of the upper and lower edge of the layer, respectively, $R = 8.31$ J/(mol K) is the universal gas constant, $g = 9.81$ m/s is the

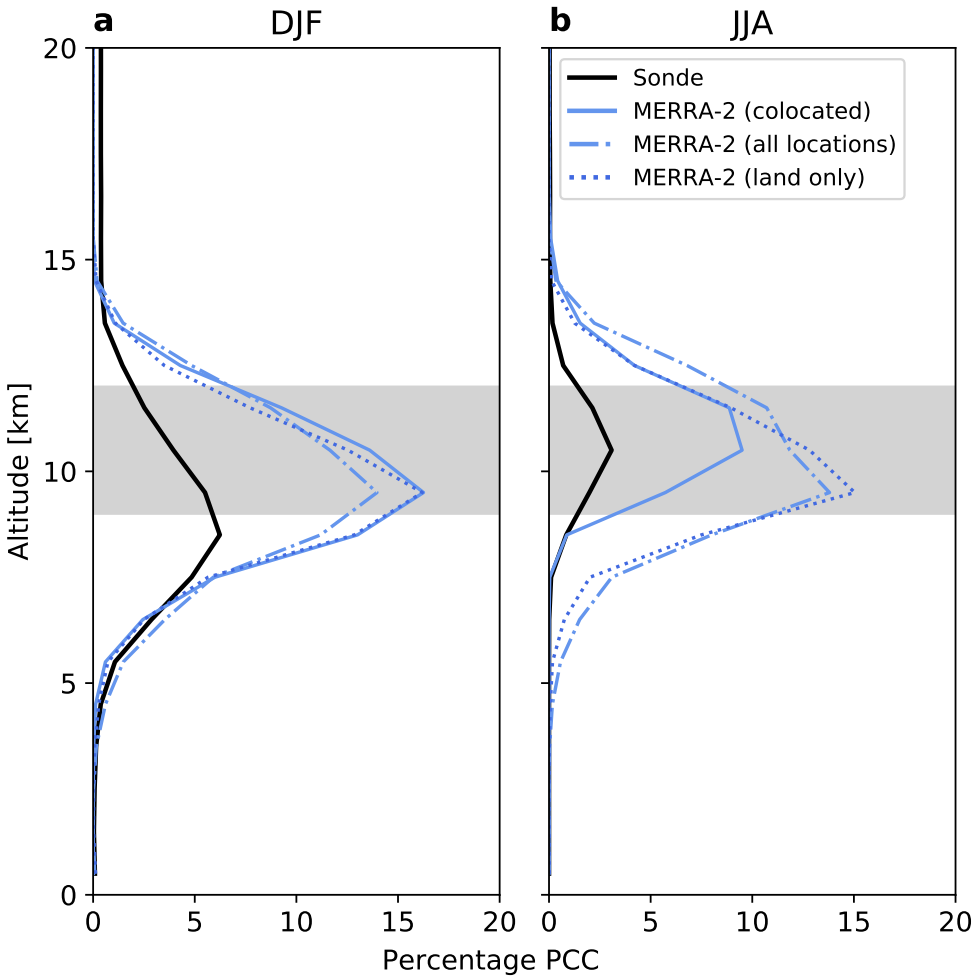

Figure 3-4: Percentage of profiles that satisfy the PCC for 30°N – 60°N for (a) DJF and (b) JJA. Sondes observations are shown in the black, solid lines, MERRA-2 at matching sonde locations in the red, solid lines, MERRA-2 at all locations in 30°N – 60°N and the respective season in the red, dash-dotted lines, and MERRA-2 at all land locations in 30°N – 60°N and the respective season in the red, dotted lines. The grey shaded region represents the range of aircraft cruise altitudes (9 – 12 km).

gravitational acceleration at the surface of the Earth, $M = 0.028$ kg/mol is the average molecular mass of air and p_+ and p_- are the pressure of the upper and lower edge of the layer, respectively.

3.2.2 Reanalysis data

Two reanalysis datasets are tested in this thesis: the Modern Era Retrospective analysis for Research and Applications V2 (MERRA-2)15 and the European Center for

Medium-Range Weather Forecasts' (ECMWF) ERA5 [35]. The reanalysis data are generated from data assimilation models that combine numerical simulations with a wide range of atmospheric observations.

MERRA-2 is generated from the Goddard Earth Observation System model, Version 5 (GEOS5) and is the latest reanalysis product from the Global Modeling and Assimilation Office (GMAO). It was built off version 1 of MERRA [107] and changes between versions are described in the literature. MERRA-2 uses a cube-sphere horizontal discretization with a resolution of around $0.5^\circ \times 0.625^\circ$ (~50 km) and 72 hybrid-eta levels from surface to 0.1 hPa. For this study, the 3-hourly, $0.5^\circ \times 0.625^\circ$, 72-layer data was used. Humidity data is assimilated using the normalized pseudorelative humidity and a complete set of the data assimilated is provided in the literature [27]. MERRA-2 assimilates radiosonde and other water vapor observations until 300 hPa since the accuracy of radiosonde water vapor observations at lower pressures is lower [29].

ERA5 is the second global reanalysis data used in this thesis. It is based on 4D-Var data assimilation using Cycle 41r2 of the Integrated Forecasting System (IFS). ERA5 is a spectral model at the TL639 resolution (31 km) with 137 layers to 1 hPa. For this study, the hourly $0.25^\circ \times 0.25^\circ$ with 37 layers was used, provided from the Copernicus Data Store (CDS). ERA5 assimilates radiosonde and other water vapor observations until the diagnosed tropopause at ~300 hPa [29].

Radiosonde profiles are collocated to the same time and locations based on the sonde release data. Additional temporal or spatial location information as the sonde rises is not provided in the sonde data. The grid-average values are used from both ERA5 and MERRA-2 and I retain all vertical layers from ground to the highest for which observations are available for each individual profile.

3.2.3 GRUAN

The global climate observing system (GCOS) reference upper air network (GRUAN) provides state-of-the-art, high quality humidity measurements from radiosondes [103]. These measurements use the RS92 sensor, but are corrected for time-lag, radiation dry

bias and other errors. Detailed uncertainty estimates are also provided by GRUAN. GRUAN only provide data for 32 locations and thus are unable to provide global trends like the IGRA dataset. However, the accuracy and uncertainty data is used as a benchmark to compare to IGRA and reanalysis data. In this section, I provide an overview of how uncertainties in temperature and humidity are propagated to the PCC.

GRUAN separate uncertainties in temperature and humidity measurements (including corrections) according to whether they are correlated or uncorrelated. In addition, a method to combine uncertainties across several observations in a given profile is provided [108]. The uncertainty of the average conditions across M observations in a given profile, l, is calculated as

$$\overline{k_{i,l}} = \sum_{j=i-M}^{j=i+M} k_{i+j,l} \tag{3.4}$$

$$\overline{r_{i,l}} = \sum_{j=i-M}^{j=i+M} r_{i+j,l}^2 \tag{3.5}$$

where k_{i+j} and r_{i+j} represents the (perfectly) correlated and uncorrelated uncertainties at observation $i+j$, respectively, and $2M$ represents the number of observations in the layer depth. Each observation's uncertainty is calculated using data provided in each GRUAN dataset.

The combined uncertainty of the average signal of profile l, $\overline{u_{i,l}}$, is

$$\overline{u_{i,l}} = \sqrt{\overline{k_{i,l}}^2 + \overline{r_{i,l}}^2} \tag{3.6}$$

I must now combine uncertainties across multiple profiles with observations in the same layer. I assume that $\overline{u_{i,l}}$ is independent and uncorrelated across profiles, allowing me to calculate the combined uncertainty, $\widehat{u_i}$, using quadrature as

$$\widehat{u_i} = \frac{1}{N}\sqrt{\sum_{i=1}^{N} u_{i,l}} \tag{3.7}$$

To propagate uncertainties in temperature and relative humidity for the PCC, I

can define the PCC in terms of four auxiliary variables, X_i, that all must be greater than zero as

$$\mathrm{PCC} = \prod_{i=1}^{4} [[X_i > 0]] \tag{3.8}$$

where $[[\dots]]$ is the Iverson brackets, which maps the statement within to it's possible values (e.g. true when $X_i > 0$, false otherwise). Each condition follows the definitions of the SAC or ISS and are defined as

$$X_1\left(T, p\right) = T_c(p) - T \tag{3.9}$$

$$X_2\left(\mathrm{RH}, T, p\right) = \mathrm{RH} - \mathrm{RH}_c(T, p) \tag{3.10}$$

$$X_3(\mathrm{RH}, T) = \mathrm{RH}\frac{p_{\mathrm{wv}}^{\mathrm{sat}}(T)}{p_{\mathrm{ice}}^{\mathrm{sat}}(T)} - 1 \tag{3.11}$$

$T_c(p)$ is defined as [109]

$$T_c(p) = 226.69 + 9.43 \ln\left[G(p) - 0.053\right] + 0.72 \ln\left[G(p) - 0.053\right]^2 \tag{3.12}$$

where $G(p)$ is the gradient of the mixing between the ambient air and engine exhaust conditions on the temperature-water vapor partial pressure curve. It is defined as [109]

$$G(P) = \frac{\mathrm{EI}(\mathrm{H_2O}) c_p p}{0.622 \mathrm{LHV}(1 - \eta_o)} \tag{3.13}$$

where $c_p = 1004$ J/K/kg is the specific heat capacity of air, p is the ambient pressure, $\mathrm{EI}(\mathrm{H_2O}) = 1.23$ kg/kg is the mass of water emitted per mass of fuel burned, $M_{\mathrm{air}} = 28.97$ g/mol and $M_{\mathrm{H_2O}} = 18.02$ g/mol is the molecular mass of air and water, respectively, LHV $= 43.13$ MJ/kg is the lower heating value of aviation fuel and $\eta_o = 0.35$ is the engine overall efficiency. η_o is equal to the propulsive efficiency (η_p)

multiplied by the thermal efficiency (η_t). While fuel and ambient air properties are relatively fixed globally and for each aircraft, η_o can vary by 10 – 15 percentage points depending on engine technology and mode of operation [110]. I assume $\eta_o = 0.35$ as a mid-point between currently used engines as well as new engines that have recently entered the market. Prior studies [111] have estimated $\eta_o = 0.31$ for the year 2006 using the BADA dataset [112].

$RH_c(T, p)$ is defined as [109]

$$RH_c(T, p) = \frac{G(p)(T - T_c(p)) + p_{\text{wv}}^{\text{sat}}(T_c)}{p_{\text{wv}}^{\text{sat}}(T)} \tag{3.14}$$

Assuming each measured variable is randomly distributed with mean, μ_ϵ, and uncertainty, σ_ϵ^2, and uncorrelated with each other, then the combined uncertainty is modeled as

$$X_i \sim \mathcal{N}(X_i(\mu_{\epsilon_1}, \ldots, \mu_{\epsilon_m}), \sigma_{X_i}^2) \tag{3.15}$$

where the variance is found as

$$\sigma_{X_i}^2 = \sum_{j=1}^{m} \frac{\partial X_i}{\partial \epsilon_j}^2 \sigma_{\epsilon_j}^2 \tag{3.16}$$

This also assumes that T and RH are uncorrelated with each other. While I do expect these variables to be correlated, GRUAN do not provide information on the correlation coefficient between the T and RH uncertainties. If this information became available, the T and RH measurements can be modeled by a multivariate Gaussian distribution with its mean equal to the nominal measurement values and its covariance matrix equal to

$$\Sigma = \begin{bmatrix} \sigma_T^2 & \rho\sigma_T\sigma_{\text{RH}} \\ \rho\sigma_T\sigma_{\text{RH}} & \sigma_{\text{RH}}^2 \end{bmatrix} \tag{3.17}$$

The probability PCC is then found as

$$P\left(\mathrm{PCC}\right) = \prod_{i=1}^{4} P\left(X_i > 0\right) = \prod_{i=1}^{4} \phi\left(\frac{\mu_{X_i}}{\sigma_{X_i}}\right) \tag{3.18}$$

Assuming that each estimate of $P\left(\mathrm{PCC}\right)$ is independent, I can estimate the proportion of a layer that satisfies the PCC as

$$\overline{P\left(\mathrm{PCC}\right)_{i,l}} = \sum_{j=i-M}^{j=i+M} P\left(\mathrm{PCC}\right)_{i+j,l} dz_{i+j,l} \tag{3.19}$$

where $dz_{i+j,l}$ is the distance between the midpoint of the given observation and adjacent observations. The variance of this distribution is

$$\overline{V\left(\mathrm{PCC}\right)_{i,l}} = \sum_{j=i-M}^{j=i+M} P\left(\mathrm{PCC}\right)_{i+j,l} \left(1 - P\left(\mathrm{PCC}\right)_{i+j,l}\right) dz_{i+j,l}^2 \tag{3.20}$$

3.2.4 Metrics

To quantify the likelihood of contrail formation and persistence, I define the persistent contrail condition (PCC). The PCC identifies whether a contrail could both form and persist in the local conditions, if an aircraft passed. Satisfying the PCC means satisfying three conditions: (a) the air must be supersaturated with respect to ice ($\mathrm{RH_i} > 100\%$); (b) the relative humidity with respect to water must be above the critical ambient relative humidity with respect to water ($\mathrm{RH_w}$>$\mathrm{RH_c}$ (see Eq 3.14)) at some point while the plume mixes with ambient air; and (c) the relative humidity with respect to water must be below 100% ($\mathrm{RH_w} < 100\%$).

RH_i is calculated as

$$RH_i = RH_w \frac{p_{\mathrm{wv}}^{\mathrm{sat}}}{p_{\mathrm{ice}}^{\mathrm{sat}}} \tag{3.21}$$

where RH_w is the measured relative humidity with respect to water, and $p_{\mathrm{ice}}^{\mathrm{sat}}$ is the estimated saturated partial pressure with respect to ice. This is approximated as [113]

$$p_{\text{ice}}^{\text{sat}} = 100e^{(\frac{-6024.5282}{T}+24.7219+0.010613868T+1.319883\times10^{-5}T^2+0.49382577\log(T)} \tag{3.22}$$

where T is the local, measured air temperature in Kelvin.

Multiplying the PCC at a given altitude (averaged over time) by the likelihood of a flight passing through that altitude gives a metric of the frequency with which contrails will form at the location. For a given vertical profile, I use the vertical distribution of aviation fuel burn as a proxy for the likelihood that aircraft will be present at that altitude. Accordingly, I calculate the fuel burn weighted PCC, F_{PCC}, at any given time t as

$$F_{\text{PCC}} = \frac{\int P_{\text{PCC}}(z)F(z)dz}{\int F(z)dz} \tag{3.23}$$

where $P_{\text{PCC}}(z)$ is the proportion of space-time that satisfies the PCC, $F(z)$ is the fuel burn profile and z is the vertical coordinate. F_{PCC} thus represents the proportion of the vertical fuel burn profile in a region that could lead to a persistent contrail forming. It is calculated from the Aviation Environmental Design Tool (AEDT) [114] for 2015 flight operations. I use a global, annual average value as aviation fuel burn varies by less than 25% between a summer peak and winter trough [115]. The vertical profile is also not expected to change between seasons or within the latitude bands considered.

The final metric used is the evaporation depth, d_e, which measures the depth below a specific altitude at which the area between the water concentration and ice saturation concentration profile is zero. For this thesis, I specify the initial altitude, Z_0, to be 10 km. It is calculated by solving the equation

$$\int_{Z_0-d_e}^{Z_0} \left(C_{\text{H}_2\text{O}} - C_{\text{H}_2\text{O}}^{\text{sat}}\right) = 0 \tag{3.24}$$

where $C_{\text{H}_2\text{O}}$ is the water vapor concentration, and $C_{\text{H}_2\text{O}}^{\text{sat}}$ represents the saturation water vapor concentration.

Throughout this thesis, I use a range of error metrics including the mean absolute error (MAE), mean factor error (MFE), normalized mean bias (NMB) and correlation coefficient (R^2). The MAE is calculated as

$$\text{MAE} = \frac{1}{N}\sum_{i}^{N}|y_{o,i} - y_{e,i}| \tag{3.25}$$

where y_o represents the observation from the sonde data and y_e the estimate from the reanalysis data. The MFE is calculated as

$$\text{MFE} = \frac{1}{N}\sum_{i}^{N}\frac{y_{e,i}}{y_{o,i}} \tag{3.26}$$

Finally, the NMB is calculated as

$$\text{NMB} = 100\frac{\sum_i y_{e,i} - y_{o,i}}{\sum_i y_{o,i}} \tag{3.27}$$

3.3 Results

3.3.1 Formation of persistent contrails

The proportion of the vertical profile that is ISS by latitude is shown in Figure 3-5. Given that the sonde locations are not uniformly distributed globally, they may not be representative of the overall meteorological conditions in a region and/or timeframe. For this reason, I present quantities averaged by latitude and season, rather than on individual observations. Comparisons between collocated reanalysis profiles with reanalysis data at all locations are shown in Figures 3-3 and 3-5 for ERA5 and MERRA-2, respectively and are further described in the Methods.

The proportion of the vertical profile that satisfies the PCC is shown in Figure 3-6, aggregated into three latitude bands. Typical subsonic cruise altitudes (9 – 12 km) are shaded in grey on each panel of Figure 3-6. The mean cruise-altitude PCC is overestimated in both reanalysis models by a factor of 1.3 to 3.5. This bias factor is highest in the mid-latitudes, at 2.0 for ERA5 and 3.5 for MERRA-2, and lowest in the Arctic, at 1.3 and 1.8, respectively. This deviation by latitude could lead to

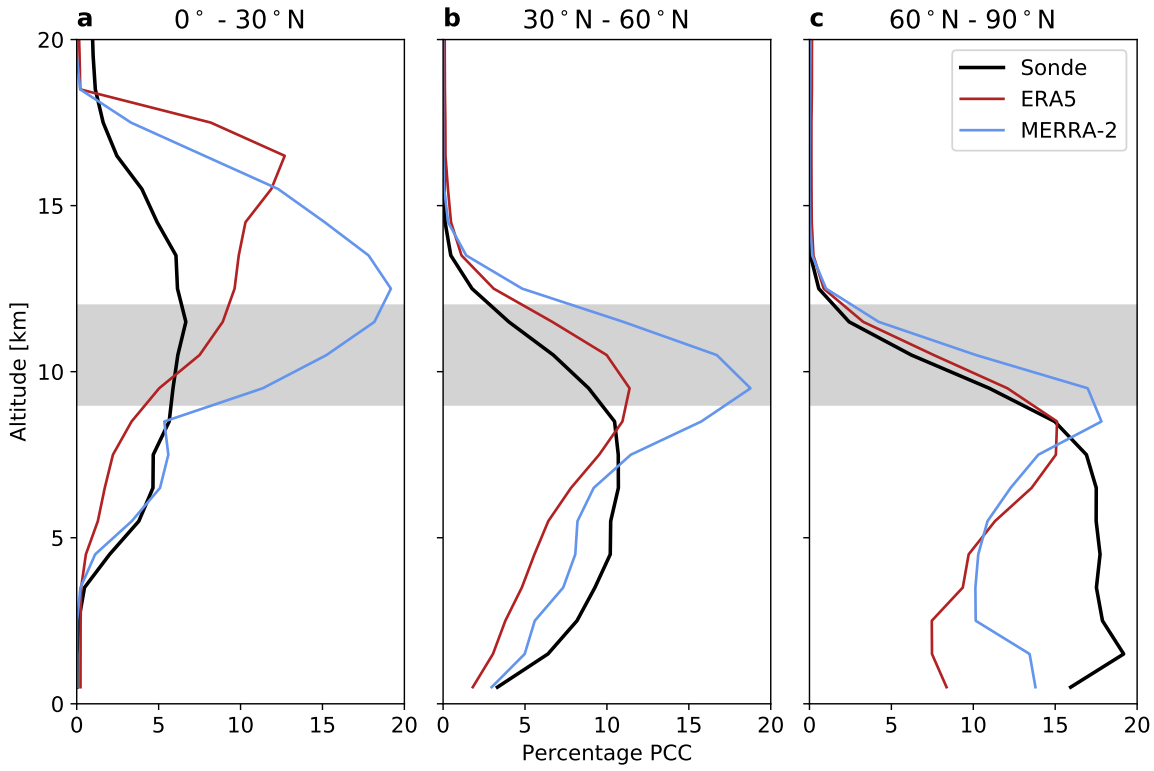

Figure 3-5: Proportion of annual average profile that is ice supersaturated (ISS) separated by latitude. ISS profile in 0° - 30°N (a), 30°N - 60°N (b) and 60°N - 90°N (c) for sonde observations (black), ERA5 (red) and MERRA-2 (blue). The grey shaded region represents the range of aircraft cruise altitudes (9 – 12 km).

spurious trends in global estimates when traffic patterns vary over time. These biases also vary with altitude and could result in additional errors when studying the effects of future supersonic aircraft, which are expected to cruise at altitudes between 15 km and 20 km [116].

Sonde observations show that the mean PCC-weighted altitude (i.e., first moment) decreases as I move poleward, from 14 km in the tropics (0° - 30°N) to 8.1 km in the Arctic (60°N - 90°N). This decrease is reproduced by ERA5 and MERRA-2. In the tropics, ERA5 overestimates the first moment by 430 m, while MERRA-2 underestimates it by 410 m. In the Arctic, ERA5 overestimates the first moment by 590 m and MERRA-2 underestimates it by 322 m. Seasonal differences and other analyses are shown in Figure 3-7.

I also quantify the variation in these errors by season. Previous studies have found

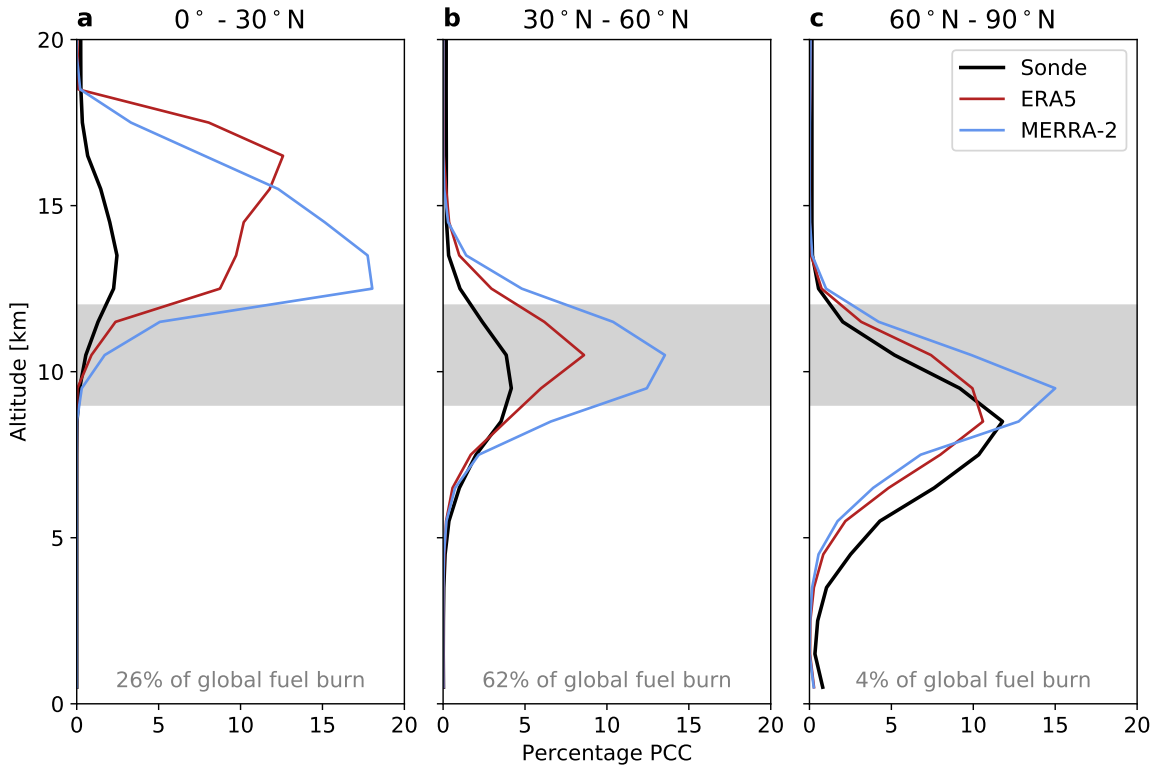

Figure 3-6: Proportion of annual average profile that satisfies the PCC, separated by latitude. PCC profile in 0° - 30°N (a), 30°N - 60°N (b) and 60°N - 90°N (c) for sonde observations (black), ERA5 (red) and MERRA-2 (blue). The grey shaded region represents the typical range of aircraft cruise altitudes (9 – 12 km). The proportion of global aviation fuel burn in each latitude band is shown at the bottom of each subplot.

that although only 22% of annual air traffic occurs during Northern hemispheric winter, over half of the expected annual mean radiative forcing from contrails occurs during this period [117]. Figure 3-8 shows how the observed and simulated PCC profiles vary between Northern Hemisphere winter (DJF) and summer (JJA) for the northern midlatitudes, covering 62% of global aviation fuel burn.

Based on sonde data, differences in the vertical PCC profile are dominated by changes which occur between 5 and 11 km. Above 11 km, the percentage PCC is roughly the same across seasons, with a 24% reduction from DJF to JJA at 11 km. However, between 5 and 11 km, the mean percentage PCC is a factor of 4.1 greater in DJF than in JJA. The shape of the profile within the cruise altitude region also changes. In DJF, the peak PCC likelihood occurs below 9 km, and decreases with

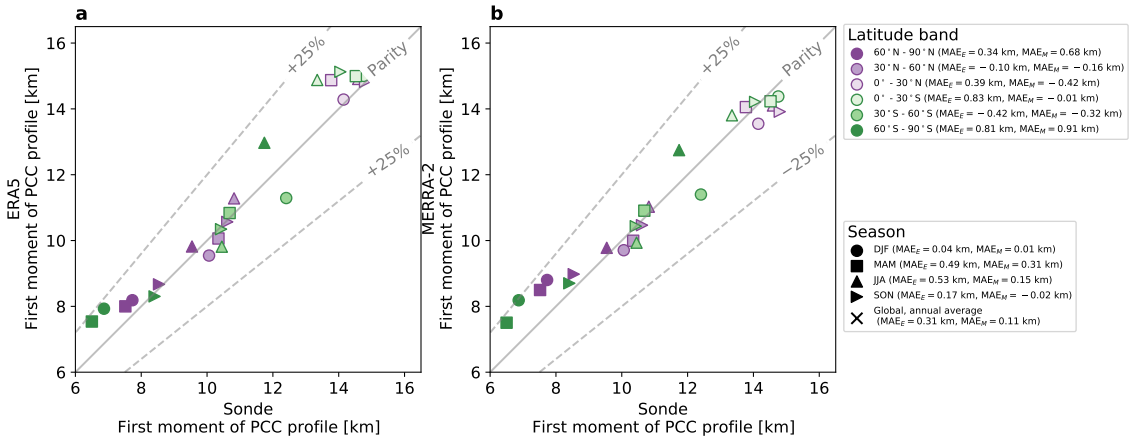

Figure 3-7: Parity plot of first moment of PCC profile [km]. Results are separated by mode: (a) ERA5 and (b) MERRA-2. Latitude bands are separated by color with purple representing the Northern Hemisphere and green the Southern Hemisphere. Darker colors represent higher latitudes. Seasons are represented by markers with DJF in circles, MAM in squares, JJA in upward-facing triangles and SON in rightward facing triangles. Global, annual average results are also included in the black cross.

increasing altitude. In JJA, the peak instead occurs at 11 km. Combined, these differences result in a mean cruise-altitude PCC proportion during DJF which is three times greater than during JJA. This seasonal trend is also reflected in contrail observation studies [118, 119].

Meteorological reanalysis data qualitatively reproduce observed seasonal variations in overall PCC likelihood. However, both ERA5 and MERRA-2 overestimate the mean cruise-altitude PCC. ERA5 overestimates this by a factor of 2.0 across both seasons. MERRA-2 shows an overestimate of a factor of 3.4 and 3.6 in DJF and JJA, respectively. Both reanalysis models also overestimate the increase in the mean PCC altitude from DJF to JJA. The sonde data show a 7.6% increase while in ERA5 and MERRA-2, I find a 19% and 14% increase, respectively.

3.3.2 Fuel burn weighted PCC

I use the fuel-burn weighted PCC to produce a single, aviation-specific performance metric which can be compared between locations. This metric measures the percentage of aviation fuel burn that could lead to the formation of a persistent contrail. The variation of fuel-burn weighted PCC over the full 2012 – 2016 period is shown

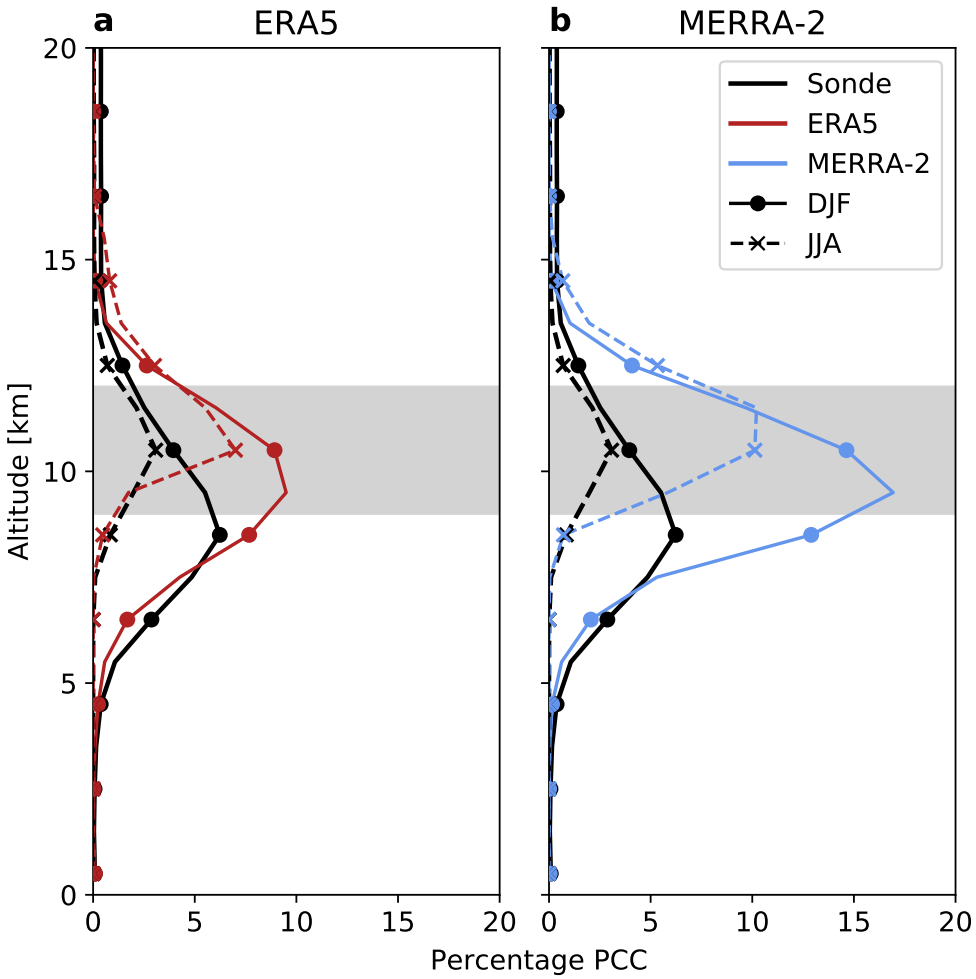

Figure 3-8: Seasonal variation in the proportion of the average profile that satisfies the PCC for 30°N – 60°N. Trends for DJF (solid line with filled circles) and JJA (dashed line with crosses) are shown for (a) sonde compared with ERA5 and (b) sonde compared with MERRA-2. The grey shaded region represents the range of aircraft cruise altitudes (9 – 12 km).

in Figure 3-9 for each latitude band. The correlation coefficient (R^2), mean absolute error (MAE), and normalized mean bias (NMB) are calculated between each reanalysis data time series and the sonde data and provided in the legend. Each time series is a daily average of all fuel-burn weighted PCC.

For all latitudes, the reanalysis data overestimates the fuel-burn weighted PCC. The greatest NMB occurs at mid-latitudes, where 62% of aviation fuel is burned. ERA5 shows a bias of 44%, while MERRA-2 has a bias that is a factor of 3.1 greater. Both reanalysis data show a positive bias in the tropics and Arctic. For ERA5, this

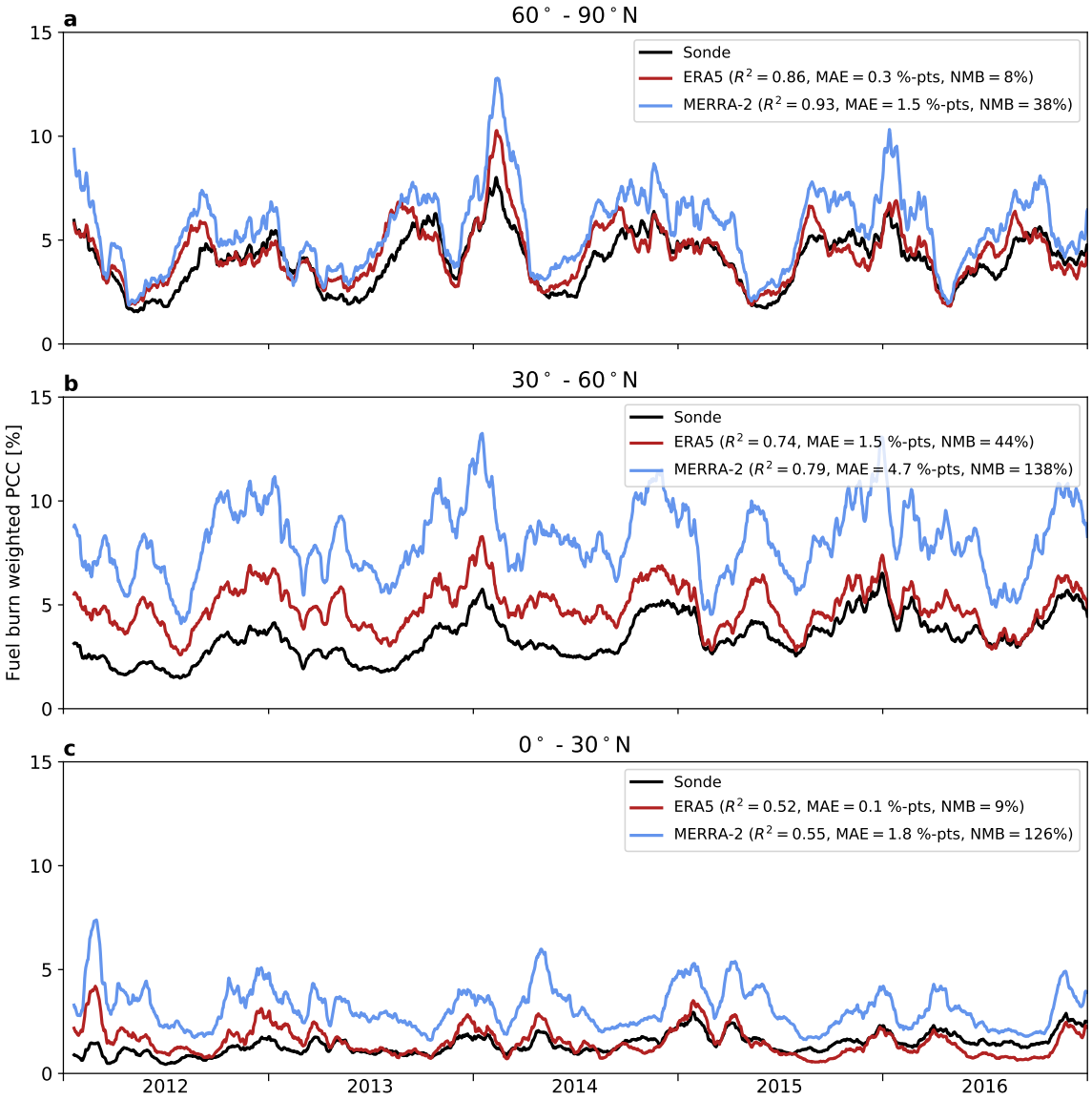

Figure 3-9: 30-day rolling mean time series of daily averaged fuel burn weighted PCC separated by latitude band. Time series are shown for 60°N - 90°N (a), 30°N - 60°N (b) and 0° - 30°N (c) for sonde observations (black), ERA5 (red) and MERRA-2 (blue). For ERA5 and MERRA-2, the correlation coefficient (R2), mean absolute error (MAE) in units of percentage points (%-pts), and normalized mean bias (NMB) between sonde and reanalysis time series are shown in each legend.

bias is +9% and +8%, respectively. In comparison, for MERRA-2, the bias is +126% in the tropics and +38% in the Arctic.

I use the coefficient of determination to assess the extent to which temporal variations in fuel-burn weighted PCC are well-represented in the reanalysis data. MERRA-

2 achieves an R^2 of 0.55 in the tropics and 0.93 in the Arctic. This suggests that, in spite of the normalized mean bias, MERRA-2 captures a large fraction of the seasonal variability in persistent contrail formation. ERA5 is also able to capture the seasonal variability with an R^2 of 0.52 in the tropics and 0.86 in the Arctic.

I also quantify the effect of engine overall efficiency (η_o) on the fuel burn weighted PCC (Figure 3-10). Increasing η_o is expected to lead to an increase in the likelihood of contrail formation [8]. In the sonde data, I find that an increase in η_o from 0.30 to 0.40 causes the fuel burn weighted PCC to increase by approximately 9.4%. This increase in fuel burn weighted PCC varies with time between a maximum of 14% and minimum of 5.8%. The sensitivity to efficiency is similar in ERA5 and MERRA-2, with a mean increase in fuel burn weighted PCC of 11% and 9.8%, respectively. Both models exhibit a larger variability over the five-year period studied, with the percentage change in fuel burn weighted PCC varying between 4.4% - 26% for MERRA-2 and 6.2% - 21% for ERA5. This could lead to unexpectedly strong seasonal or latitudinal variations in model-based predictions that would not be reproduced in reality.

The fuel burn weighted PCC can also be aggregated to a single metric for each latitude band and season as shown in Figure 3-11, with the mean factor error (MFE, see Eq 3.26) shown in the legend. MERRA-2 overestimates the fuel burn weighted PCC in all cases, while ERA5 overestimates in all but two cases (0° – 30°S in DJF and 60°S – 90°S in JJA). In addition, the MFE is higher for MERRA-2 than ERA5 in all cases except 60°S – 90°S. Finally, the MFE is greatest for ERA5 and second greatest for MERRA-2 in the northern mid-latitudes, where the 62% of fuel is burned.

3.3.3 Contrail longevity

Contrail lifetime is determined by the time taken for contrail ice crystals to fall into sub-saturated air and evaporate. Initially, ice crystals fall and grow in supersaturated conditions until the relative humidity with respect to ice, $RH_i = 100\%$. Once they reach subsaturated conditions, they lose ice mass until the surrounding air reaches an $RH_i = 100\%$. As they continue to fall in subsaturated conditions, they will lose more ice mass until they evaporate. The evaporation depth thus measures the vertical

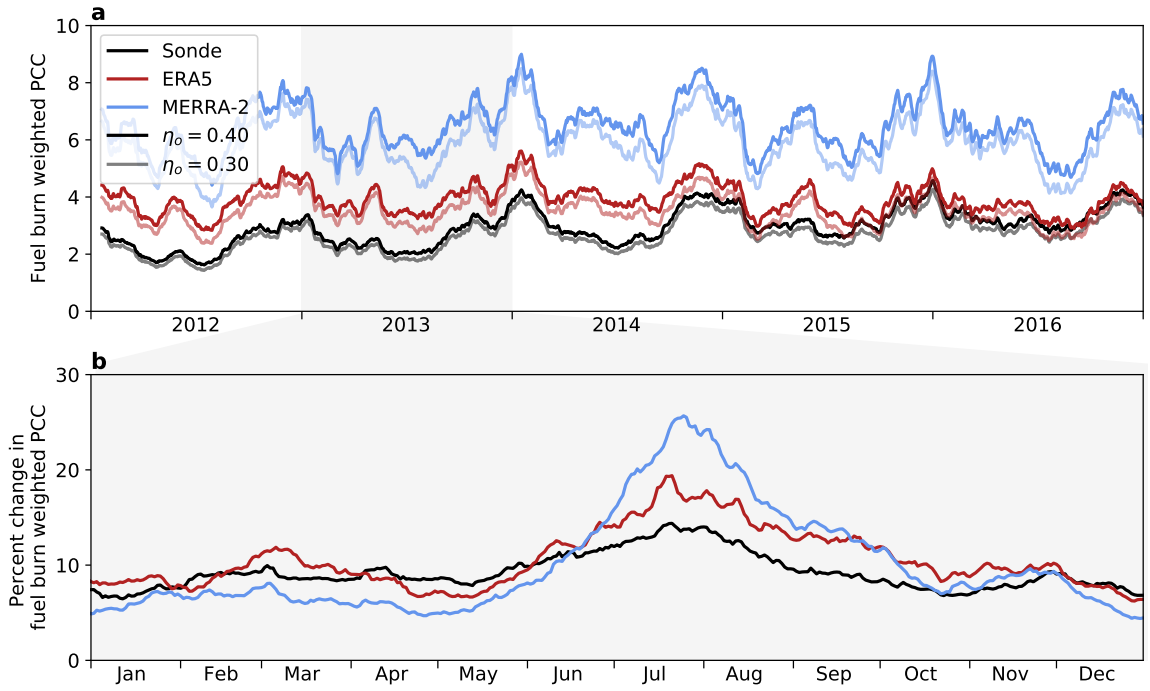

Figure 3-10: Effect of engine overall efficiency (η_o) on fuel burn weighted PCC. (a) Timeseries of fuel burn weighted PCC from 2012 to 2016 for $\eta_o = 0.30$ (light shades) and $\eta_o = 0.40$ (dark shades) for the sonde data (black), ERA5 (red) and MERRA-2 (blue). (b) Percent change in fuel burn weighted PCC for 2013 only for a change from $\eta_o = 0.30$ to $\eta_o = 0.40$ for each model.

displacement a newly formed ice crystal could fall before evaporating, so is related to the contrail lifetime, depending also on the settling velocity of the crystals.

Figure 3-12 shows how the mean evaporation depth for regions satisfying the PCC at 10 km varies from 2012 to 2016. The sonde data shows a mean depth of 1.3 km, varying between a minimum of 1.0 km in NH summer and maximum of 1.8 km in NH winter. Comparing with reanalysis data, ERA5 has a NMB of 17% and a MAE of 0.2 km, which is smaller than for MERRA-2 (45% and 0.6 km, respectively). The contrail lifetime estimated using ERA5 is thus likely to be more accurate than when using MERRA-2, although an overestimate would be expected from both. Both models predict a similar, positive R^2 of 0.85, suggesting that seasonal variations are well represented. This suggests that the reanalysis models predict the vertical gradients in temperature and water vapor correctly.

Figure 3-13 shows a timeseries of the median and inter-quartile range (IQR) of

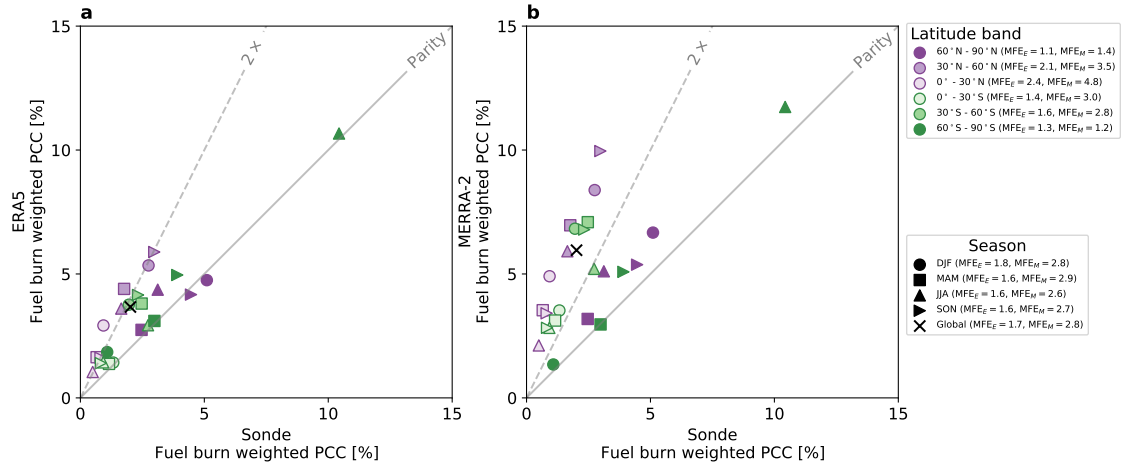

Figure 3-11: Parity plot of fuel-burn weighted PCC by latitude band and season. Results are separated by model: (a) ERA5 and (b) MERRA-2. Latitude bands are separated by color with purple representing the Northern Hemisphere and green the Southern Hemisphere. Darker colors represent higher latitudes. Seasons are represented by markers with DJF in circles, MAM in squares, JJA in upward-facing triangles and SON in rightward facing triangles. Global, annual average results are also included in the black cross. The mean factor error (MFE) between each reanalysis data and the sonde is included for results by latitude band and season. The subscript "E" refers to ERA5 and subscript "M" to MERRA-2.

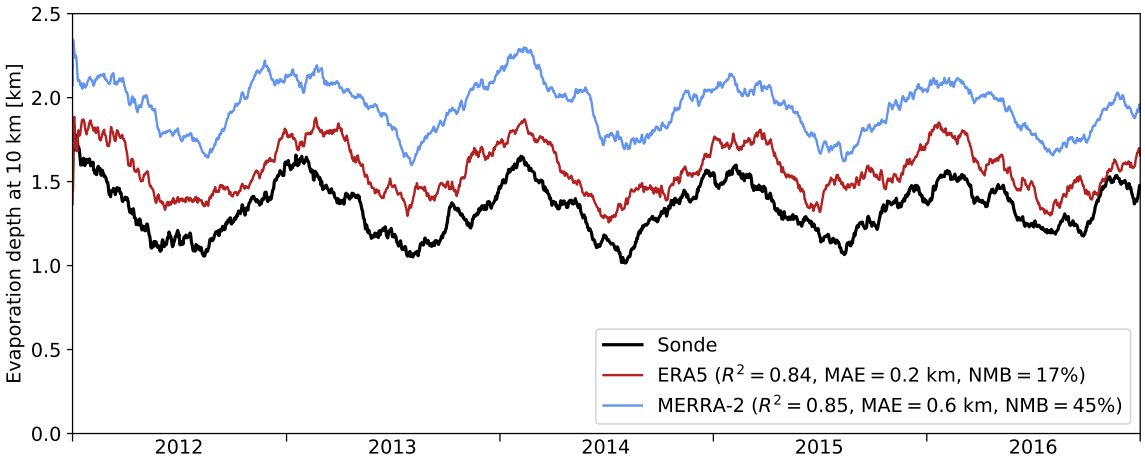

Figure 3-12: Timeseries of mean evaporation depth for PCC regions at 10 km. The black solid line represents the sonde data, red line ERA5 and blue line MERRA-2. The caption includes the metrics comparing each reanalysis data with sonde including the R2, mean absolute error (MAE) and normalized mean bias (NMB).

the evaporation depth for the sonde data and each data assimilation system. These results follow those discussed for the mean evaporation depth except for two differ-

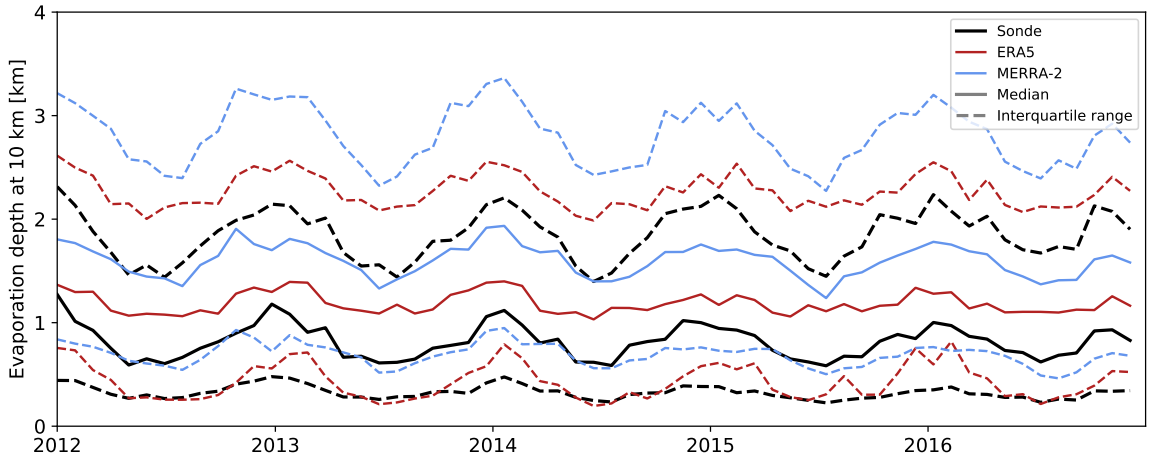

Figure 3-13: Median and interquartile range (IQR) of the evaporation depth at 10 km. Black lines represent sonde data, red lines ERA5 and blue lines MERRA-2. Solid lines refer to the median of the distribution and the dashed lines are the lower and upper quartile, together representing the interquartile range.

ences. Firstly, the distribution of evaporation depth is skewed by a small number of large evaporation depths, exceeding 5 km in 3.9% of cases. This causes the mean evaporation depth to be 0.5 km greater than the median. Secondly, both ERA5 and MERRA-2 do not capture the strength of the seasonal cycle in the median evaporation depth. The observations vary by a factor of 2.2 between a maximum of 1.3 km in JJA and minimum of 0.6 km in DJF. In comparison, ERA5 varies from 1.4 km in JJA to 1.0 km in DJF, a factor of 1.4 seasonality, and MERRA-2 varies from 1.9 km in JJA to 1.2 km in DJF, a factor of 1.6 seasonality.

3.3.4 Individual observations

Multiple contrail studies have shown that in-flight, operational strategies to divert flights around PCC or ISS regions may reduce the number of contrails that form [16, 120, 121]. These strategies rely upon forecasts being accurate enough to predict PCC regions. To assess this, I compare individual observations of PCC regions with estimates from the reanalysis data. ERA5 and MERRA-2 correctly predict PCC regions (true positives) 13% and 52% of the time respectively between 9 and 12 km globally. In comparison, non-PCC regions (true negatives) are correctly predicted

95% and 93% of the time, respectively (see Tables 3.1 and 3.2). The results are similar to recent comparisons between aircraft observations and ERA5, where ice supersaturation is found to be correctly predicted 18% of the time [122]. These results suggest that mitigation strategies using reanalysis data focusing on individual contrails may be unreliable.

Table 3.1: Error matrix for ERA5 against sonde data for observations globally at altitudes between 9 and 12 km.

		ERA5		
		Not PCC	PCC	
Sonde	Not PCC	90.2%	4.7%	95.0%
	PCC	4.4%	0.7%	5.0%
		94.6%	5.4%	100%

Table 3.2: Error matrix for MERRA-2 against sonde data for observations globally at altitudes between 9 and 12 km.

		MERRA-2		
		Not PCC	PCC	
Sonde	Not PCC	87.9%	7.1%	95.0%
	PCC	2.4%	2.6%	5.0%
		90.3%	9.7%	100%

I also assess whether the ability of reanalysis data to predict individual PCC regions is driven by errors in temperature or humidity by swapping either the temperature or humidity profiles in sonde data with that in the reanalysis data. Figure 3-14 shows the improvement on various metrics of swapping temperature or humidity for both ERA5 and MERRA-2 in the northern mid-latitudes, between 9 – 12 km. For both ERA5 and MERRA-2, swapping the temperature profile has a small effect, improving the number of true positives by 2 and 1 percentage points, respectively. In comparison, swapping the humidity profiles leads to a 54 and 28 %-pts improvement. This confirms that errors in humidity are driving the difference between the sonde and reanalysis estimates of percentage PCC [123]. The remaining difference may be due to the lower vertical resolution of the reanalysis compared with the sonde data.

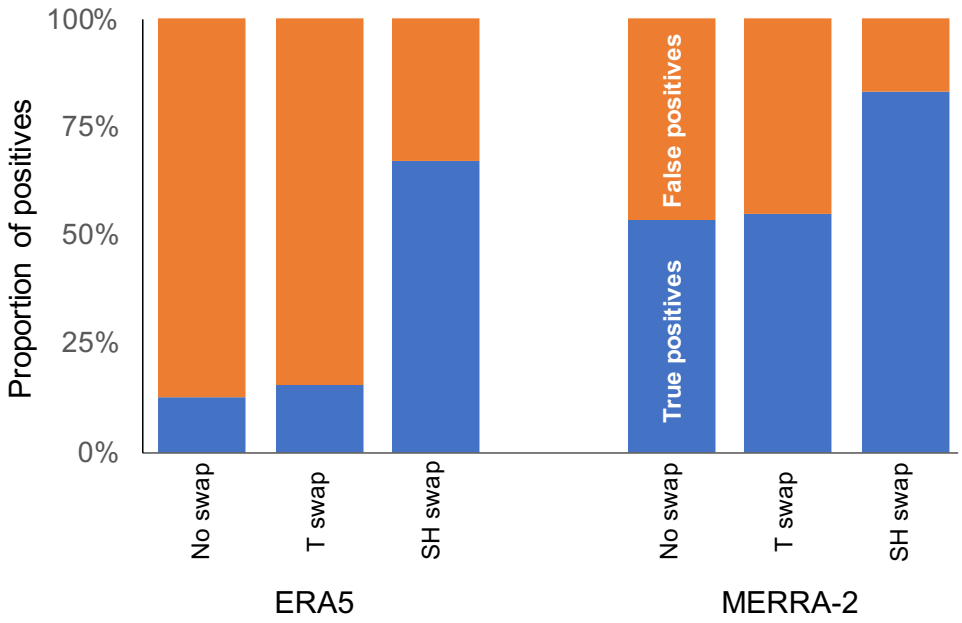

Figure 3-14: Proportion of individual observations satisfying the PCC in the reanalysis and sonde for ERA5 (left three bars) and MERRA-2 (right three bars). The left bar in each group compares the raw reanalysis data with the sonde data. The central bar uses the temperature (T) profile from the sonde data and the specific humidity (SH) profile from the reanalysis data, compared with the sonde data. The right bar uses the humidity profile from sonde data and the temperature profile from the reanalysis data, compared with the sonde data.

3.4 Discussion

I find four central results. Firstly, both ERA5 and MERRA-2 overestimate the fuel burn weighted PCC by 8% to 138% varying by model and latitude band. In the northern mid-latitudes, where 62% of aviation fuel is burned, the mean percentage PCC at cruise altitudes is overestimated by a factor of 2.0 and 3.5, respectively for ERA5 and MERRA-2. Similar biases are also found in the tropics and Arctic. These results suggest that contrail simulations using reanalysis data will overestimate the number of persitent contrails that form.

Secondly, the sonde data exhibits seasonality in PCC in the mid-latitudes, where the mean cruise percentage PCC is a factor of 1.7 higher in DJF than JJA. MERRA-2 consistently overestimates this mean cruise PCC by a factor of 3.4 – 3.6 and ERA5 by a factor of 2.0. Both models correctly predict the seasonality in PCC, which is

important to capture as studies suggest contrails forming in the winter are expected to have an outsized climate impact [117].

Thirdly, the evaporation depth, a proxy for contrail lifetime, is overestimated by 45% in MERRA-2 and 17% in ERA5. This suggests that simulations using MERRA-2 and ERA5 would predict contrails surviving to lower depths than expected from observations and, thus, with longer lifetimes.

Finally, both reanalyses are unable to identify individual PCC regions. At cruise altitudes, MERRA-2 correctly predicts PCC regions 52% of the time, while ERA5 correctly predicts 13% of these. This suggests that mitigation strategies focusing on avoiding individual contrails may not be practical given the inability of reanalysis data and, by extension, forecasts in predicting individual PCC regions. Sensitivity tests show that model improvements should focus on estimating humidity more accurately to improve individual PCC estimates.

These findings come with some caveats. First, the relative measurement uncertainty of the RS92 humidity sensor is 10% [103], however, our findings show biases in the reanalysis data that are higher than this. The RS92 sensor also has a daytime dry relative bias due to radiative heating that is 30% at 10 km and 50% at 15 km [98, 103, 104, 124]. This dry bias can explain some differences between sonde and reanalysis data. To test the robustness of our findings, I compared 2,877 profiles from the Global Climate Observing System (GCOS) Reference Upper Air Network (GRUAN), which corrects raw RS92 measurements for time lag and radiation bias. Figure 3-15 shows that the GRUAN data predicts a 4.2% occurrence of PCC regions between 9 – 12 km. The IGRA data underestimates the occurrence of PCC regions by 24% relative to GRUAN, while MERRA-2 and ERA5 show a factor of 2.5 and 1.6 overestimate, respectively. For comparison, the 95% confidence interval in the mean occurrence of PCC regions at cruise altitudes in the GRUAN data is 3.7% - 4.6%. This bias also cannot explain spatial and temporal differences between the sources. In addition, the comparison between the sonde and reanalysis data are based on the grid average. I do not interpolate the reanalysis data in either time or space. As a result, PCC regions smaller than an individual layer will not be resolved, but this is

not expected to have an effect on the ability to resolve deeper PCC regions.

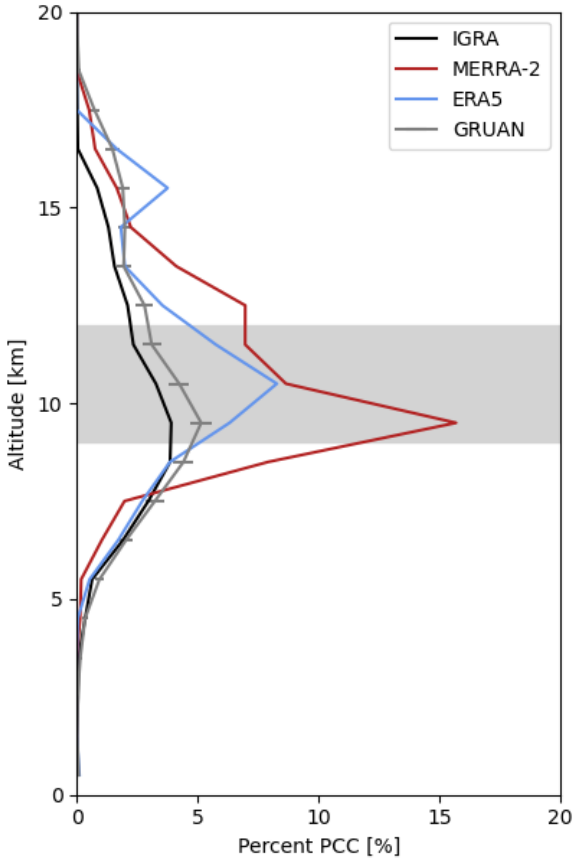

Figure 3-15: Percentage of profiles that satisfy the PCC for four different sources at 2,877 collocated location. Sondes observations are shown in the black, solid lines, MERRA-2 in the red, solid lines, ERA5 in the blue, solid lines, and GRUAN in the grey, solid lines. Error bars represent the 95% confidence interval of percentage PCC estimated in each layer. Further details on the calculation are provided in the Methods. The grey shaded region represents the range of aircraft cruise altitudes (9 – 12 km).

Reanalysis data are a necessary tool in contrail modeling and other applications. Our results show biases in the predicted number of persistent contrails that could form using reanalysis data. The biases have shown that ERA5 and MERRA-2 both overestimate the likelihood of persistent contrail formation at cruise altitudes on average by a factor of 1.9 and 3.5, respectively in the mid-latitudes. Furthermore, both models fail to capture variations in the likelihood and expected lifetime of contrails with season, altitude, and latitude, which cannot be accounted for with a single scalar correction. Meteorological data that prioritizes upper tropospheric and lower strato-

spheric humidity, coupled with direct observational estimates of contrail coverage and properties are needed to improve and better constrain current model estimates.

Chapter 4

Inference of global contrail properties

4.1 Introduction

Global, numerical models of contrails make a range of assumptions about how contrails evolve over time. Two broad approaches have been developed. First, contrail modules have been developed within global climate models (GCMs). These modules are similar to those for natural cirrus clouds, but the formation of contrails is based on the Schmidt-Appleman Criterion (SAC) (see Chapter 3) [6–8]. Second, Lagrangian contrail models have been developed that track the evolution of the contrail cross-section, explicitly modeling the ice mass and number of particles. A "Gaussian plume approach" - where the concentration of contrail ice particles are assumed to follow a Gaussian distribution - has been widely used in this role due to its computational speed and adaptability for use in diffusion and shear-driven flows [17, 23, 125]. This approach has been used to quantify the annual average, global, net instantaneous radiative forcing (RF) of contrails in 2006 to be 74 mW/m^2.

These global modeling approaches require simplifications to be made. For example, all present implementations of a Gaussian plume model for contrails assume that the ambient conditions are homogeneous and that the contrail ice crystals are monodisperse in size - i.e. all particles have the same diameter. Jacobson et al. [126]

are able to account for the crystal size distribution, however use the subgrid plume model [127] to simulate the evolution of contrail dimensions (width and depth). This approach is similar to the Gaussian plume in that ambient conditions are assumed to be homogeneous throughout the contrail cross-section. Large eddy simulations (LES) have shown that the effective size of contrail ice particles can vary by an order of magnitude within the contrail, with the largest particles settling faster than the smaller particles (see, for example, Paoli and Shariff [32] and Unterstrasser and Gierens [33]). This can lead to contrails that are deeper than those modeled using the Gaussian plume approach, with the largest particles reaching warmer conditions where they evaporate earlier than the smallest particles. The effect of accounting for these factors on the global contrail RF has not been quantified.

In this chapter, I use statistical inference to estimate the global contrail RF using a medium-fidelity contrail model. Statistical inference is commonly used in situations where measuring or modeling a full population is difficult, such as opinion surveys [128], or modeling uncertain distributions that can take infinitely many values [129]. For a full flight schedule with around 35 million operations, I randomly sample from the distance flown by the full population of flights. Contrail properties are estimated using the Aircraft Plume Chemistry, Emissions, and Microphysics Model (APCEMM), a model that can simulate the evolution of a contrail, capturing the crystal size distribution and spatial variations over time [36]. Meteorological conditions and aviation emissions, required as inputs to APCEMM, are estimated from MERRA-2 and the Aviation Emissions Inventory Code (AEIC), respectively [78]. Next, the rapid radiative transfer model (RRTM) [37] is used to quantify contrail radiative properties. Finally, contrail properties of the full population of flights, such as the RF, can then be inferred from the sample set [130], providing a new, higher fidelity estimate of global contrail properties and climate impacts.

4.2 Method

In this section, the modeling and inference approach is described in more detail. It begins with an overview of the sampling and modeling approach, before describing each model in more detail, focusing on changes and applications for this work.

4.2.1 Sampling approach and modeling overview

Starting with a flight schedule for scheduled commercial aviation in 2016 generated by the Official Airline Guide (OAG) [131], AEIC is used to model the flight paths for each operation using the great circle distance between the origin and destination airport. In 2016, the total distance flown by commercial aircraft was estimated to be 4.5×10^{13} m. To select a sample, a uniformly-distributed random real number is drawn between 0 and the total distance flown. Using the order defined in the schedule (by date-time, then origin-destination pair, and then aircraft type), and the distance flown per operation calculated from AEIC, the exact operation and distance along that operation can be found for each sample. For example, if the sample drawn is 500 km, I find the flight within the order of the schedule that would have flown the 500^{th} km. Selecting from the distance flown means that any global estimate using the samples requires multiplying the desired mean property across all samples by the total distance flown (i.e. 4.5×10^{13} m). The time, location (altitude, latitude, and longitude), and emissions are calculated using AEIC. For this work, I generate 100,000 random samples from which to extract operating conditions from AEIC and calculate contrail properties in APCEMM.

To test whether this sampling approach is adequate, Figure 4-1 shows the estimated fuel burn per unit distance flown against the number of samples. The left panel shows the estimated sample mean and 95% confidence interval, as well as the actual fuel burn per unit distance calculated by AEIC for the full schedule. This shows that, for this particular variable, the sample mean converges towards a constant value, which is within 0.06% of the AEIC calculated value after 100,000 samples. The rate of convergence is dependent on the population standard deviation, where a

higher standard deviation would lead to a wider confidence interval after modeling all samples. The convergence properties can also be measured by the coefficient of variation (CoV), which equals the sample standard deviation over the sample mean. If the random samples are independent and identically distributed, then the Central Limit Theorem (CLT) implies that the gradient of the CoV with the number of samples should be $-1/2$ in log-log scale. This is shown in the right panel of Figure 4-1, where the CoV reaches 1% after approximately 3,400 samples.

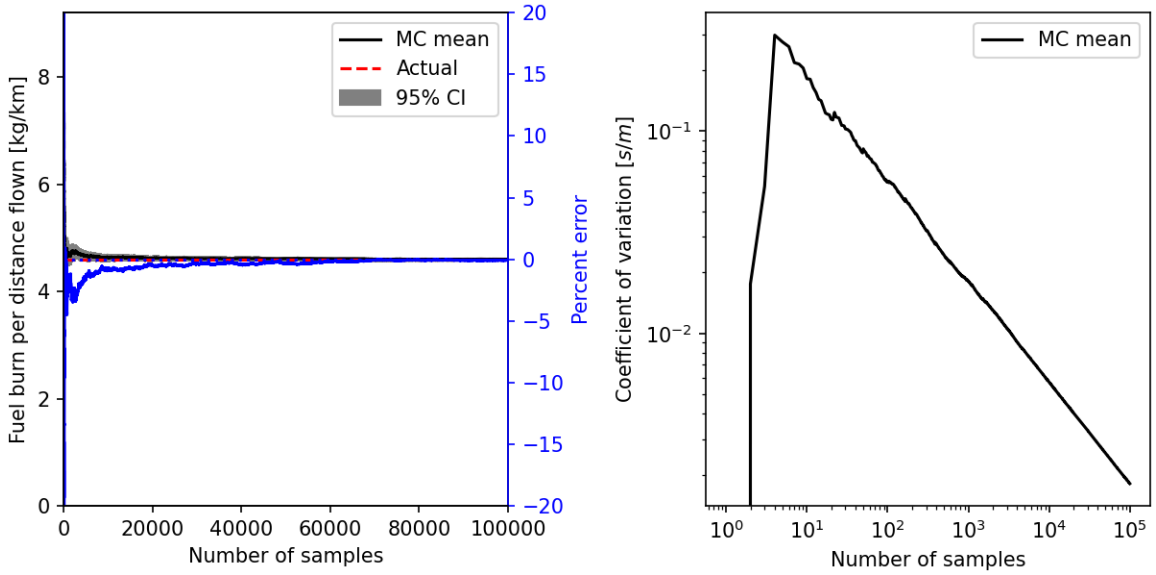

Figure 4-1: Convergence of the fuel burn per unit distance flown against the number of samples. The left panel shows the convergence of the Monte Carlo (MC) mean (black solid line), the 95% confidence interval (CI) of the mean (grey shaded region), and the actual fuel burn per unit distance calculated by AEIC (red dashed line). The percentage error is shown by the blue line with the right hand side axis of the left panel. The right panel shows the coefficient of variation (standard deviation over the mean) of the samples.

In addition to the fuel burn, the aircraft type is also an important variable in modeling contrails. The size and weight of the aircraft influences the wing-tip vortices that drive the engine exhaust plume and contrail downwards over the first few minutes after emissions [32, 132]. In addition, the aircraft engine operation affects the exhaust temperature and particle emissions, which can change whether the exhaust plume satisfies the SAC and the number of particles that form [8]. For this reason, I also test the bias in proportion of the total distance flown by each aircraft type, which

is shown in Figure 4-2. This shows the actual proportion of distance flown by each aircraft type against that estimated from the samples. At proportions above 10^{-3}, the sampling approach has an error below 10% of the actual proportion flown.

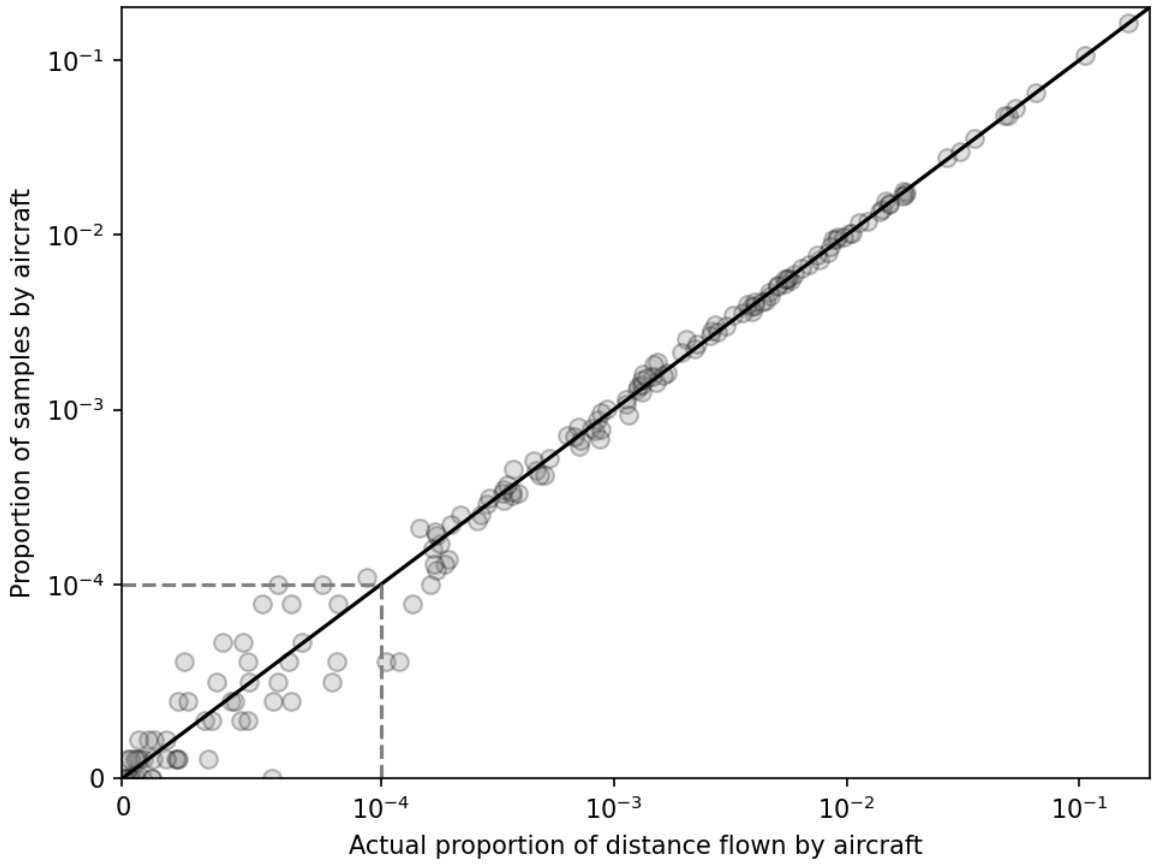

Figure 4-2: Actual proportion of distance flown by each aircraft type versus that estimated by the samples. The axes are logarithmic above 10^{-4} and linear below.

The colocated vertical meteorological profile is extracted from the MERRA-2 reanalysis output. Temperature and humidity profiles are extracted and used as inputs to APCEMM for modeling the evolution of the contrail. The radiative forcing of the contrail is estimated using RRTM with the Monte Carlo Independent Column Approximation (McICA). Natural cloud properties are also extracted from MERRA-2 and the maximum-random overlap approach is used between natural clouds [133]. Contrail properties are input separately from natural cloud properties and random overlap is assumed between natural clouds and contrails. Further details on the RRTM changes and modeling approach are provided in Section 4.2.5.

These steps are repeated over all samples that are selected from the schedule. In the subsequent sections, each model is described in more detail, with a focus on the changes made specifically for this work.

4.2.2 Emissions and exhaust conditions

The Aviation Emissions Inventory Code (AEIC) was developed by Simone, Stettler, and Barrett [78] and, starting from a flight schedule, can estimate global civil aviation routes and emissions. AEIC uses the EUROCONTROL Base of Aircraft Data (BADA) version 3.15 to model the performance of aircraft operations throughout their flight envelopes [112]. Emissions species, including NO_x, unburned hydrocarbons, and sulfur emissions, can also be estimated. For modeling contrails, the number of particles being emitted is required as this is required to estimate the number of contrail ice particles. I use the SCOPE11 method developed in Chapter 2 to estimate the total number of particles and the distribution's geometric mean diameter (GMD), used to calculate the rate of ice sedimentation on ice crystals via the Kelvin effect [134].

To model the formation of contrails, APCEMM uses a 1-D plume model that simulates the mixing between the mixed-out engine core and bypass conditions with the ambient air [135, 136]. This allows for modeling the plume mixing process explicitly and accounts for the sulfate coating of black carbon particles that are assumed to be the contrail ice nuclei [9, 11, 13]. Using this model requires an estimate of the exhaust temperature and nozzle area. The mixed-out stagnation temperature is used since the core and bypass nozzles are expected to mix faster than the bypass and exhaust due to the larger velocity difference between the core and nozzle flows. This approach is consistent with existing contrail models [8]. The exhaust temperature and nozzle area are estimated in two steps, using gas turbine thermodynamic cycle analysis [137]. An overview of the methods is provided below, with more details in Appendix B.

First, I estimate the exhaust area. To do this, the thrust, overall pressure ratio, bypass ratio, and fuel flow rate at the 100% thrust condition from the ICAO EDB

[75] is used. The bypass to jet velocity ratio, α, is assume to be fixed at 0.7 at this thrust condition. α can vary between engines and across operating points, however a value of 0.7 is a typical design variable used when developing an engine (Dr. Jayant Sabnis, personal communication, October 16, 2020). Assuming efficiencies for the fan, compressor, and turbine (again, personal communications with Dr. Jayant Sabnis), the exhaust area can be calculated.

Second, I estimate the engine conditions at cruise. First, fuel flow rates at the four operating points at ground, sea-level static data from the ICAO EDB are used [75] to develop a linear relationship between the non-dimensional fuel flow rate and the fraction of rated gross thrust for each engine. The non-dimensional fuel flow rate, $\hat{m}_f$, is calculated as

$$\hat{m}_f = \frac{\dot{m}_f \text{LCV}}{\sqrt{c_{p,c} T_{t2}} A^2 P_{t2}} \tag{4.1}$$

where $\dot{m}_f$ is the fuel flow rate in kg/s, LCV = 43.1 MJ/kg is the lower calorific value of the fuel, $c_{p,c} = 1,005$ J/kg/K is the specific heat capacity of air at constant pressure, T_{t2} and P_{t2} are the stagnation temperature and pressure, respectively, at the inlet to the engine, and A is the exhaust area of the engine.

Since both the non-dimensional fuel flow rate and the fraction of rated gross thrust are both non-dimensional properties of the engine, they can be used to relate fuel flow conditions at cruise to the fraction of rated gross thrust generated by the engine [137]. In cruise, the non-dimensional fuel flow rate is computed from Eq using the fuel flow rate estimated in AEIC. The fraction of rated thrust is then found by interpolating the ground data relating non-dimensional fuel flow rate and the fraction of rated thrust. This provides an estimated fraction of rated gross thrust that represents the operation of an engine in AEIC, which is used to estimate the gross thrust, overall pressure ratio, and the fuel flow rate at cruise. This is used to estimate the temperature and pressure throughout the engine and, using the exhaust area calculated in the first step, the exhaust plume stagnation temperature is found.

4.2.3 MERRA-2

For this work, I use the MERRA-2 reanalysis product from the Global Modeling and Assimilation Office (GMAO) [27]. MERRA-2 uses a cube-sphere horizontal discretization with a resolution of 50 km and 72 hybrid-eta levels from surface to 0.1 hPa. For this study, the 2016 3-hourly, $0.5° \times 0.625°$, 72-layer data was used. As described in Section 4.2.1, humidity, temperature, and wind speeds are used. The ambient humidity profile is assumed to be stationary in time since the contrail and water vapor will advect together. Temperature and wind speed can be changed by external factors (e.g.; radiation and/or pressure changes). For this reason, I account for temporal changes in the temperature and wind speed, extracting the profile from each variable from MERRA-2 as a function of time after formation, to be consistent with MERRA-2. Wind speeds are interpolated vertically and used to advect crystals relative to the aircraft flight altitude, and thus represent the effect of shear. For the temperature and humidity, a nearest neighbor approach is used for the vertical distribution, while temporal variables are interpolated linearly in time. Cloud fraction, liquid water path, and ice water path are also extracted from MERRA-2 every three hours and used for the radiative forcing calculations.

4.2.4 APCEMM

The Aircraft Plume Chemistry, Emissions, and Microphysics Model (APCEMM) was developed by Fritz et al. [36] and is able to simulate the evolution of the gaseous, aerosol, and ice microphysical properties of an aircraft plume. It was developed to model plume evolution under a variety of conditions, as well as to study interactions between contrail ice and plume chemistry. In this work, only the emissions and ice microphysics components of APCEMM are used. The model simulates the early plume using a box model which is used to whether the contrail forms and indicate the number of sulfate-coated soot particles that lead to ice crystals [135, 136]. Diffusion, advection (including settling), and shear are then used to model the bulk of the contrail using a spatially-resolved, 2-D spectral method [138], and particle growth using

a moving-center size structure [139]. The simulation constants (e.g.; diffusivities) are retained from Fritz et al. [36] except for the soot emissions index and geometric mean diameter, fuel flow rate, aircraft mass, wingspan, number of engines, flight speed, exhaust temperature, exhaust bypass area, and flight altitude generated from AEIC and the turbofan solver described in Section 4.2.2. The spatial resolution is set to approximately 100 m in the horizontal direction and 10 m in the vertical direction, and the time step set to 600 s. The ice particles are modeled using 38 size bins from a minimum radius of 50 nm to a maximum of 80 µm

For all simulations, contrails are assumed to persist for a maximum of 24 hours within APCEMM given the low likelihood of contrails surviving beyond this duration [16, 111]. Contrails are also assumed to have evaporated when both the ice mass and number of crystals are below 10^{-2} kg/m and 10^{6} crystals/m, respectively. In addition, contrails are only modeled to an height of 4 km below the flight altitude. In a subset of cases where a large proportion of contrail ice particles grow beyond approximately 50 µm, particles can fall more than 10 vertical grid cells in a given timesteps, leading to gaps in the vertical spacing of contrail ice mass. These cases are re-simulated at the same spatial resolution but with a time step of 120 s.

Three changes are made to APCEMM for this work. First, as APCEMM uses a spectral solver for diffusion and shear, periodic boundary conditions are required. MERRA-2 profiles are not periodic and thus I separate APCEMM's humidity profile into a meteorological or "met" portion and a "plume" portion. The met portion is equivalent to the input profile from MERRA-2 and is fixed with time. The plume portion represents the change in the background meteorological conditions due to the presence of ice crystals. Given that the background humidity is assumed to be stationary, the plume portion is the only component that needs to be diffused, advected, and sheared. Ensuring that the domain is large enough to contain the contrails, the plume component is zero at the domain edges and thus periodic.

Second, a low-pass filter is applied to the shear and advection components of the spectral solver [140]. This alleviates stability issues in the form of Gibbs oscillations that were found during the formation and evaporation stages of contrail evolution

[140]. The low-pass filter acts similar to approaches using artificial dissipation, alleviating the instability issues. The added stability allows me to simulate at lower temporal resolutions than Fritz et al. [36].

Finally, APCEMM is updated to read humidity, temperature, and shear data from MERRA-2. As mentioned in Section 4.2.3, I use a nearest neighbor approach for filling variables vertically and linearly interpolate temperature and velocity in time.

4.2.5 RRTM

The rapid radiative transfer model (RRTM) is a widely used model for estimating radiative fluxes in the atmosphere [37, 141]. For this work, the standalone version of RRTM is used. The vertical pressure, temperature, and humidity profiles from MERRA-2 are used directly with RRTM, with built-in values for 5 chemical species (CO_2, O_3, N_2O, CO, CH_4, and O_2) used based on the global, annual average. Surface properties (temperature and surface emissivity) and natural cloud properties (cloud fraction, liquid water path, and ice water path) are also extracted from MERRA-2. The cloud properties are used with the Monte Carlo Independent Column Approximation (McICA) with the maximum-random overlap assumption to allow for partially cloudy layers [133, 142, 143]. The liquid water cloud effective radius is assumed to be 14.2 µm and ice water cloud effective radius to be 24.8 µm.

The McICA estimates radiative transfer by simulating multiple, randomly generated columns (also referred to as subcolumns), where each layer is homogeneously cloudy or clear. The proportion of subcolumns that are cloudy for a given layer matches the cloud fraction assuming a sufficient sample size. For a layer in a subcolumn, the liquid and ice cloud properties are calculated separately, but then combined together for use in forcing calculations. For example, for layers with non-zero cloud fraction, the cloud optical depth, τ_c is calculated as

$$\tau_c = \mathrm{IWP}\sigma_{\mathrm{ice}} + \mathrm{LWP}\sigma_{\mathrm{liq}} \tag{4.2}$$

where IWP stands for the ice water path and LWP the liquid water path, both in g/m^2; σ represents the absorption coefficient; and subscripts ice and liq represent the ice and liquid portions, respectively. This combination and the fact that a layer is considered either homogeneously cloudy or clear allows me to incorporate an additional calculation for contrails as

$$\tau_c = \mathrm{IWP}\sigma_{\mathrm{ice}} + \mathrm{LWP}\sigma_{\mathrm{liq}} + \mathrm{CWP}\sigma_{\mathrm{con}} \tag{4.3}$$

where CWP stands for the contrail water path in g/m^2 and subscript con is short for contrail. For layers with no clouds, the cloud fraction is always zero, so only the contrail portion of the cloud calculations is included. For cloudy conditions, all three (ice, liquid, and contrail) portions are included. In this case, maximum-random overlap approach is used for natural clouds [142], and random overlap is used for the overlap between natural clouds and contrails.

In order to use this implementation, the contrail ice water path and effective radius (to estimate the absorption coefficient, asymmetry parameter, and single scattering albedo) are required as inputs to RRTM. The contrail properties from APCEMM are separated into layers matching the edges of the MERRA-2 layers. Additional layers are included for the lower and upper extremes of the contrail, matching the 1$^{\mathrm{st}}$ and 99$^{\mathrm{th}}$ percentile of the ice mass or crystal number, whichever is at a lower or higher altitude, respectively. Horizontally, the ice mass and number of crystals of eight APCEMM columns are combined together to form a single column in RRTM as shown in Figure 4-3. Calculations are conducted separately for each RRTM column using the independent column approximation (ICA), which assumes that columns do not interact with each other radiatively [33, 144]. In each RRTM column, the contrail water path is calculated by integrating the ice water concentration vertically. The average effective radius is estimated by weighting the effective radius in each APCEMM grid cell by the ice crystal surface area. The radiative forcing is estimated at the thermal tropopause (provided by MERRA-2) and the total forcing of the contrail at a given time is calculated by integrating across each RRTM column.

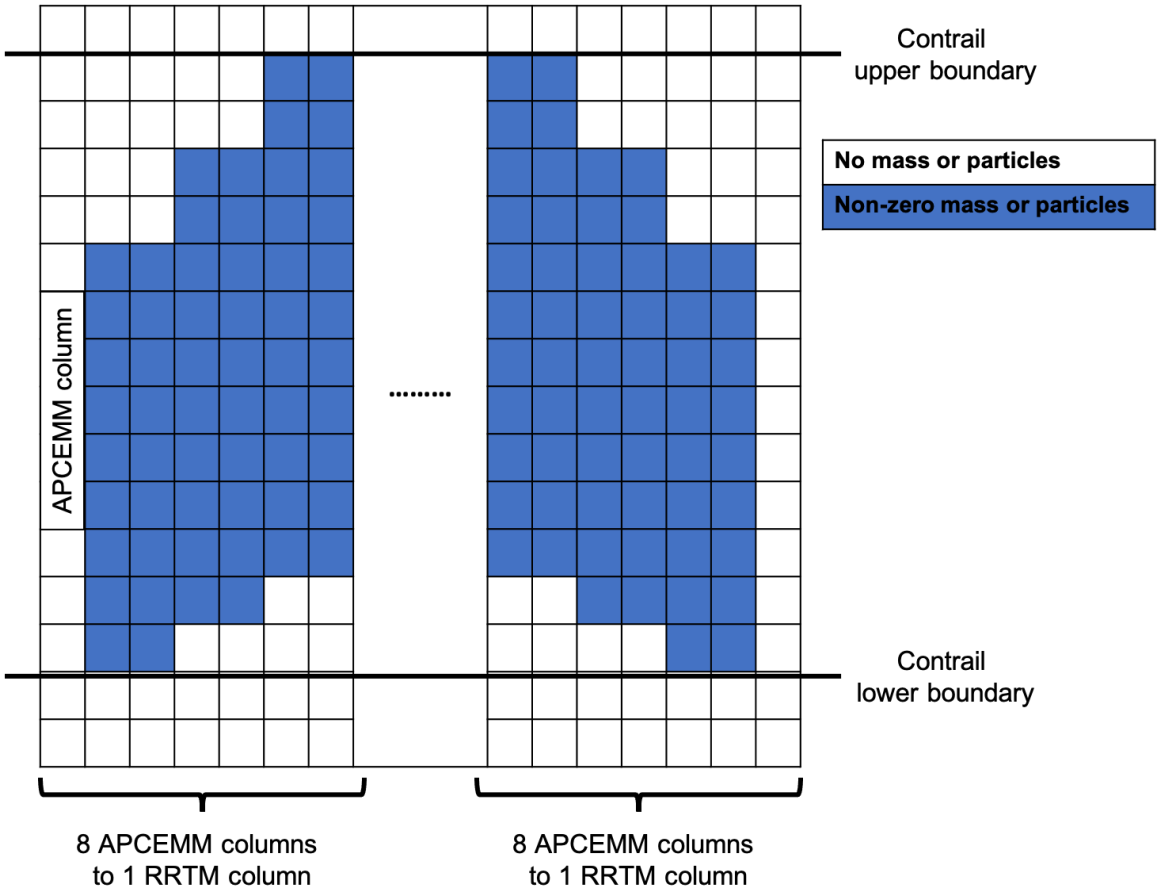

Figure 4-3: Vertical column and horizontal row mapping from APCEMM to RRTM. Blue shaded regions indicate a non-zero ice mass or number of crystals. 8 vertical APCEMM columns are combined for use in RRTM.

4.2.6 Inferring contrail properties

94,393 random samples are generated from the 2016 flight schedule, which requires modeling contrails for around 5,964 samples based on the persistent contrail criterion (see Chapter 3). 39% of these cases do not survive the vortex sinking process. (In Section 4.3.1, I will show that this is sufficient to estimate the annual average, global, net RF to within ± 7 mW/m^2). To estimate annual average contrail properties (e.g.; contrail radiative forcing), two calculation steps are required. First, the desired contrail property must be integrated in time until the contrail evaporates. For a single contrail, this is calculated as

$$F_{I,i} = \int_0^{t_{\text{evap}}} F_i(t)dt \approx \sum_{l=0}^{t_{\text{evap}}/\Delta t} F_i(t = t_l)\Delta t \tag{4.4}$$

where $F_{I,i}$ is the time-integrated property of the i^{th} contrail, t_{evap} is the time the contrail persists before evaporating, $F_i(t)$ is the contrail property at time t, and Δt is the simulation time step. Second, the average value of $F_{I,i}$ is calculated over all flight samples (including cases where no contrail forms) and multiplied by the average value with the total distance flown in the schedule, D_f, as

$$\hat{F} = \frac{D_f}{N} \sum_{i=1}^{N} F_{I,i} \tag{4.5}$$

where $\hat{F}$ is the annual average property of interest and N is the number of samples.

For all metrics, confidence intervals can also be calculated following similar principles to confidence intervals in Monte Carlo simulations. For a sufficiently large number of samples, the Central Limit Theorem finds that the distribution of the mean of a random variable, X, will be normally distributed with mean, $\mu = \sum_{i=0}^{N} X_i$, and standard deviation, $s = \sqrt{\frac{\sum_{i=0}^{N}\left(X_i - \hat{X}\right)^2}{N-1}}$. A confidence interval of $\alpha\%$ defines the interval within which I have $\alpha\%$ confidence that the actual mean lies. Throughout the results of this chapter, $\alpha = 95\%$ is used. This allows me to calculate confidence intervals that have a 95% likelihood of containing the population mean. This confidence interval does not measure the uncertainty due to uncertain inputs, but instead represents the uncertainty due to the use of a sampling-based approach instead of modeling all contrails possible in the schedule.

4.2.7 MERRA-2 correction for overestimate in persistent contrail formation

In chapter 3, MERRA-2 was found to overestimate the number of persistent contrails that form by a factor of 1.8 to 3.6 dependent on the altitude, latitude and season. To quantify the effect of this overestimate on the annual average, global contrail RF, contrails that have been simulated are randomly selected such that the proportion

of contrails that form is lower by the desired factor for each altitude, latitude, and season. This is accomplished by generating a uniformly-distributed random number between 0 and 1 for each modeled contrail, and assuming a contrail would actually form and persist if the random number is above one over the factor overestimate. For example, if the factor overestimate is 2.0 for a particle location, then a contrail would be considered to form and persist if the random number is above 0.5. For this work, I repeat the selection process 10,000 times in order to generate a distribution representing the effect of the correction on the global, annual average, radiative forcing. Note that this approach is a simplified approach to quantify the effect of the bias in MERRA-2 data and only provides an order of magnitude effect on the contrail RF.

4.3 Results

4.3.1 Annual average properties

The climate impact of many forcers, including contrails, is often measured via radiative forcing (RF). This measures the energy imbalance caused by the presence of a climate forcer due to its interaction with incoming and outgoing radiation. In this chapter, I calculate the instantaneous RF at the thermal tropopause. Additional RF metrics such as the effective RF provide a closer metric to estimate global temperature effects. However, these require simulations using a global climate model [1, 5].

The RF for contrails in 2016 is estimated to be 96 ± 7 mW/m^2. The effect of contrails on the shortwave (SW) and longwave (LW) components of the radiation spectrum are found to be 132 ± 8 mW/m^2 and -37 ± 3 mW/m^2, respectively. Figure 4-4 shows the running mean and 95% confidence intervals against the number of samples for each RF component. The LW RF converges the slowest requiring approximately 45,000 samples before reaching within 1% of its value using all samples, while the SW component requires around 10,000 samples. The combined, net RF results require approximately 20,000 samples to reach 1% of the value using all samples.

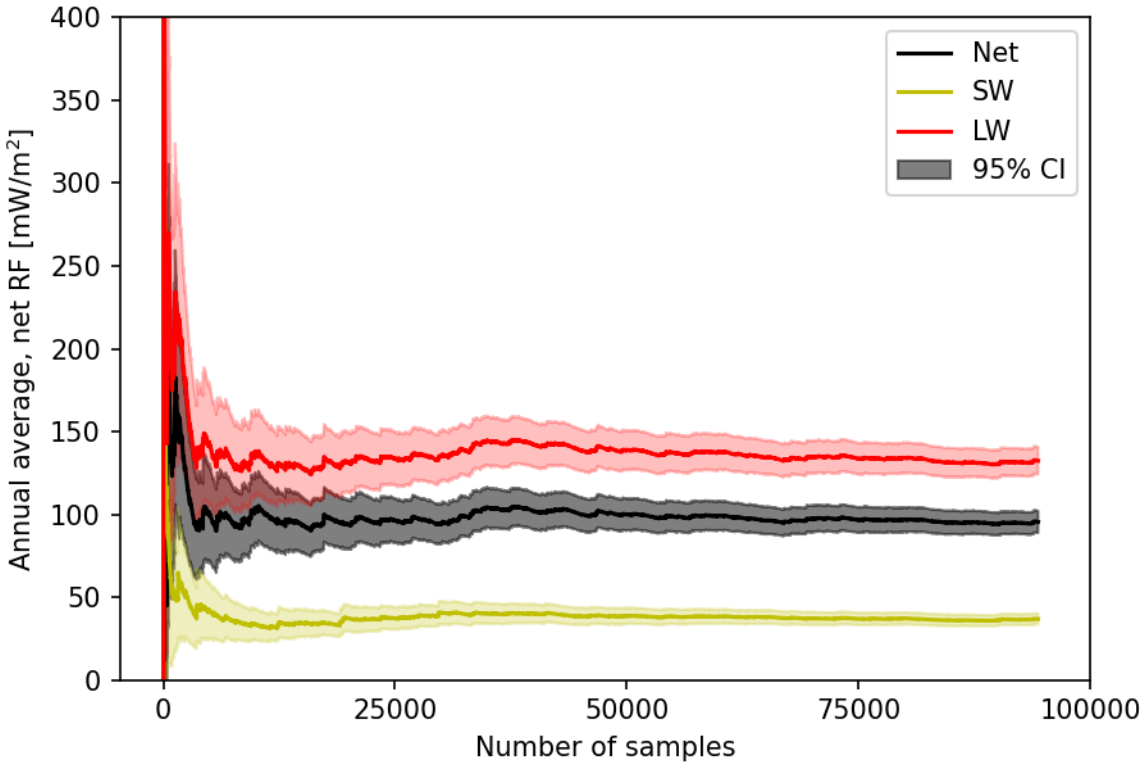

Figure 4-4: Running mean of net, shortwave, and longwave RF components with 95% confidence intervals.

Figure 4-5 shows the annual average, global, net RF estimates from seven different studies in addition to my result. The RF values are estimated for the year 2002 in one study and 2006 in 5 studies. To compare with this work, contrail RF estimates are scaled to the year 2016 based on the distance flown following the approach in Lee et al. [5]. The highest net RF is estimated in Lee et al. [5], who conducted a review of multiple contrail studies and provided a central estimate of contrail RF that is 3% higher than my estimate. This estimate is higher than all other published results included in Figure 4-5 as Lee et al. [5] correct for differences in aircraft routing and emissions models, and the use of bulk radiative transfer models versus more detailed line-by-line radiative transfer models. This difference is within the 95% confidence intervals and thus there is no statistical evidence to suggest that these estimates differ.

Schumann et al. [111] and Schumann and Graf [145] used an instance-based model similar to this work but assumed individual contrails to evolve as a monodisperse Gaussian plume [23]. I find their results to be within 6% higher and 28% lower of

this work, respectively, the former result being within the 95% confidence intervals of this work. Both studies, however, used the ERA5 reanalysis dataset, which was found to have a smaller wet bias than the MERRA-2 dataset used in this analysis. In chapter 3, ERA5 was also found to overestimate the probability of a persistent contrail forming by a factor of 2.0 in the northern mid-latitudes, versus a factor of 3.5 for MERRA-2. This suggests that the Gaussian plume approach overestimates the contrail ice mass and thus radiative properties of contrails relative to APCEMM. However, further studies on individual cases must be studied to confirm this.

The remaining estimates, shaded in green, simulate contrails within a global climate model and calculate the stratospherically-adjusted RF. This RF estimate has been found to be around 58% lower than the instantaneous RF for contrails [5]. This leads the net RF to be lower in these published estimates than this work for the results highlighted in green. Additional differences can be attributed to differences in models and assumptions used to model contrails. The estimated net RF in Chen and Gettelman [26] was significantly lower than other published results as they used an initial crystal size of 10 µm, which may be a factor of 2 or higher than expected from measurement data [145]. A sensitivity study in Chen and Gettelman [26] found that reducing the initial crystals size to 7.5 µm increases the net RF by a factor of 2.5, which would bring the difference with this work to 53%. Overall, the contrail inference approach using APCEMM generates a net RF that is in line with published results.

4.3.2 Spatial distribution of contrail impacts

Figure 4-6 shows the spatial distribution of the contrail energy forcing (EF) per distance flown in 11 regions in the Northern hemisphere and the associated 95% confidence interval over means in each region. The EF is calculated as the time integral of the radiative forcing multiplied by the contrail width [146]. For this work, instead of using estimate a contrail width, I calculate the RF in groups of eight vertical APCEMM columns (see Section 4.2.5), multiply each RF by the width of the group of columns, and then sum across all groups. The contrail width is thus the sum of the

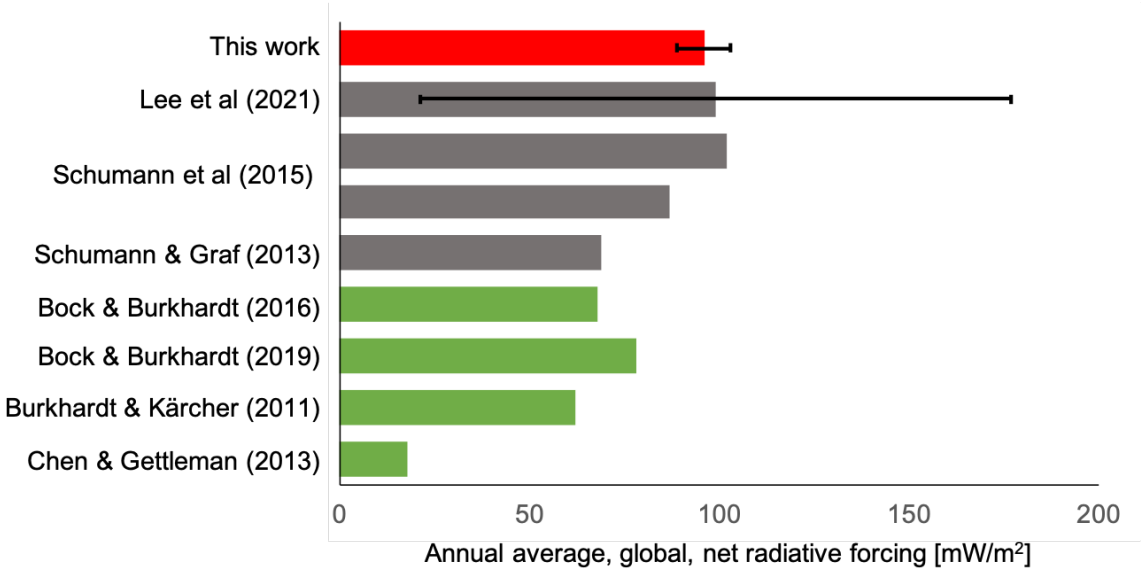

Figure 4-5: Comparison of annual average, global, net radiative forcing estimates from literature with this work (red bar). Grey bars represent instantaneous RF estimates and green bars stratospheric-adjusted RF. The two results for Schumann et al. [111] are with (higher value) and without (lower value) coupling with a global aerosol-climate model.

width of all groups with non-zero forcing. The highest contrail EF per distance flown occurs in W. EU with a forcing of 71 MJ/m. This is 23% higher than the contrails from flights over Russia and 35% higher than those over Canada/Alaska, the next two highest forcing values. In the other regions of heavy air traffic, CONUS and SEA, the contrail EF is 39% and 69% lower than in W. EU, respectively. The lower panel of Figure 4-6 shows that the highest proportion of flight distance that leads to contrails is in the North Atlantic at 6.7%, followed by W. EU at 6.4%. CONUS and SEA have a 32% and 74% lower likelihood of formation, respectively, closely matching the difference in the contrail EF per distance flown by region. The regional differences in contrail energy forcing per distance flown is particularly relevant given that aviation is expected to grow faster in the SEA region at a compound annual growth rate (CAGR) of 5.5% - 7.0% in terms of revenue passenger kilometers (RPK) compared with growth rates of around 2.7% and 3.1% in North America and Europe [4]. Given that flights that form over W. EU have a higher impact on average than those over CONUS and SEA, this shows that scaling contrail impacts by the distance

flown may lead to overestimates.

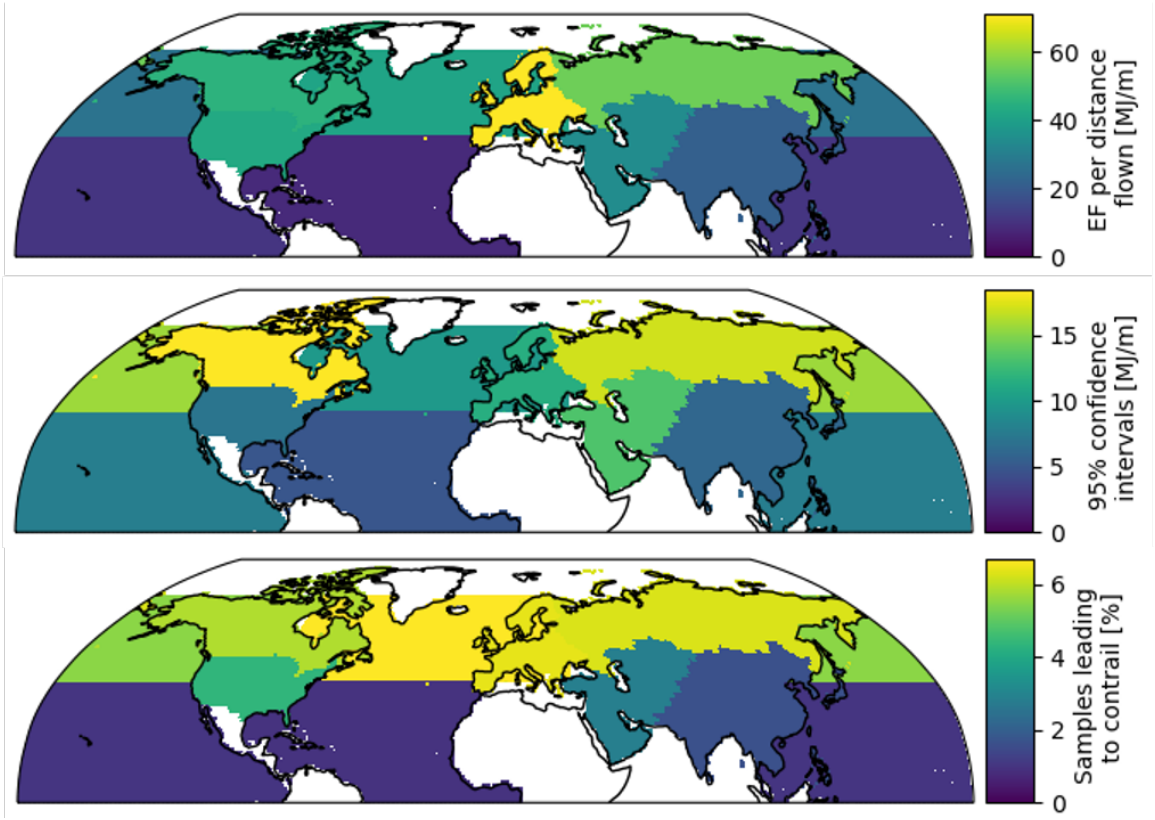

Figure 4-6: Spatial distribution of mean contrail energy forcing (EF) per distance flown (upper panel), 95% confidence interval over means (central panel), and the proportion of samples leading to a contrail (lower panel) in 11 regions in the Northern hemisphere.

Measuring impacts per distance flown is useful to understand the propensity for contrails to form and interact with radiation for a given flight or set of flights. However, to understand the average impact of contrails, Figure 4-7 shows the EF per distance flown leading to a contrail showing the net, SW, and LW components. These results highlight two key features. First, despite the net EF per distance flown being highest in W. EU, the net EF per total contrail length formed is highest in SEA, 18% higher than that over W. EU. Relative to CONUS, the EF per total contrail length formed is 33% higher over SEA. Second, the middle and lower panels of Figure 4-7 show that the regional differences are caused by differences in the LW energy forcing, rather than the SW energy forcing. The SW EF tends to vary by surface conditions, varying by 29% between minimum and maximum values over land, but varying by

106% over the oceans.

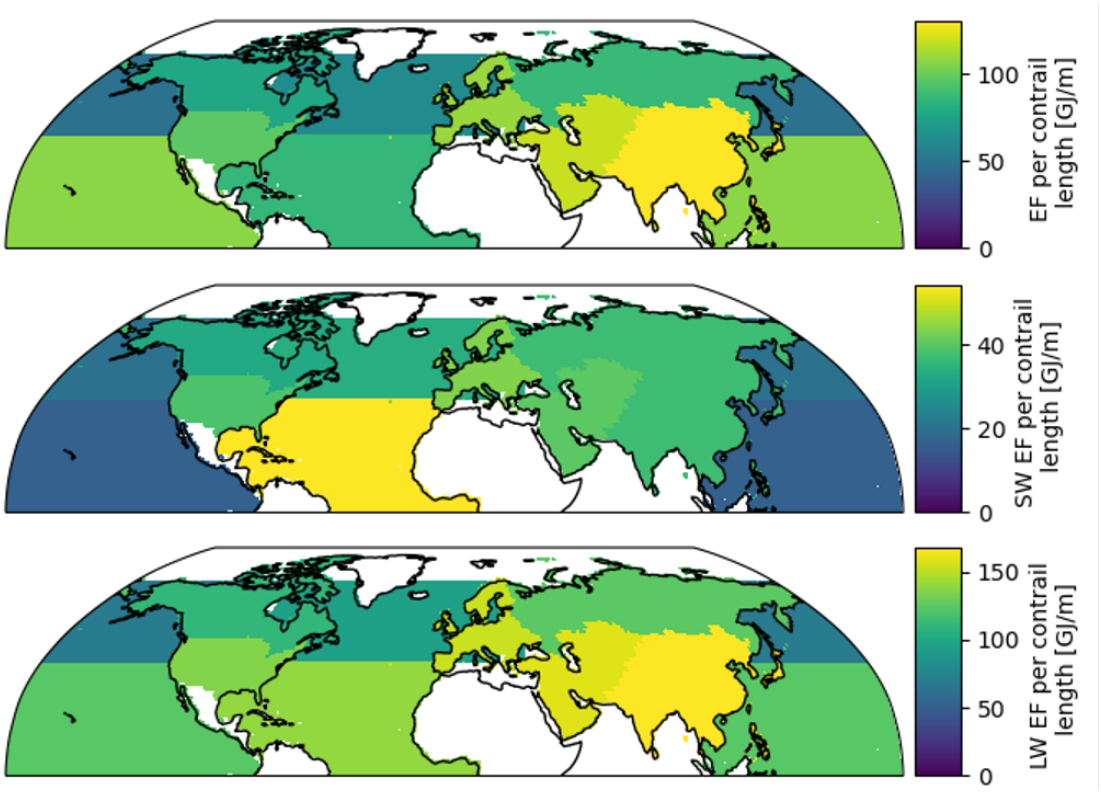

Figure 4-7: Spatial distribution of mean contrail energy forcing per distance flown leading to contrail. Upper panel portrays the net energy forcing, middle panel the shortwave (SW) energy forcing, and upper panel the longwave (LW) energy forcing in 11 regions in the Northern hemisphere.

The formation of persistent contrails was also found to change by latitude (see Chapter 3), so Figure 4-8 shows the average energy forcing per km flown by latitude. 95% confidence intervals are included in the energy forcing estimates and the red line shows the underlying flight distribution by latitude. 71% of distance flown is in the Northern mid-latitudes between around 25°N to 60°N. In this region, the average energy forcing per distance flown gradually increases, peaking at 50°N. This peak is a factor of 27 greater than the lowest energy forcing found in the tropics. Comparing 0° to 60°N with 60°S to 0°, the contrail energy forcing is found to be a factor of 2.2 lower in the Southern hemisphere than Northern hemisphere. Most of this difference is caused by the probability of distance flown leading to persistent contrails in the Southern Hemisphere being a factor of 2.0 lower than that in the Northern hemisphere.

The remaining difference is caused by contrails in the Southern hemisphere having a 16% lower energy forcing than those in the Northern hemisphere. This is particularly important in the SEA region as, despite 53% of distance flown in the SEA region occurs in the tropics, I found that the contrail energy forcing per distance flown to be a factor of 4.2 lower between $0° - 30°$N than at higher latitudes.

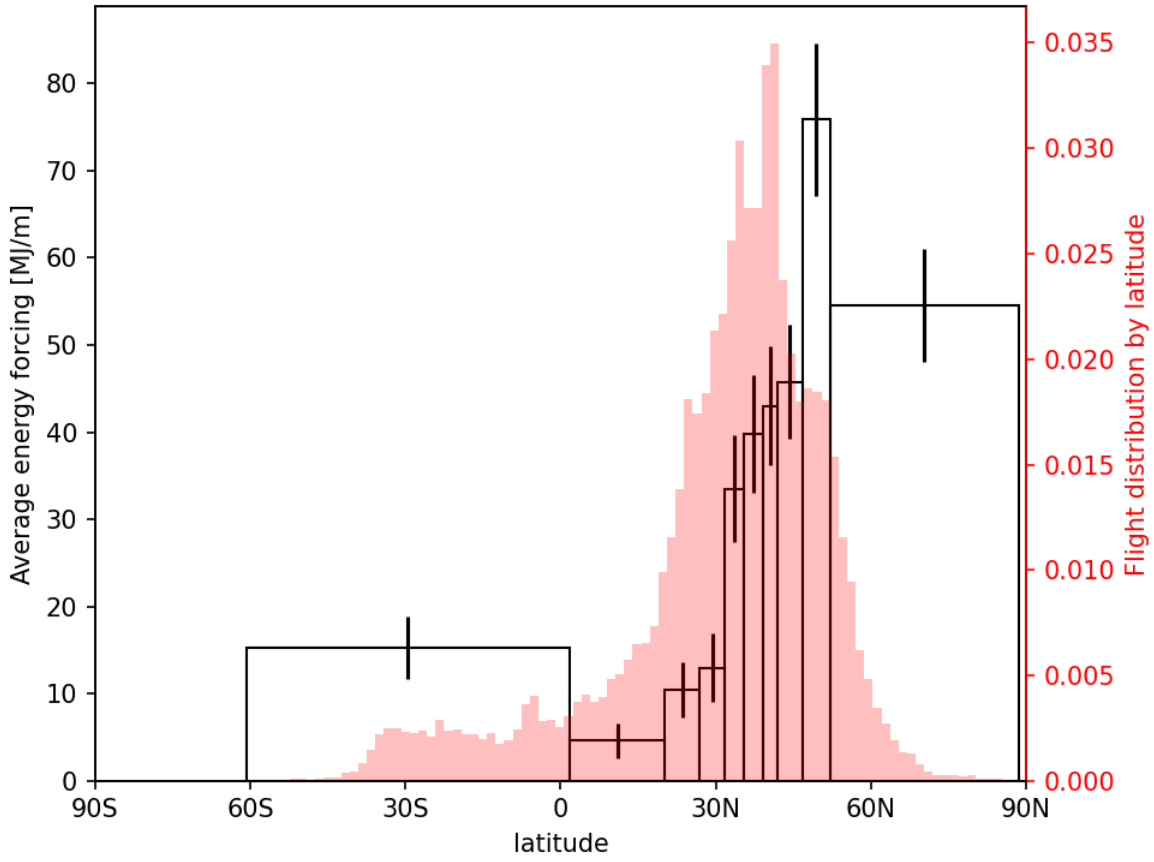

Figure 4-8: Average energy forcing per distance flow by latitude with 95% confidence intervals. Latitude bins are defined to give an equal number of samples per bin. The red bars show the number of operations by latitude.

Mannstein, Spichtinger, and Gierens [147] showed that flying up to 6,000 ft (1,830 m) lower could reduce the number of contrails that form by 50%. Fichter et al. [148] extended this and found the contrail RF to decrease approximately linearly as aircraft cruise altitudes were decreased in 2,000 ft increments. Modeling a maximum downwards shift of 6,000 ft, this led to a decrease in contrail RF of 45%. Schumann, Graf, and Mannstein [146] used a global contrail model that assumes contrails evolve

as a Gaussian plume to show that reducing aircraft cruise flight altitudes by 2,000 ft (610 m) could reduce the contrail RF by 8.1%. Figure 4-9 shows the average contrail energy forcing as a function of flight altitude as well as the underlying flight distribution in red. The flight distribution shows two cruise altitudes at around 10 km and 11 km. The 10 km peak aligns with the peak in contrail energy forcing and contrails forming 0.5 km (around 1,600 ft) below this altitude have a 56% lower impact. In comparison, the contrails forming at the aircraft cruise altitude of 11 km have a 62% lower impact that contrails forming at 10 km. AEIC assumes aircraft fly at a fixed altitude of 7,000 ft below the flight ceiling. Given how sensitive contrail results are to altitude, more precise approaches to estimate aircraft cruise altitudes should be used in future work.

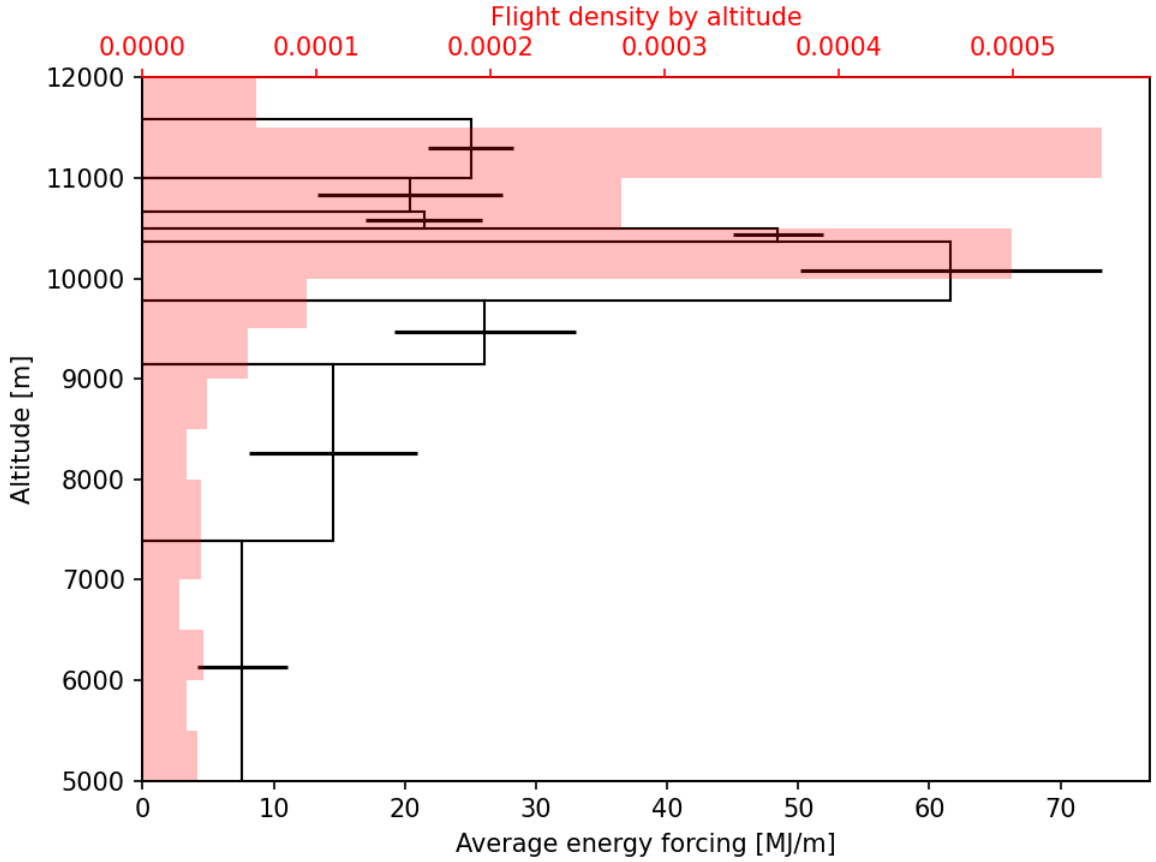

Figure 4-9: Average energy forcing per distance flow by altitude with 95% confidence intervals. Altitude bins are defined to ensure an equal number of samples per bin. The red bars show the number of operations by altitude.

4.3.3 Temporal variations of contrail impacts

The time of year that an aircraft is flown can also have an effect on the radiative forcing. Stuber et al. [117] found that the contrail net radiative forcing peaked in February at around 130 mW/m^2 and was a factor of 6 lower during June, July, and August. Similar trends were also found by Chen and Gettelman [26]. Figure 4-10 shows the monthly average, global net radiative forcing. These results match the findings found in the literature where the peak radiative forcing of contrails occurs in April and is a factor of 7.6 higher than the lowest value in July. In addition, I find that contrails are a factor of 3.4 more likely to form in MAM than JJA, while the average contrail lifetimes varies by only 7%. Combined, these two effects mean that March, April, and May (MAM) contribute around 38% of the annual average, global net RF and June, July, and August (JJA), contribute around 13.5%, while aircraft fly 11% further distance in JJA. This finding is also similar to those in Chapter 3, where the probability of a persistent contrail forming was a factor of 3.5 higher in Northern Hemisphere winter than summer.

Finally, in Figure 4-11, I show diurnal trends in contrail properties. The upper panels shows the contrail RF against the local time of the contrail, where the local time is the coordinated universal time (UTC) corrected for the local longitude. This shows that the peak net contrail impact occurs during the night between 18:00 h and 06:00 h when the shortwave forcing is lowest. I find that contrails at night cause 67% of the annual average, global net contrail RF, while this period accounts for only 36% of the overall distance flown in 2016 as depicted in the lower panel. This result matches those found by Stuber et al. [117], who found that nighttime flights accounted for 60% of the net RF in 1992. During the day, the shortwave forcing increases and causes a cooling effect offsetting 71% of the warming effect caused by the longwave radiation. The contrail energy forcing per distance flown is lowest for flights where contrails form at around 06:00 h. The longwave energy forcing varies by a factor of 1.5 between its maximum and minimum value through the day. In comparison, the shortwave portion varies by a factor of 13.4, with a maximum of 33.6

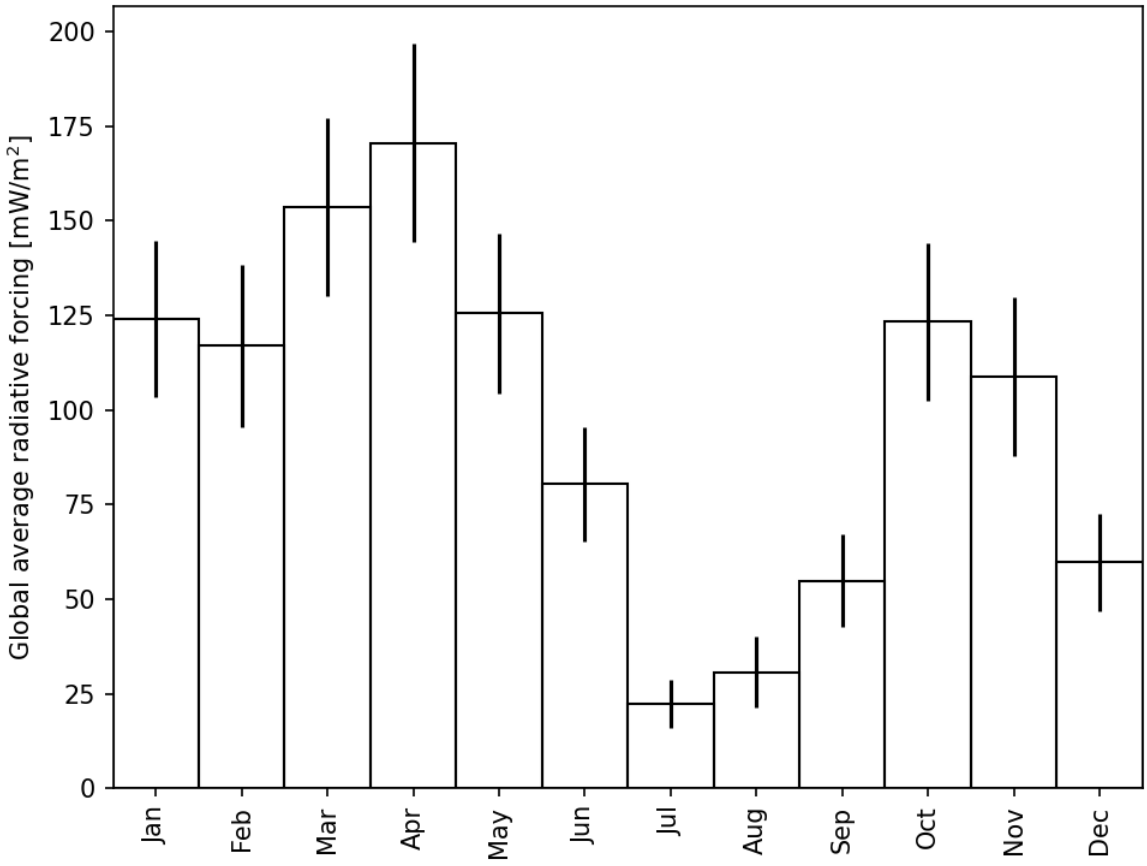

Figure 4-10: Monthly average, net contrail radiative forcing with 95% confidence intervals.

MJ/m at around 05:00 h and a minimum at around 16:00 h. At the same time, the proportion of distance flown that leads to a contrail does not depend on the time of day. This suggests that shifting to flights earlier in the morning could reduce the climate impact.

4.3.4 Effect of engine emissions on contrail impacts

To account for the variability in particle emissions between engines, the SCOPE11 method developed in Chapter 2 was used. The left panel of Figure 4-12 shows the relationship between the BC particle emissions index and the initial number of crystals that form in the contrail and survive vortex sinking. As expected, this plot shows that increasing the number of particles emitted by the engine increases the number of crystals leading to a correlation coefficient of 0.53. The aircraft mass and wingspan are

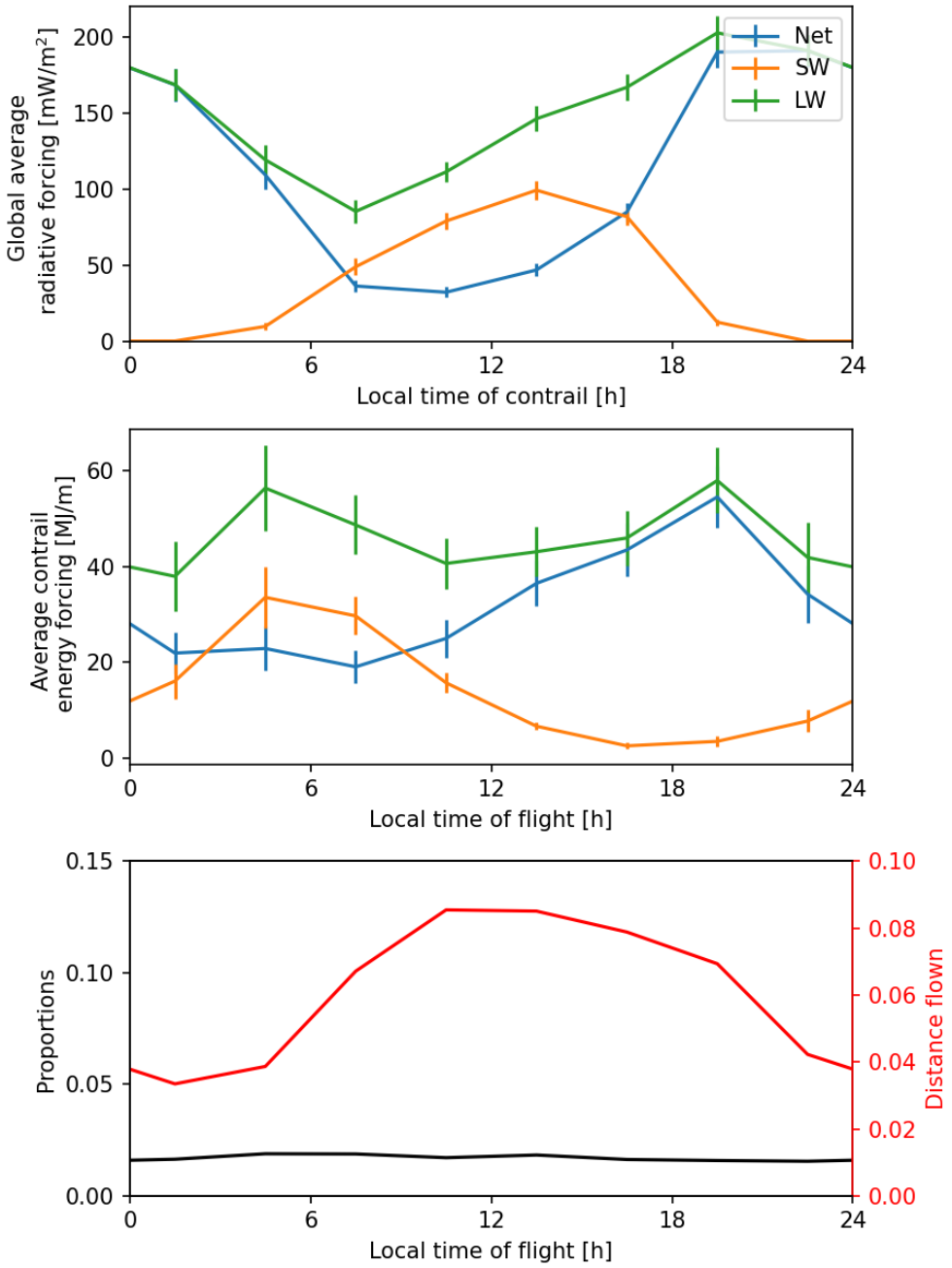

Figure 4-11: Variation of contrail by local time. Upper panel shows the average radiative forcing with 95% confidence intervals against the local time of the contrail with net RF in blue, SW RF in orange, and LW RF in green. Middle panel shows the average contrail energy forcing against the time at contrail formation and uses the same color scheme as the upper panel. Lower panel shows the proportion of distance flown by local time (solid grey line) and the proportion of distance flown leading to a persistent contrail (solid black line).

the next most important variables in determining the initial number of crystals, with correlation coefficients of -0.43 and -0.42. Both of these variables are closely related and impact the initial number of crystals as they influence the vortex sinking process. Vortex sinking causes the plume, and thus contrail, to descend and heat up, and this warming can cause crystals to evaporate after forming. Heavier aircraft, requiring wider wingspans, have a stronger vortex leading to a higher increase in temperature and thus more crystals evaporating. Finally, the initial, ambient temperature is the next most important variable in determining the initial number of crystals, with a correlation coefficient of 0.31. The ambient temperature is important as, alongside the exhaust temperature, it defines the evolution of the temperature in the exhaust plume. This determines the proportion of BC particles that get coated in sulfates and thus can form crystals.

The effect of the initial number of crystals on the contrail energy forcing is shown in the right panel of Figure 4-12. The scatter plots shows a weak relationship between the two, which suggests that increasing the initial number of crystals leads to a higher energy forcing. The weak relationship is also portrayed in the correlation coefficient of 0.14 between these two variables. As expected, the relationship of energy forcing with the BC particle emissions index is weaker (correlation coefficient of 0.10). This suggests that the variability in the number of particles emitted across engines does not drive changes in the radiative impact of a single contrail. Instead, the spatial and temporal variations in the atmospheric conditions (mainly temperature and humidity) have a stronger effect. Teoh et al. [16] incorporated the effect of variations in particle number emissions between engines with the Contrail Cirrus Prediction tool (CoCiP) focusing on the Japanese airspace, however they did not study the relationship between emissions and energy forcing. Their contrail EF was found 53.5 GJ/m (distance flown), which was a factor of 3.6 higher than that estimated from Schumann et al. [111] in a global study. However, as shown in Figure 4-6, contrail EF is higher in North America and Western Europe, so extensions from the Japanese airspace to a global domain could drive this difference.

In addition to the effects of variations in particle emissions between engines, devel-

oping technologies to reduce the number of particles emitted has also been suggested as an approach to reduce the contrail radiative forcing [12, 15, 79, 149]. My results suggest a weak, positive, relationship between the impact of an individual contrail and particle emissions, and thus the effect of reducing emissions should lead to a modest decrease in overall contrail climate impact. Conflicting results have been found in the literature, however. For example, Burkhardt, Bock, and Bier [21] found that an 80% reduction in the initial number of ice crystals could reduce the contrail RF by 50%, assuming spherically-shaped ice crystals. In contrast, Caiazzo et al. [17] found that reducing the number of particles emitted by 67% could decrease the contrail RF by up to 13% or increase it by up to 5%, with the range depending on the assumed crystal shape. For spherical crystals, they found a reduction of only 2%. Although the correlation between particle emissions and contrail EF provides a sense of the variability, it does not directly inform us on the effect of fleet-wide reductions in particle emissions on the overall contrail radiative forcing. Additional simulations with reduced particle emissions are required to study this.

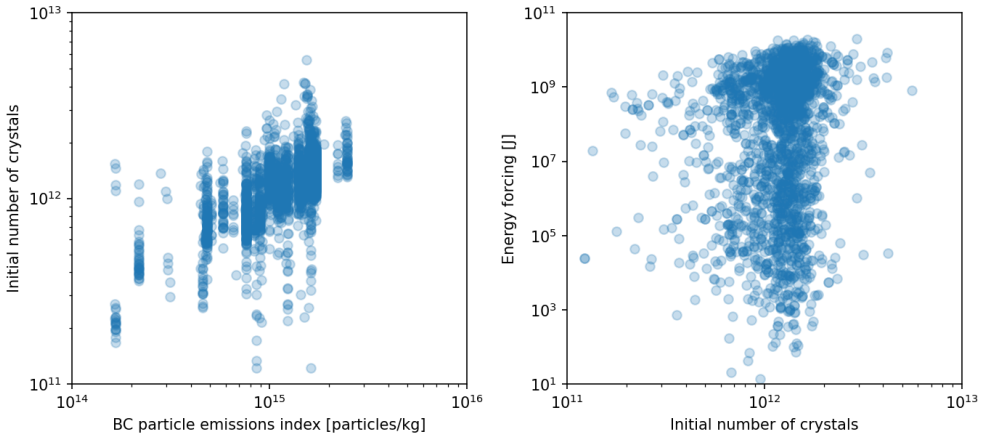

Figure 4-12: Relationship between BC particle emissions index in cruise and the initial number of crystals that form in the contrail and survive vortex sinking (left panel) and the initial number of crystals against the energy forcing (right panel).

4.3.5 MERRA-2 correction for overestimate in persistent contrail formation

Figure 4-13 shows the distribution in the net RF after correcting for the bias in MERRA-2 in identifying regions where a persistent contrail can form. Overall, the global, annual average, net RF decreases by a factor of 3.3 from 96 mW/m^2 with no correction applied to 29 mW/m^2 with corrections applied randomly by altitude, latitude, and season. I find that the 5$^{\text{th}}$ to 95$^{\text{th}}$ percentile of the corrected RF ranges from 26 to 33 mW/m^2. This correction implies that the contrail net RF reduces from being a factor of 2.9 higher than the aviation CO_2 net RF to 13% lower than this. While this approach corrects for the overestimate in the number of contrails that form, it does not account for the overestimate that may occur as the contrail ages and picks up additional ice mass. This could lead to a larger reduction in the contrail net RF.

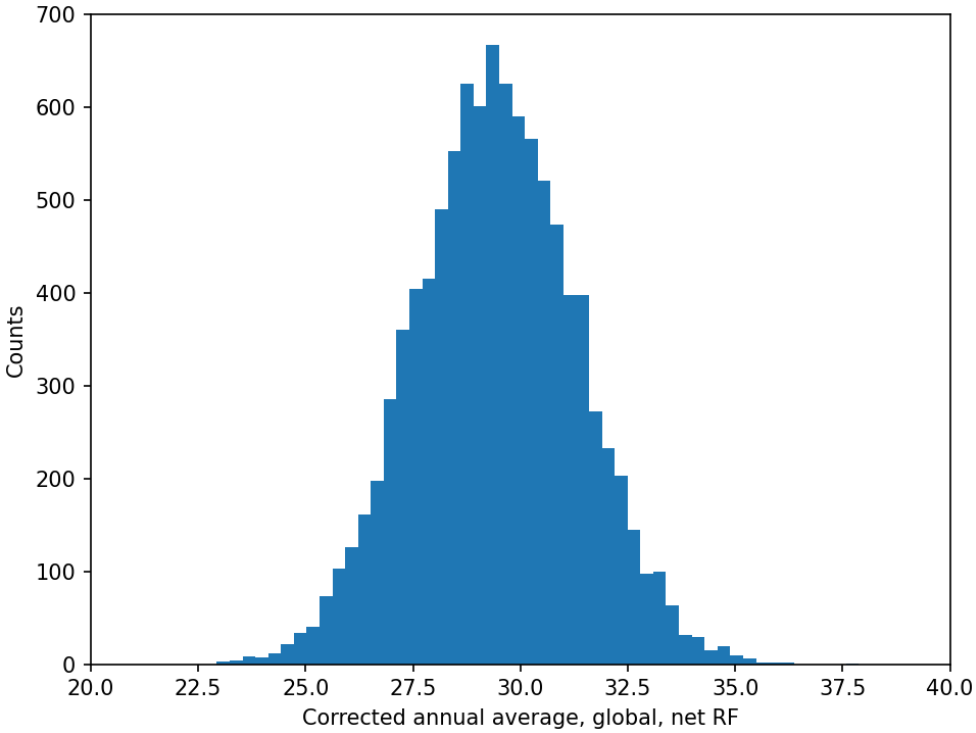

Figure 4-13: Distribution of annual average, global, net RF after corrected for MERRA-2 bias in identifying regions where persistent contrails can form

4.4 Discussion

In this chapter, I have shown that statistical inference can be used to quantify global contrail properties. The annual average, global, net radiative forcing in 2016 was found to be 96 mW/m^2, within the range of other literature estimates, and required around 20,000 samples to converge. This property makes inference for contrail properties particularly powerful for two reasons. First, additional detail can be included within APCEMM or another contrail model (e.g. large eddy simulations). For example, APCEMM did not include the effects of turbulence or radiative effects, which can affect the ice mass and ice surface area by around 20%. This can allow for more potentially more accurate estimates of global contrail properties.

The statistical approach was also used to disaggregate results in a number of ways. First, spatial trends were evaluated. The highest contrail energy forcing per distance flown was found to be in Western Europe, aligning with a peak in aircraft distance flown. This was 39% and 69% higher than the contrail energy forcing per unit distance over the contiguous United States and South and East Asia, respectively. In addition to region, the contrail energy forcing was found to be highly dependent on latitude. For example, in the South and East Asia region, the contrail energy forcing was a factor of 4.2 higher at latitudes above 30°N than below.

Current cruise altitudes vary between around 9 km and 12 km. The lower altitude aligns with a peak in the contrail energy forcing per distance flown suggesting that lowering flight altitudes may decrease the contrail impact, corroborating other literature results. However, at the 11 km altitude, the contrail energy forcing is around 62% lower than that at 10 km. This shows that uniform reductions in flight altitude may not reduce the net impact, but avoiding altitudes of around 10 km could.

Second, temporal trends were assessed. The monthly radiative forcing results showed that the highest impact occurred in April and was a factor of 7.6 than the lowest in July, despite the distance flown increasing by only 22%. The local time also affects the radiative forcing, with nighttime contrails contributing 67% of the annual average, global net RF, while 36% of the flight distance is flown at night. Comparing

to the local time at contrail formation, shortwave impacts show a six hour delay between formation and peak impact.

Finally, the effect of the overestimate in PCC in the MERRA-2 data was studied. Using the bias in the MERRA-2 versus sonde data found in Chapter 3, I find that the global, annual average, net RF could decrease by a factor of around 2.8 from 96 mW/m^2 to 30 mW/m^2. Relative to the RF due to aviation CO_2 emissions, the contrail RF would reduce from being a factor of 3.0 higher to a 13% lower. This difference could have important implications in identifying the most important climate forcers to focus on to reduce aviation's climate impact.

While the focus of this chapter has been on developing and testing the statistical inference approach, this work can be improved and extended in three key ways. First, the number of samples generated can be extended. At approximately 100,000 samples, the results have been disaggregated by a single variable across up to eleven groups. Simulating contrails from more samples would allow for disaggregating against multiple variables. For example, trends by latitude and altitude could be considered together. More samples would also allow for the breakdown of results in more groups, which is important for variables such as aircraft-engine combination and emissions. A second, related, improvement is to use variance reduction techniques that would allow for results to converge faster. For example, stratified sampling, where pseudo-random samples are generated from a population that can be separated into sub-populations (e.g.; aircraft type or latitude), or importance sampling, which can preferentially sample the input space to match a desired distribution allowing for a higher focus on, for examples, regions where contrails form. Finally, the underlying model can be changed to use a more detailed, sophisticated approach to capture more complex physical phenomena that can affect contrail evolution (e.g.; plume and atmospheric turbulence, and the effect of radiation on contrail ice mass [33, 144, 150]).

Overall, the ability to quantify the global contrail impact using around 20,000 flight samples presents a unique opportunity to improve the current understanding of contrails at a global scale. The adaptability of the method can make it useful for researchers interested in applying more detail to the evolution of contrails and

showing the effect of these changes to the global contrail impact.s

Chapter 5

Conclusions

This thesis aims to improve understanding of the global contrail climate impact. I have focused on three aspects of global contrail modeling approaches - predicting particle number emissions, the accuracy of global meteorological datasets, and the modeling approach for global numerical estimates.

5.1 Summary of findings and contributions

In Chapter 2, a new approach to estimate the number of black carbon (BC) particles emitted from the exhaust of aircraft engines is developed. The approach uses two complementary datasets that relate smoke number measurement to the BC mass concentration, quantify losses in the measurement system, and connect mass emissions to particle number emissions by estimating the geometric mean diameter (GMD) of particles. The method is applied to existing BC mass and particle number measurements achieving an R^2 of 0.80 and 0.82, respectively. Global BC emissions for all operations in 2015 were estimated to be 2.0 Gg/year (95% CI $= 1.7 - 2.3$) and 2.42×10^{26} particles/year (95% CI $= 1.58 - 3.81 \times 10^{26}$).

In Chapter 3, I quantify the error in using meteorological data provided by reanalysis models like ERA5 and MERRA-2. Most numerical estimates of the global contrail impact rely on reanalysis models or other numerical simulations of the atmosphere to estimate temperature and humidity. However, no studies have systematically studied

the accuracy of using such datasets. Using data from 793,044 radiosondes, persistent contrails forming at cruise altitudes in 30°N – 60°N are found to be overestimated by factors of 2.0 and 3.5 for ERA5 and MERRA-2, respectively. Seasonal and inter-annual trends are well-reproduced by both models ($R^2 = 0.79$ and 0.74). I also define the evaporation depth, which measures the depth to which a contrail can survive based on the available ice mass and is thus a measure of contrail lifetime. This metric is found to be overestimated by 17% in ERA5 and 45% in MERRA-2 suggesting the contrail lifetime may be overestimated. Finally, the reanalyses incorrectly identify individual regions that could form persistent contrails 87% and 52% of the time, respectively. These results suggest that contrail models currently overestimate the number and lifetime of persistent contrails.

Finally, in Chapter 4, I use contrail inference to take advantage of a intermediate fidelity contrail model, APCEMM, by running it for a random sample of the distance flown by aircraft in 2016 and calculate the contrail physical and radiative properties. For an aviation schedule in 2016, the global, annual average, contrail instantaneous radiative forcing was found to be 96 mW/m^2, within around 6% of other literature estimates. The approach also allows for disaggregating results by input variables. The spatial distribution of impacts showed that flights over Western Europe had the highest contrail energy forcing per unit flown, 39% and 66% higher than the same metric over the contiguous United States and South and East Asia. A major factor affecting was latitude and I found that the peak contrail energy forcing per distance flown was at a latitude of around 50°N. Temporal effects were also studied and flights during the summer were found to be up to a factor of 7.6 lower than other months. Similarly, nighttime flights were found to contribute to 67% of the annual average impact despite accounting for only 36% of distance flown. I also used the particle emissions approach as an input to APCEMM and found that it had a correlation coefficient of 0.53 with the initial number of crystals that form in the contrail. In comparison, it had a smaller correlation coefficient of 0.10 with the energy forcing per contrail, suggesting that approaches to reduce particle number emissions may not have a strong effect on contrail RF. Finally, the effect of the overestimate in PCC

in the MERRA-2 data was applied to the global, annual average, net RF, decreasing it by a factor of 2.8 from 96 mW/m^2 to 30 mW/m^2. This difference could have important implications in identifying the most important climate forcers to focus on to reduce aviation's climate impact. These results display the potential of statistical inference to quantify the impact of contrails at a global scale and further dissect the impacts in multiple ways.

5.2 Future work

As emissions reductions becomes a stronger priority for the aviation industry [151], new combustor technologies are being developed, such as the lean-burn combustor developed by GE [152]. Since the black carbon emissions method in this thesis relies on smoke number data, as measurement data for new technologies becomes available, the same equations can be used and re-fitted for the new technologies. Computational methods to estimate black carbon emissions from the combustor that do not require emissions measurements are also being developed and these can provide more insight on approaches to reduce particle emissions [153]. Finally, multiple studies find that contrail ice particles form on sulfate-coated BC particles [11, 136], which requires information on the number of volatile particles emitted by the engine. Extending this approach to account for volatile particles and using it for estimating the number of crystals that form would provide a major advancement.

When quantifying the biases in the ERA5 and MERRA-2 reanalysis datasets, a single source of upper tropopsheric, lower stratospheric (UTLS) water vapor measurements - sondes - was used. While this is a large, pervasive, and reliable dataset, and provides a vertical snapshot of the atmosphere, flight data and satellite data can also provide more information in the UTLS. These could be useful to provide additional information to quantify the accuracy of reanalysis data. In addition, my work focused on the formation of persistent contrails. A logical extension would be to quantify the overestimate in the contrail physical and radiative properties over its lifetime. This would need to account for potential differences in the overestimate by

altitude and latitude, but also account for aircraft/engine parameters, such as aircraft mass, BC particle emissions, and engine overall efficiency, that can affect the contrail throughout its lifetime. Correcting for the biases found would be invaluable for improving estimates of global contrail coverage and radiative forcing, helping policy-makers and industry identify the most important climate forcers to focus on. Finally, a key takeaway from this work is the need for more UTLS measurements and methods to constrain water vapor concentrations in numerical weather simulations.

The contrail inference method is a tool that allows for using intermediate-resolution models to quantify the contrail physical and radiative properties on a global scale. Two major advancements could be made to this work. Firstly, a simple, unbiased, random sampling approach is used. While this is sufficient for quantifying global contrail impacts, it is difficult to quantify mean contrail properties in regions where there are fewer flights, since the random sampling would lead to an insufficient number of samples to converge for these regions. This could be important given that around 20% of contrails account for 78% of the annual average, global, net RF. Stratified or importance sampling approaches that can ensure a wider coverage of samples could improve the ability to simulate contrails in spatial regions or for aircraft types that are not commonly found in the schedule. Secondly, while APCEMM is an invaluable tool for the purposes of this work, improvements to the contrail modeling approach could be made in two directions. (1) APCEMM does not account for radiative effects or turbulence, which could have an important effect on contrail evolution [144]. The contrail inference framework allows for the inclusion of more complex physical effects. (2) The computational resources required to simulate APCEMM allow for around 10,000 contrails to be simulated within a 2 month timeframe. Additional samples would allow for disaggregating impacts by multiple variables and still retain statistical convergence in the results. As such, faster models that can still simulate the key physics of contrail evolution could be valuable to extend the results.

Overall, the methods developed in this thesis improve the understanding of and ability to model contrails both individually, with the use of the particle emissions approach, and at a global scale, via the reanalysis bias quantification and the use of

statistical inference. While these methods should improve the accuracy of global contrail radiative forcing results, this should be measured using two approaches. Firstly, observations of contrails must be used to constrain the results from APCEMM as well to identify regions of the atmosphere that are favorable for contrail formation. In-situ measurements of particle emissions and contrail ice particles are invaluable to understand how contrail ice crystals form and persist within the first few minutes to hours [79]. Observations of contrails using satellite images can also identify contrail forming regions, which can be used to constrain the output from reanalysis models, as well be used to quantify the accuracy in contrail coverage and radiative forcing estimates as well [154]. Secondly, using faster, simplified approaches to simulating contrails with statistical inference could allow modelers to quantify the uncertainty in the underlying models using Monte Carlo simulations. This would quantify the effect of parameter uncertainties in the overall contrail radiative forcing, a topic that has not yet been studied in detail.

Appendix A

Derivation of volumetric flow rate

The volumetric flow rate, Q, is a parameter required to convert the BC mass concentration to an emissions index. Derivations in the literature have found different coefficients and do not show this derivation as a function of the fuel hydrogen content, H_c. As such, we provide an overview of the method for unmixed engines following Stettler et al [67], but generalize this for a fuel of any hydrogen content.

We assume the fuel can be written in the form C_nH_m and the resulting combustion reaction is:

$$C_nH_m + (n + \tfrac{m}{4}) O_2 \longrightarrow n\, CO_2 + \tfrac{m}{2}\, H_2O$$

which assumes 100% combustion efficiency from fuel to products. For $H_c = 13.8\%$ and $n = 12$, we find $m = 22.8928$ and the resulting moles per emissions product can be calculated.

To estimate the volumetric flow rate, we begin with conservation of mass. We can convert between our reaction equation and mass by multiply by the molecular masses of each species. As such, 1 kg of fuel would require $(n + \frac{m}{4}) \frac{M_{O_2}}{M_{C_nH_m}}$ kg of O_2 for complete combustion and similar calculations can be made for the remaining species. Conservation of mass thus results in:

$$\begin{aligned}\dot{m}_{\text{core|exhaust}}\left[\frac{\text{kg}}{\text{kg}_{\text{fuel}}}\right] &= \dot{m}_{\text{core|in}} + \dot{m}_{\text{combustion}} \\ &= 0.768{\cdot}\text{AFR}\cdot \text{N}_2 + 0.232{\cdot}\text{AFR}\cdot \text{O}_2 \\ &- \left(n+\frac{m}{4}\right)\frac{M_{\text{O}_2}}{M_{\text{C}_\text{n}\text{H}_\text{m}}}\cdot \text{O}_2 + n\frac{M_{\text{CO}_2}}{M_{\text{C}_\text{n}\text{H}_\text{m}}}\cdot \text{CO}_2 \\ &+ \frac{m}{2}\frac{M_{\text{H}_2\text{O}}}{M_{\text{C}_\text{n}\text{H}_\text{m}}}\cdot \text{H}_2\text{O}\end{aligned} \tag{A.1}$$

where M_i refers to the molecular mass of species . We use the standard atomic weight values from the International Union of Pure and Applied Chemistry (IUPAC) [155]. The volumetric flow rate is then estimated by scaling each term by the appropriate species' density. The densities are calculated at STP using the ideal gas law.

$$\begin{aligned}Q_{\text{core|exhaust}}\left[\frac{\text{m}^3}{\text{kg}_{\text{fuel}}}\right] &= \left(\frac{0.768}{\rho_{\text{N}_2}}+\frac{0.232}{\rho_{\text{O}_2}}\right)\cdot \text{AFR} - \left(n+\frac{m}{4}\right)\frac{M_{\text{O}_2}}{\rho_{\text{O}_2}M_{\text{C}_\text{n}\text{H}_\text{m}}}\text{O}_2 \\ &+ n\frac{M_{\text{CO}_2}}{\rho_{\text{CO}_2}M_{\text{C}_\text{n}\text{H}_\text{m}}}\cdot \text{CO}_2 + \frac{m}{2}\frac{M_{\text{H}_2\text{O}}}{\rho_{\text{H}_2\text{O}}M_{\text{C}_\text{n}\text{H}_\text{m}}}\cdot \text{H}_2\text{O}\end{aligned} \tag{A.2}$$

For $n = 12$ and $m = 22.8928$, the resulting volumetric flow rate is:

$$\begin{aligned}Q_{\text{core|exhaust}}\left[\frac{\text{m}^3}{\text{kg}_{\text{fuel}}}\right] &= (0.614+0.163)\cdot \text{AFR} - 2.376 + 1.609 + 1.534 \\ &= 0.777\cdot \text{AFR} + 0.767\end{aligned} \tag{A.3}$$

For a mixed turbofan engine, the bypass and core streams are internally mixed, thus the mass concentration is based on the combined flow streams. As such, the volumetric flow rate is adjusted by a factor of $(1+\beta)$, where β is the bypass ratio.

$$Q_{\text{mixed|exhaust}}\left[\frac{\text{m}^3}{\text{kg}_{\text{fuel}}}\right] = 0.777\cdot \text{AFR}\cdot(1+\beta) + 0.767 \tag{A.4}$$

Appendix B

Gas turbine calculations

In this section, an overview is provided of the calculation procedure and key equations solved to estimate the engine exhaust flow area (combined bypass and core flow area), as well as the exhaust temperature. Both procedures use a similar set of equations, however the iterative calculation approach and the available input parameters differ between the two.

B.1 Estimating the exhaust area

To calculate the engine exhaust flow area, we begin with publicly available data from the engine emissions data bank (EEDB) [75]. The EEDB provides ground, sea-level static, operating conditions of the engine. At the 100% of an engine's rated thrust (F_{00}), the overall pressure ratio (OPR), bypass ratio (BPR), and fuel flow rate ($\dot{m}_f$) are provided. Finally, I use the jet velocity ratio, α, which is calculated as the core exhaust jet velocity, V_{jc}, over the bypass exhaust jet velocity, V_{jc}. α is used a design parameter in order to maximize the engine overall efficiency, η_o, and is set to be 0.7 (Dr. Jayant Sabnis, personal communication, October 16, 2020). Finally, we assume the ambient conditions to follow the normal temperature and pressure conditions where the temperature and pressure at ground conditions are 288 K and 1013 hPa, respectively.

To calculate the internal temperature and pressure within the engine, I found an

iterative approach was required. To begin this, an initial guess is made for fan pressure ratio (FPR). This is used to calculate the conditions at location 13 downstream of the fan as

$$P_{t13} = \mathrm{FPR} P_{t2} \tag{B.1}$$

$$T_{t13} = T_{t2} \mathrm{FPR}^{\frac{\gamma_c - 1}{\gamma_c \eta_{\mathrm{fan}}}} \tag{B.2}$$

where P and T represent the pressure and temperature, respectively, subscript 2 and 13 represent conditions upstream and downstream of the fan, $\gamma_c = 1.4$ is the specific heat ratio of the air passing through the compressor, and $\eta_{\mathrm{fan}} = 0.92$ is the fan polytropic efficiency. Using α, the core exhaust jet velocity can be calculated as

$$V_{j,c} = \frac{V_{j,b}}{\alpha} \tag{B.3}$$

and using F_{00}, the mass flow rate through the core of the engine, $\dot{m}_c$, is calculated as

$$\dot{m}_c = \frac{F_{00}}{V_{j,c}\left(1 + \alpha \mathrm{BPR}\right)} \tag{B.4}$$

Using OPR, the conditions downstream at location 3 downstream of the compressor can be calculated as

$$P_{t3} = \mathrm{OPR} P_{t2} \tag{B.5}$$

$$T_{t3} = T_{t2} \mathrm{OPR}^{\frac{\gamma_c - 1}{\gamma_c \eta_{\mathrm{com}}}} \tag{B.6}$$

where $\eta_{\mathrm{com}} = 0.90$ is the compressor polytropic efficiency. The compressor typically consists of two or three separate components (e.g. high-pressure and low-pressure compressor), however, information on the pressure ratio of each part of compressor is not always publicly available. For this reason, the compressor is treated as a

single component. Using the polytropic efficiency is particularly advantageous in this situation as it is independent of the baseline pressure unlike the adiabatic efficiency [156].

Using the input $\dot{m}_f$, the conditions downstream of the combustor at location 4 can be estimated as

$$P_{t4} = P_{t3} \tag{B.7}$$

$$T_{t4} = \frac{\frac{\dot{m}_c}{\dot{m}_f} c_{p,c} T_{t3} + \mathrm{LCV}}{c_{p,t}\left(1 + \frac{\dot{m}_c}{\dot{m}_f}\right)} \tag{B.8}$$

where $c_{pc} = 1005$ J/K/kg and $c_{pt} = 1250$ J/K/kg are the heat capacity at constant pressure in the compressor and turbine, respectively, and LCV = 43.3 MJ/kg is the lower calorific value of the fuel. The combustor is assumed to have no pressure loss. While this is not physically correct since the flow requires that the pressure reduces slightly in order to move forwards through the combustor, it has a small effect on the overall efficiency and thus we do not account for it. Finally, the power between the compressor and turbine is matched in order to calculated the temperature downstream of the turbine at location 5 as

$$T_{t5} = T_{t4} - (T_{t3} - T_{t2}) - (T_{t13} - T_{t2}) \frac{c_{p,c}}{c_{p,t}} \mathrm{BPR} \tag{B.9}$$

The associated pressure, P_{t5}, is calculated as

$$T_{t4,\mathrm{is}} = T_{t4} - (T_{t4} - T_{t5})/\eta_{\mathrm{tur}} \tag{B.10}$$

$$P_{t5} = P_{t4}\left(\frac{T_{t5,\mathrm{is}}}{T_{t4}}\right)^{\frac{\gamma_t}{\gamma_t - 1}} \tag{B.11}$$

where η_{tur} is the adiabatic efficiency of the turbine and $\gamma_t = 1.3$ is the specific heat ratio of the air passing through the turbine. Finally, this provides a second approach to calculate the core exhaust jet velocity, $V_{j,c}$, as

$$V_{j,c}* = \sqrt{2c_{p,t}T_{t5}\left(1 - \left(\frac{P_{\text{amb}}}{P_{t5}}\right)^{\frac{\gamma_t - 1}{\gamma_t}}\right)} \tag{B.12}$$

The iterative solver optimizes on the FPR until the squared error between $V_{jc,}*$ and $V_{j,c}$ converges to a constant value with a tolerance of 10^{-14}. Assuming the flow to be perfectly expanded, the bypass flow exhaust area, A_{19}, can be calculated as

$$T_{19} = T_{t13} - \frac{V_{jb}^2}{2c_{pc}} \tag{B.13}$$

$$\rho_{19} = \frac{P_{\text{amb}}}{R_c T_{19}} \tag{B.14}$$

$$A_{19} = \frac{\dot{m}_c \text{BPR}}{\rho_{19} V_{j,b}} \tag{B.15}$$

where subscript 19 represent conditions at the exhaust of the bypass, ρ is the density of air, and $R_c = 287$ J/K/kg is the specific gas constant of dry air. The core flow exhaust area, A_9 is calculated following the same approach as

$$T_9 = T_{t13} - \frac{V_{j,c}^2}{2c_{p,t}} \tag{B.16}$$

$$\rho_9 = \frac{P_{\text{amb}}}{R_t T_9} \tag{B.17}$$

$$A_9 = \frac{\dot{m}_c}{\rho_9 V_{j,b}} \tag{B.18}$$

where subscript 9 represent conditions at the exhaust of the core. The combined area, $A = A_9 + A_{19}$, is used as an input to APCEMM.

B.2 Estimating exhaust temperature

The iterative procedure for estimating the exhaust temperature is analogous to that for the exhaust area, however information for engines in cruise are not publicly available. AEIC provides information on fuel flow rate using aircraft performance data

from BADA [112]. Assuming International Standard Atmosphere (ISA) conditions, the altitude and flight speed define the stagnation temperature and pressure at the engine inlet. This is used to calculate the non-dimensional fuel flow rate $\hat{m}_f$, calculated as

$$\hat{m}_f = \frac{\dot{m}_f \mathrm{LCV}}{\sqrt{c_{p,c} T_{t2,c}} A^2 P_{t2,c}} \tag{B.19}$$

where subscript c represents cruise conditions. The EEDB also includes fuel flow rate data for four different thrust settings for each engine at sea-level, static, conditions - idle conditions with the non-dimensional thrust setting, $F/F_{00} = 4\%$, approach conditions with $F/F_{00} = 30\%$, climb-out conditions with $F/F_{00} = 85\%$, and take-off conditions with $F/F_{00} = 100\%$. These thrust settings are related with the non-dimensional fuel flow rate at the ground conditions. Using $\hat{m}_f$ at cruise, the F/F_{00} at cruise conditions can be linearly interpolated from the ground-based EEDB data points. Examples of the relationship between non-dimensional thrust and non-dimensional fuel flow rate are shown in Figure B-1 for five different engines. These results show that a simple interpolation approach is reasonable for the ground conditions.

By interpolating from relationships similar to the ones in Figure B-1, the thrust can be calculated as $F_{\mathrm{c}} = (F/F_{00})_{\mathrm{c}} F_{00}$, where subscript c refers to cruise conditions. Similar, the pressure ratio at cruise, $\mathrm{OPR}_{\mathrm{c}}$, is estimated as

$$\mathrm{OPR}_{\mathrm{gc}} = 1 + \mathrm{OPR} \frac{F}{F_{00\,\mathrm{c}}} \tag{B.20}$$

The estimated values of thrust, pressure ratio, and fuel flow rate at cruise can be combined with the exhaust areas calculated in Section B.1. The overall approach is similar, but I found that I was required to guess the core mass flow rate in addition to the FPR. Since two variables are being guessed, a second variable is also required to converge on. In this case, I use the thrust, F, and the core flow exhaust area, A_9, to converge on the FPR and $\dot{m}_c$.

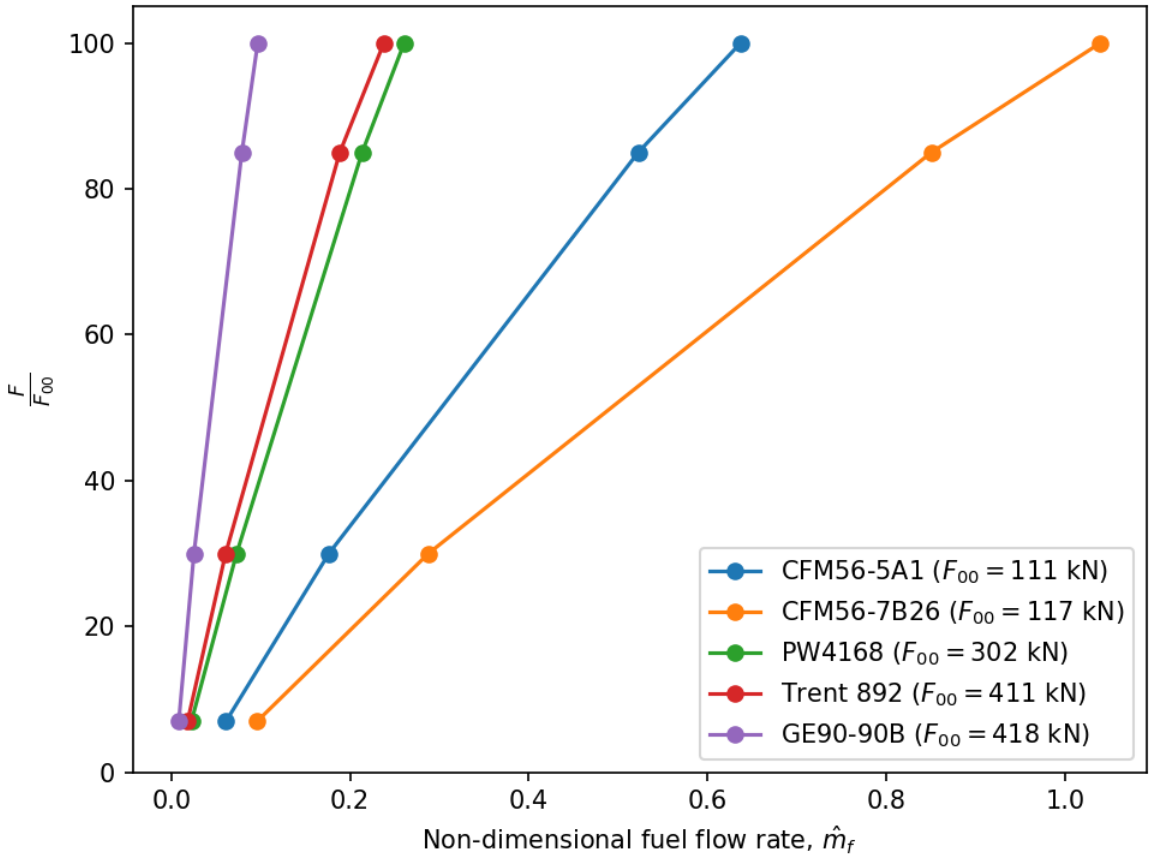

Figure B-1: Non-dimensional fuel flow rate against non-dimensional thrust for five different engines.

Bibliography

[1] IPCC. *IPCC, 2013: Climate Change 2013: The Physical Science Basis. Contribution of Working Group I to the Fifth Assessment Report of the Intergovernmental Panel on Climate Change*. Tech. rep. 2013.

[2] IPCC. *Summary for Policymakers. In: Climate Change 2013: The Physical Science Basis. Contribution of Working Group I to the Fifth Assessment Report of the Intergovernmental Panel on Climate Change [Stocker, T.F., D. Qin, G.-K. Plattner, M. Tignor, S.K. Allen, J. Boschung, A. Nauels, Y. Xia, V. Bex and P.M. Midgley (Eds.)]*. 2013.

[3] Airbus. *Global Market Forecast 2017-2036*. http://www.airbus.com/aircraft/market/global-market-forecast.html. 2017.

[4] Boeing. *Current Market Outlook 2017*. http://www.boeing.com/commercial/market/current-market-outlook-2017/. 2017.

[5] D. S. Lee et al. "The Contribution of Global Aviation to Anthropogenic Climate Forcing for 2000 to 2018". en. In: *Atmospheric Environment* 244 (Jan. 2021), p. 117834. ISSN: 1352-2310. DOI: 10.1016/j.atmosenv.2020.117834.

[6] E Schmidt. "Die Entstehung von Eisnebel Aus Den Auspuffgasen von Flugmotoren". In: *Schriften der Deutschen Akademie der Luftfahrtforschung* Heft 44 (1941).

[7] H. Appleman. "The Formation of Exhaust Condensation Trails by Jet Aircraft". In: *Bulletin of the American Meteorological Society* 34.1 (Jan. 1953), pp. 14–20. ISSN: 0003-0007. DOI: 10.1175/1520-0477-34.1.14.

[8] Schumann. "Influence of Propulsion Efficiency on Contrail Formation". In: *Aerospace Science and Technology* 4.6 (Sept. 2000), pp. 391–401. ISSN: 1270-9638. DOI: 10.1016/S1270-9638(00)01062-2.

[9] P. J. DeMott et al. "Ice Formation by Black Carbon Particles". In: *Geophysical Research Letters* 26.16 (1999), pp. 2429–2432. ISSN: 1944-8007. DOI: 10.1029/1999GL900580.

[10] Andrew Heymsfield et al. "Contrail Microphysics". In: *Bulletin of the American Meteorological Society* 91.4 (Apr. 2010), pp. 465–472. ISSN: 0003-0007. DOI: 10.1175/2009BAMS2839.1.

[11] O. B. Popovicheva et al. "Aircraft Engine Soot as Contrail Nuclei". In: *Geophysical Research Letters* 31.11 (2004). ISSN: 1944-8007. DOI: 10.1029/2003GL018888.

[12] B. Kärcher and F. Yu. “Role of Aircraft Soot Emissions in Contrail Formation”. In: *Geophysical Research Letters* 36.1 (Jan. 2009). ISSN: 0094-8276. DOI: 10.1029/2008GL036649.

[13] B. Kärcher et al. “The Microphysical Pathway to Contrail Formation”. In: *Journal of Geophysical Research: Atmospheres* 120.15 (2015), pp. 7893–7927. ISSN: 2169-8996. DOI: 10.1002/2015JD023491.

[14] Ulrich Schumann et al. “Contrails: Visible Aviation Induced Climate Impact”. en. In: *Atmospheric Physics*. Ed. by Ulrich Schumann. Research Topics in Aerospace. Springer Berlin Heidelberg, 2012, pp. 239–257. ISBN: 978-3-642-30182-7 978-3-642-30183-4. DOI: 10.1007/978-3-642-30183-4_15.

[15] Bernd Kärcher. “Formation and Radiative Forcing of Contrail Cirrus”. en. In: *Nature Communications* 9.1 (May 2018), p. 1824. ISSN: 2041-1723. DOI: 10.1038/s41467-018-04068-0.

[16] Roger Teoh et al. “Mitigating the Climate Forcing of Aircraft Contrails by Small-Scale Diversions and Technology Adoption”. In: *Environmental Science & Technology* 54.5 (Mar. 2020), pp. 2941–2950. ISSN: 0013-936X. DOI: 10.1021/acs.est.9b05608.

[17] Fabio Caiazzo et al. “Impact of Biofuels on Contrail Warming”. en. In: *Environmental Research Letters* 12.11 (2017), p. 114013. ISSN: 1748-9326. DOI: 10.1088/1748-9326/aa893b.

[18] Inés Sanz-Morère et al. “Reducing Uncertainty in Contrail Radiative Forcing Resulting from Uncertainty in Ice Crystal Properties”. In: *Environmental Science & Technology Letters* 7.6 (June 2020), pp. 371–375. DOI: 10.1021/acs.estlett.0c00150.

[19] Prem Lobo et al. “Demonstration of a Regulatory Method for Aircraft Engine Nonvolatile PM Emissions Measurements with Conventional and Isoparaffinic Kerosene Fuels”. In: *Energy & Fuels* 30.9 (Sept. 2016), pp. 7770–7777. ISSN: 0887-0624. DOI: 10.1021/acs.energyfuels.6b01581.

[20] Prem Lobo et al. “Comparison of Standardized Sampling and Measurement Reference Systems for Aircraft Engine Non-Volatile Particulate Matter Emissions”. en. In: *Journal of Aerosol Science* 145 (July 2020), p. 105557. ISSN: 0021-8502. DOI: 10.1016/j.jaerosci.2020.105557.

[21] Ulrike Burkhardt, Lisa Bock, and Andreas Bier. “Mitigating the Contrail Cirrus Climate Impact by Reducing Aircraft Soot Number Emissions”. En. In: *npj Climate and Atmospheric Science* 1.1 (Oct. 2018), p. 37. ISSN: 2397-3722. DOI: 10.1038/s41612-018-0046-4.

[22] S. Twomey. “Pollution and the Planetary Albedo”. In: *Atmospheric Environment (1967)* 8.12 (Dec. 1974), pp. 1251–1256. ISSN: 0004-6981. DOI: 10.1016/0004-6981(74)90004-3.

[23] U. Schumann. “A Contrail Cirrus Prediction Model”. In: *Geosci. Model Dev.* 5.3 (May 2012), pp. 543–580. ISSN: 1991-9603. DOI: 10.5194/gmd-5-543-2012.

[24] Ulrike Burkhardt and Bernd Kärcher. “Global Radiative Forcing from Contrail Cirrus”. en. In: *Nature Climate Change* 1.1 (Apr. 2011), pp. 54–58. ISSN: 1758-678X. DOI: 10.1038/nclimate1068.

[25] Ulrike Burkhardt and Bernd Kärcher. “Process-Based Simulation of Contrail Cirrus in a Global Climate Model”. en. In: *Journal of Geophysical Research: Atmospheres* 114.D16 (Aug. 2009), p. D16201. ISSN: 2156-2202. DOI: 10.1029/2008JD011491.

[26] C.-C. Chen and A. Gettelman. “Simulated Radiative Forcing from Contrails and Contrail Cirrus”. English. In: *Atmospheric Chemistry and Physics* 13.24 (Dec. 2013), pp. 12525–12536. ISSN: 1680-7316. DOI: https://doi.org/10.5194/acp-13-12525-2013.

[27] Ronald Gelaro et al. “The Modern-Era Retrospective Analysis for Research and Applications, Version 2 (MERRA-2)”. In: *Journal of Climate* 30.14 (May 2017), pp. 5419–5454. ISSN: 0894-8755. DOI: 10.1175/JCLI-D-16-0758.1.

[28] Jonathan H. Jiang et al. “An Assessment of Upper Troposphere and Lower Stratosphere Water Vapor in MERRA, MERRA2, and ECMWF Reanalyses Using Aura MLS Observations”. en. In: *Journal of Geophysical Research: Atmospheres* 120.22 (2015), pp. 11, 468–11, 485. ISSN: 2169-8996. DOI: 10.1002/2015JD023752.

[29] Sean M. Davis et al. “Assessment of Upper Tropospheric and Stratospheric Water Vapor and Ozone in Reanalyses as Part of S-RIP”. English. In: *Atmospheric Chemistry and Physics* 17.20 (Oct. 2017), pp. 12743–12778. ISSN: 1680-7316. DOI: 10.5194/acp-17-12743-2017.

[30] Lisa Bock and Ulrike Burkhardt. “The Temporal Evolution of a Long-Lived Contrail Cirrus Cluster: Simulations with a Global Climate Model”. en. In: *Journal of Geophysical Research: Atmospheres* 121.7 (2016), pp. 3548–3565. ISSN: 2169-8996. DOI: 10.1002/2015JD024475.

[31] N. Lamquin et al. “Evaluation of Upper Tropospheric Humidity Forecasts from ECMWF Using AIRS and CALIPSO Data”. English. In: *Atmospheric Chemistry and Physics* 9.5 (Mar. 2009), pp. 1779–1793. ISSN: 1680-7316. DOI: https://doi.org/10.5194/acp-9-1779-2009.

[32] Roberto Paoli and Karim Shariff. “Contrail Modeling and Simulation”. In: *Annual Review of Fluid Mechanics* 48.1 (2016), pp. 393–427. DOI: 10.1146/annurev-fluid-010814-013619.

[33] S. Unterstrasser and K. Gierens. “Numerical Simulations of Contrail-to-Cirrus Transition – Part 2: Impact of Initial Ice Crystal Number, Radiation, Stratification, Secondary Nucleation and Layer Depth”. In: *Atmospheric Chemistry and Physics* 10.4 (Feb. 2010), pp. 2037–2051. ISSN: 1680-7316. DOI: 10.5194/acp-10-2037-2010.

[34] Akshat Agarwal et al. “SCOPE11 Method for Estimating Aircraft Black Carbon Mass and Particle Number Emissions”. In: *Environmental Science & Technology* 53.3 (Feb. 2019), pp. 1364–1373. ISSN: 0013-936X. DOI: 10.1021/acs.est.8b04060.

[35] Hans Hersbach et al. “The ERA5 Global Reanalysis”. en. In: *Quarterly Journal of the Royal Meteorological Society* 146.730 (2020), pp. 1999–2049. ISSN: 1477-870X. DOI: 10.1002/qj.3803.

[36] Thibaud M. Fritz et al. “The Role of Plume-Scale Processes in Long-Term Impacts of Aircraft Emissions”. English. In: *Atmospheric Chemistry and Physics* 20.9 (May 2020), pp. 5697–5727. ISSN: 1680-7316. DOI: 10.5194/acp-20-5697-2020.

[37] Eli J. Mlawer et al. “Radiative Transfer for Inhomogeneous Atmospheres: RRTM, a Validated Correlated-k Model for the Longwave”. en. In: *Journal of Geophysical Research: Atmospheres* 102.D14 (1997), pp. 16663–16682. ISSN: 2156-2202. DOI: 10.1029/97JD00237.

[38] Bingqi Yi et al. “Influence of Ice Particle Surface Roughening on the Global Cloud Radiative Effect”. EN. In: *Journal of the Atmospheric Sciences* 70.9 (Sept. 2013), pp. 2794–2807. ISSN: 0022-4928, 1520-0469. DOI: 10.1175/JAS-D-13-020.1.

[39] Chia-Pang Kuo et al. “Assessing the Accuracy and Efficiency of Longwave Radiative Transfer Models Involving Scattering Effect with Cloud Optical Property Parameterizations”. en. In: *Journal of Quantitative Spectroscopy and Radiative Transfer* 240 (Jan. 2020), p. 106683. ISSN: 0022-4073. DOI: 10.1016/j.jqsrt.2019.106683.

[40] Bethan Owen, David S. Lee, and Ling Lim. “Flying into the Future: Aviation Emissions Scenarios to 2050”. In: *Environmental Science & Technology* 44.7 (Apr. 2010), pp. 2255–2260. ISSN: 0013-936X. DOI: 10.1021/es902530z.

[41] Steve HL Yim et al. “Global, Regional and Local Health Impacts of Civil Aviation Emissions”. In: *Environmental Research Letters* 10.3 (2015), p. 034001.

[42] Akshay Ashok et al. “Development of a Response Surface Model of Aviation’s Air Quality Impacts in the United States”. In: *Atmospheric Environment* 77 (Oct. 2013), pp. 445–452. ISSN: 1352-2310. DOI: 10.1016/j.atmosenv.2013.05.023.

[43] US EPA. *The Benefits and Costs of the Clean Air Act: 1990 to 2020 Final Report of US Environmental Protection Agency Office of Air and Radiation.* 2011.

[44] WHO. *Health Risks of Particulate Matter from Long-Range Transboundary Air Pollution.* 2006.

[45] Carla Grobler et al. “Marginal Climate and Air Quality Costs of Aviation Emissions”. In: *Environmental Research Letters* 14.11 (Nov. 2019), p. 114031. ISSN: 1748-9326. DOI: 10.1088/1748-9326/ab4942.

[46] David S. Lee et al. “Aviation and Global Climate Change in the 21st Century”. In: *Atmospheric Environment* 43.22–23 (July 2009), pp. 3520–3537. ISSN: 1352-2310. DOI: 10.1016/j.atmosenv.2009.04.024.

[47] Christopher S. Dorbian, Philip J. Wolfe, and Ian A. Waitz. “Estimating the Climate and Air Quality Benefits of Aviation Fuel and Emissions Reductions”. en. In: *Atmospheric Environment* 45.16 (May 2011), pp. 2750–2759. ISSN: 1352-2310. DOI: 10.1016/j.atmosenv.2011.02.025.

[48] Joyce E. Penner et al. “Anthropogenic Aerosol Indirect Effects in Cirrus Clouds”. In: *Journal of Geophysical Research: Atmospheres* 123.20 (2018), pp. 11, 652–11, 677. ISSN: 2169-8996. DOI: 10.1029/2018JD029204.

[49] Rückerl Regina et al. “Air Pollution and Inflammation (Interleukin-6, C-Reactive Protein, Fibrinogen) in Myocardial Infarction Survivors”. In: *Environmental Health Perspectives* 115.7 (July 2007), pp. 1072–1080. DOI: 10.1289/ehp.10021.

[50] Prem Lobo et al. “Measurement of Aircraft Engine Non-Volatile PM Emissions: Results of the Aviation-Particle Regulatory Instrumentation Demonstration Experiment (A-PRIDE) 4 Campaign”. In: *Aerosol Science and Technology* 49.7 (July 2015), pp. 472–484. ISSN: 0278-6826. DOI: 10.1080/02786826.2015.1047012.

[51] Dan Bulzan et al. “Gaseous and Particulate Emissions Results of the NASA Alternative Aviation Fuel Experiment (AAFEX)”. In: (Oct. 2010), pp. 1195–1207. DOI: 10.1115/GT2010-23524.

[52] Prem Lobo et al. “PM Emissions Measurements of In-Service Commercial Aircraft Engines during the Delta-Atlanta Hartsfield Study”. en. In: *Atmospheric Environment* 104 (Mar. 2015), pp. 237–245. ISSN: 1352-2310. DOI: 10.1016/j.atmosenv.2015.01.020.

[53] M. Abegglen et al. “Effective Density and Mass–Mobility Exponents of Particulate Matter in Aircraft Turbine Exhaust: Dependence on Engine Thrust and Particle Size”. In: *Journal of Aerosol Science* 88 (Oct. 2015), pp. 135–147. ISSN: 0021-8502. DOI: 10.1016/j.jaerosci.2015.06.003.

[54] Michael T. Timko et al. “Gas Turbine Engine Emissions—Part II: Chemical Properties of Particulate Matter”. In: *Journal of Engineering for Gas Turbines and Power* 132.6 (Mar. 2010), pp. 061505-061505–15. ISSN: 0742-4795. DOI: 10.1115/1.4000132.

[55] Neelakshi Hudda et al. “Emissions from an International Airport Increase Particle Number Concentrations 4-Fold at 10 km Downwind”. In: *Environmental Science & Technology* 48.12 (June 2014), pp. 6628–6635. ISSN: 0013-936X. DOI: 10.1021/es5001566.

[56] N. Hudda and S. A. Fruin. “International Airport Impacts to Air Quality: Size and Related Properties of Large Increases in Ultrafine Particle Number Concentrations”. In: *Environmental Science & Technology* 50.7 (Apr. 2016), pp. 3362–3370. ISSN: 0013-936X. DOI: 10.1021/acs.est.5b05313.

[57] N. Hudda et al. "Aviation-Related Impacts on Ultrafine Particle Number Concentrations Outside and Inside Residences near an Airport". In: *Environmental Science & Technology* 52.4 (Feb. 2018), pp. 1765–1772. ISSN: 0013-936X. DOI: 10.1021/acs.est.7b05593.

[58] M. P. Keuken et al. "Total and Size-Resolved Particle Number and Black Carbon Concentrations in Urban Areas near Schiphol Airport (the Netherlands)". In: *Atmospheric Environment* 104 (Mar. 2015), pp. 132–142. ISSN: 1352-2310. DOI: 10.1016/j.atmosenv.2015.01.015.

[59] Steven R. H. Barrett, Rex E. Britter, and Ian A. Waitz. "Global Mortality Attributable to Aircraft Cruise Emissions". In: *Environmental Science & Technology* 44.19 (Oct. 2010), pp. 7736–7742. ISSN: 0013-936X. DOI: 10.1021/es101325r.

[60] Jamin Koo et al. "Spatial Sensitivities of Human Health Risk to Intercontinental and High-Altitude Pollution". In: *Atmospheric Environment* 71 (June 2013), pp. 140–147. ISSN: 1352-2310. DOI: 10.1016/j.atmosenv.2013.01.025.

[61] ICAO. *Annex 16: Environmental Protection, Vol. II: Aircraft Engine Emissions Third Edition*. 2008.

[62] ARP1179C. *Aircraft Gas Turbine Engine Exhaust Smoke Measurement - SAE Aerospace Recommended Practice (ARP1179C)*. 1993.

[63] Chowen C. Wey et al. "Overview on the Aircraft Particle Emissions Experiment (APEX)". In: *Journal of Propulsion and Power* 23.5 (Sept. 2007), pp. 898–905. ISSN: 0748-4658. DOI: 10.2514/1.26406.

[64] ARP6320. *Procedure for the Continuous Sampling and Measurement of Non-Volatile Particulate Matter Emissions from Aircraft Turbine Engines*. 2018.

[65] Roger L. Wayson, Gregg G. Fleming, and Ralph Iovinelli. "Methodology to Estimate Particulate Matter Emissions from Certified Commercial Aircraft Engines". In: *Journal of the Air & Waste Management Association* 59.1 (Jan. 2009), pp. 91–100. ISSN: 1096-2247. DOI: 10.3155/1047-3289.59.1.91.

[66] Marc E. J. Stettler et al. "Updated Correlation Between Aircraft Smoke Number and Black Carbon Concentration". In: *Aerosol Science and Technology* 47.11 (Nov. 2013), pp. 1205–1214. ISSN: 0278-6826. DOI: 10.1080/02786826.2013.829908.

[67] Marc E. J. Stettler et al. "Global Civil Aviation Black Carbon Emissions". en. In: *Environmental Science & Technology* 47.18 (July 2013), pp. 10397–10404. DOI: 10.1021/es401356v.

[68] AIR6504. *Procedure for the Calculation of Non-Volatile Particulate Matter Sampling and Measurement System Penetration Functions and System Loss Correction Factors - SAE Aerospace Information Report 6504 (AIR6504)*. Oct. 2017.

[69] Barouch Giechaskiel et al. “Calibration and Validation of Various Commercial Particle Number Measurement Systems”. In: *SAE International Journal of Fuels and Lubricants* 2.1 (2009), pp. 512–530. ISSN: 1946-3952.

[70] AIR6241. *Procedure for the Continuous Sampling and Measurement of Non-Volatile Particle Emissions from Aircraft Turbine Engines - SAE Aerospace Information Report 6241 (AIR6241)*. Nov. 2013.

[71] J. P. Terlouw and M. G. R. Vogelaar. *Kapteyn Package, Version 2.3*. Kapteyn Astronomical Institute. 2015.

[72] Jost Heintzenberg. “Properties of the Log-Normal Particle Size Distribution”. In: *Aerosol Science and Technology* 21.1 (Jan. 1994), pp. 46–48. ISSN: 0278-6826. DOI: 10.1080/02786829408959695.

[73] John S. Kinsey et al. “Physical Characterization of the Fine Particle Emissions from Commercial Aircraft Engines during the Aircraft Particle Emissions eXperiment (APEX) 1–3”. en. In: *Atmospheric Environment* 44.17 (June 2010), pp. 2147–2156. ISSN: 1352-2310. DOI: 10.1016/j.atmosenv.2010.02.010.

[74] Skipper Seabold and Josef Perktold. *Statsmodels: Econometric and Statistical Modeling with Python*. 2010.

[75] EASA. *ICAO Engine Emissions Databank (EDB) V24*. Nov. 2017.

[76] M. E. J. Stettler, S. Eastham, and S. R. H. Barrett. “Air Quality and Public Health Impacts of UK Airports. Part I: Emissions”. In: *Atmospheric Environment* 45.31 (Oct. 2011), pp. 5415–5424. ISSN: 1352-2310. DOI: 10.1016/j.atmosenv.2011.07.012.

[77] A. Dopelheuer and M. Lecht. “Influence of Engine Performance on Emission Characteristics”. In: *Symposium of the Applied Vehicle Technology Pane-Gas Turbine Engine Combustion, Emissions and Alternative Fuels, Lisbon, Portugal*. Citeseer, 1998.

[78] Nicholas W. Simone, Marc E. J. Stettler, and Steven R. H. Barrett. “Rapid Estimation of Global Civil Aviation Emissions with Uncertainty Quantification”. In: *Transportation Research Part D: Transport and Environment* 25 (Dec. 2013), pp. 33–41. ISSN: 1361-9209. DOI: 10.1016/j.trd.2013.07.001.

[79] Richard H. Moore et al. “Biofuel Blending Reduces Particle Emissions from Aircraft Engines at Cruise Conditions”. en. In: *Nature* 543.7645 (Mar. 2017), pp. 411–415. ISSN: 1476-4687. DOI: 10.1038/nature21420.

[80] Roger Teoh et al. “A Methodology to Relate Black Carbon Particle Number and Mass Emissions”. en. In: *Journal of Aerosol Science* 132 (June 2019), pp. 44–59. ISSN: 0021-8502. DOI: 10.1016/j.jaerosci.2019.03.006.

[81] Xiaole Zhang, Xi Chen, and Jing Wang. “A Number-Based Inventory of Size-Resolved Black Carbon Particle Emissions by Global Civil Aviation”. en. In: *Nature Communications* 10.1 (Feb. 2019), pp. 1–11. ISSN: 2041-1723. DOI: 10.1038/s41467-019-08491-9.

[82] Lisa Bock and Ulrike Burkhardt. "Reassessing Properties and Radiative Forcing of Contrail Cirrus Using a Climate Model". en. In: *Journal of Geophysical Research: Atmospheres* 121.16 (Aug. 2016), 2016JD025112. ISSN: 2169-8996. DOI: 10.1002/2016JD025112.

[83] Chih-Chieh Chen et al. "Global Contrail Coverage Simulated by CAM5 with the Inventory of 2006 Global Aircraft Emissions". en. In: *Journal of Advances in Modeling Earth Systems* 4.2 (2012). ISSN: 1942-2466. DOI: 10.1029/2011MS000105.

[84] Bingqi Yi et al. "Simulation of the Global Contrail Radiative Forcing: A Sensitivity Analysis". en. In: *Geophysical Research Letters* 39.24 (2012). ISSN: 1944-8007. DOI: 10.1029/2012GL054042.

[85] Gaby Rädel and Keith P. Shine. "Validating ECMWF Forecasts for the Occurrence of Ice Supersaturation Using Visual Observations of Persistent Contrails and Radiosonde Measurements over England". en. In: *Quarterly Journal of the Royal Meteorological Society* 136.652 (2010), pp. 1723–1732. ISSN: 1477-870X. DOI: 10.1002/qj.670.

[86] Claudia Vitolo et al. "ERA5-Based Global Meteorological Wildfire Danger Maps". en. In: *Scientific Data* 7.1 (July 2020), p. 216. ISSN: 2052-4463. DOI: 10.1038/s41597-020-0554-z.

[87] Job C. M. Dullaart et al. "Advancing Global Storm Surge Modelling Using the New ERA5 Climate Reanalysis". en. In: *Climate Dynamics* 54.1 (Jan. 2020), pp. 1007–1021. ISSN: 1432-0894. DOI: 10.1007/s00382-019-05044-0.

[88] Sebastian D. Eastham and Steven R. H. Barrett. "Aviation-Attributable Ozone as a Driver for Changes in Mortality Related to Air Quality and Skin Cancer". en. In: *Atmospheric Environment* 144 (Nov. 2016), pp. 17–23. ISSN: 1352-2310. DOI: 10.1016/j.atmosenv.2016.08.040.

[89] V. Buchard et al. "The MERRA-2 Aerosol Reanalysis, 1980 Onward. Part II: Evaluation and Case Studies". en. In: *Journal of Climate* 30.17 (Sept. 2017), pp. 6851–6872. ISSN: 0894-8755. DOI: 10.1175/JCLI-D-16-0613.1.

[90] Miguel Nogueira. "Inter-Comparison of ERA-5, ERA-Interim and GPCP Rainfall over the Last 40 Years: Process-Based Analysis of Systematic and Random Differences". en. In: *Journal of Hydrology* 583 (Apr. 2020), p. 124632. ISSN: 0022-1694. DOI: 10.1016/j.jhydrol.2020.124632.

[91] Lars Hoffmann et al. "From ERA-Interim to ERA5: The Considerable Impact of ECMWF's next-Generation Reanalysis on Lagrangian Transport Simulations". English. In: *Atmospheric Chemistry and Physics* 19.5 (Mar. 2019), pp. 3097–3124. ISSN: 1680-7316. DOI: 10.5194/acp-19-3097-2019.

[92] Yonglin Zhang et al. "Consistency Evaluation of Precipitable Water Vapor Derived From ERA5, ERA-Interim, GNSS, and Radiosondes Over China". en. In: *Radio Science* 54.7 (2019), pp. 561–571. ISSN: 1944-799X. DOI: 10.1029/2018RS006789.

[93] G. Rädel and K. P. Shine. "Evaluation of the Use of Radiosonde Humidity Data to Predict the Occurrence of Persistent Contrails". In: *Quarterly Journal of the Royal Meteorological Society* 133.627 (July 2007), pp. 1413–1423. ISSN: 0035-9009. DOI: 10.1002/qj.128.

[94] F. Immler et al. "Cirrus, Contrails, and Ice Supersaturated Regions in High Pressure Systems at Northern Mid Latitudes". In: *Atmospheric Chemistry and Physics* 8.6 (Mar. 2008), pp. 1689–1699.

[95] S. Baughcum et al. "Properties of Ice-Supersaturated Layers Based on Radiosonde Data Analysis 171". en. In: *Proceedings of the TAC-2, June 22 - 25.* 2009, pp. 169–173.

[96] N. C. Dickson et al. "Probabilistic Description of Ice-Supersaturated Layers in Low Resolution Profiles of Relative Humidity N. C. Dickson, K. Gierens, H. L. Rogers, R. L. Jones". In: *AGU Fall Meeting Abstracts* 42 (Dec. 2009), A42A–06.

[97] Larry M. Miloshevich et al. "Development and Validation of a Time-Lag Correction for Vaisala Radiosonde Humidity Measurements". EN. In: *Journal of Atmospheric and Oceanic Technology* 21.9 (Sept. 2004), pp. 1305–1327. ISSN: 0739-0572, 1520-0426. DOI: 10.1175/1520-0426(2004)021<1305:DAVOAT>2.0.CO;2.

[98] Larry M. Miloshevich et al. "Accuracy Assessment and Correction of Vaisala RS92 Radiosonde Water Vapor Measurements". en. In: *Journal of Geophysical Research: Atmospheres* 114.D11 (2009). ISSN: 2156-2202. DOI: 10.1029/2008JD011565.

[99] Nathaniel J. Livesey et al. *Version 5.0x Level 2 and 3 Data Quality and Description Document.* Tech. rep. JPL D-105336 Rev. A. Jet Propulsion Laboratory: Earth Observing System (EOS) Aura Microwave Limb Sounder (MLS), June 2020.

[100] Imke Durre et al. "Enhancing the Data Coverage in the Integrated Global Radiosonde Archive". en. In: *Journal of Atmospheric and Oceanic Technology* 35.9 (Sept. 2018), pp. 1753–1770. ISSN: 0739-0572. DOI: 10.1175/JTECH-D-17-0223.1.

[101] Imke Durre, Russell S. Vose, and David B. Wuertz. "Overview of the Integrated Global Radiosonde Archive". en. In: *Journal of Climate* 19.1 (Jan. 2006), pp. 53–68. ISSN: 0894-8755. DOI: 10.1175/JCLI3594.1.

[102] Imke Durre and Xungang Yin. "ENHANCED RADIOSONDE DATA FOR STUDIES OF VERTICAL STRUCTURE". In: *Bulletin of the American Meteorological Society* 89.9 (2008), pp. 1257–1262. ISSN: 0003-0007.

[103] R. J. Dirksen et al. "Reference Quality Upper-Air Measurements: GRUAN Data Processing for the Vaisala RS92 Radiosonde". English. In: *Atmospheric Measurement Techniques* 7.12 (Dec. 2014), pp. 4463–4490. ISSN: 1867-1381. DOI: 10.5194/amt-7-4463-2014.

[104] H. Vömel et al. “Radiation Dry Bias of the Vaisala RS92 Humidity Sensor”. en. In: *Journal of Atmospheric and Oceanic Technology* 24.6 (June 2007), pp. 953–963. ISSN: 0739-0572. DOI: 10.1175/JTECH2019.1.

[105] WMO. *Historical WMO Publication No. 9, Volume A, Observing Stations and WMO Catalogue of Radiosondes*. https://www.wmo.int/pages/prog/www/ois/volume-a/vola-hist-home.htm.

[106] David Bolton. “The Computation of Equivalent Potential Temperature”. en. In: *Monthly Weather Review* 108.7 (July 1980), pp. 1046–1053. ISSN: 0027-0644. DOI: 10.1175/1520-0493(1980)108<1046:TCOEPT>2.0.CO;2.

[107] Michele M. Rienecker et al. “MERRA: NASA’s Modern-Era Retrospective Analysis for Research and Applications”. In: *Journal of Climate* 24.14 (July 2011), pp. 3624–3648. ISSN: 0894-8755. DOI: 10.1175/JCLI-D-11-00015.1.

[108] Michael Sommer, Rudd Dirksen, and Christoph Von Rohden. *Brief Description of the RS92 GRUAN Data Product (RS92-GDP)*. Tech. rep. GRUAN-TD-4 Rev. 2.0. GRUAN Lead Center: GCOS Reference Upper Air Network (GRUAN), Feb. 2016.

[109] Ulrich Schumann. “On Conditions for Contrail Formation from Aircraft Exhausts”. en. In: *Meteorologische Zeitschrift* (Mar. 1996), pp. 4–23. ISSN: , DOI: 10.1127/metz/5/1996/4.

[110] Alan H. Epstein. “Aeropropulsion for Commercial Aviation in the Twenty-First Century and Research Directions Needed”. en. In: *AIAA Journal* (Apr. 2014). DOI: 10.2514/1.J052713.

[111] U. Schumann et al. “Dehydration Effects from Contrails in a Coupled Contrail–Climate Model”. In: *Atmos. Chem. Phys.* 15.19 (Oct. 2015), pp. 11179–11199. ISSN: 1680-7324. DOI: 10.5194/acp-15-11179-2015.

[112] *User Manual for The Base Of Aircraft Data (Bada) Revision 3.9.* Tech. rep. EEC Technical/Scientific, Report No. 11/03/08-08. Eurocontrol Experimental Center, 2011.

[113] D SONNTAG. “Important New Values of the Physical Constants of 1986, Vapour Pressure Formulations Based on the ITS-90, and Psychrometer Formulae”. In: *Important new values of the physical constants of 1986, vapour pressure formulations based on the ITS-90, and psychrometer formulae* 40.5 (1990), pp. 340–344. ISSN: 0084-5361.

[114] Christopher Roof et al. “Aviation Environmental Design Tool (AEDT) System Architecture”. In: *Doc# AEDT-AD-01* (2007).

[115] J. T. Wilkerson et al. “Analysis of Emission Data from Global Commercial Aviation: 2004 and 2006”. In: *Atmos. Chem. Phys.* 10.13 (July 2010), pp. 6391–6408. ISSN: 1680-7324. DOI: 10.5194/acp-10-6391-2010.

[116] V. Grewe et al. “Climate Impact of Supersonic Air Traffic: An Approach to Optimize a Potential Future Supersonic Fleet – Results from the EU-Project SCENIC”. In: *Atmospheric Chemistry and Physics Discussions* 7.3 (May 2007), pp. 6143–6187.

[117] Nicola Stuber et al. “The Importance of the Diurnal and Annual Cycle of Air Traffic for Contrail Radiative Forcing”. en. In: *Nature* 441.7095 (June 2006), pp. 864–867. ISSN: 0028-0836. DOI: 10.1038/nature04877.

[118] Rabindra Palikonda et al. “Contrail Coverage Derived from 2001 AVHRR Data over the Continental United States of America and Surrounding Areas”. en. In: *Meteorologische Zeitschrift* (Sept. 2005), pp. 525–536. ISSN: , DOI: 10.1127/0941-2948/2005/0051.

[119] Patrick Minnis et al. “Contrail Frequency over the United States from Surface Observations”. EN. In: *Journal of Climate* 16.21 (Nov. 2003), pp. 3447–3462. ISSN: 0894-8755, 1520-0442. DOI: 10.1175/1520-0442(2003)016<3447:CFOTUS>2.0.CO;2.

[120] Banavar Sridhar, Hok K. Ng, and Neil Y. Chen. “Aircraft Trajectory Optimization and Contrails Avoidance in the Presence of Winds”. In: *Journal of Guidance, Control, and Dynamics* 34.5 (Sept. 2011), pp. 1577–1584. DOI: 10.2514/1.53378.

[121] Yixiang Lim, Alessandro Gardi, and Roberto Sabatini. “Modelling and Evaluation of Aircraft Contrails for 4-Dimensional Trajectory Optimisation”. English. In: *SAE International Journal of Aerospace* 8.2015-01-2538 (Sept. 2015), pp. 248–259. ISSN: 1946-3855, 1946-3901. DOI: 10.4271/2015-01-2538.

[122] Klaus Gierens, Sigrun Matthes, and Susanne Rohs. “How Well Can Persistent Contrails Be Predicted?” en. In: *Aerospace* 7.12 (Dec. 2020), p. 169. DOI: 10.3390/aerospace7120169.

[123] M. Diao et al. “Cloud-Scale Ice-Supersaturated Regions Spatially Correlate with High Water Vapor Heterogeneities”. English. In: *Atmospheric Chemistry and Physics* 14.5 (Mar. 2014), pp. 2639–2656. ISSN: 1680-7316. DOI: 10.5194/acp-14-2639-2014.

[124] Junhong Wang et al. “Radiation Dry Bias Correction of Vaisala RS92 Humidity Data and Its Impacts on Historical Radiosonde Data”. en. In: *Journal of Atmospheric and Oceanic Technology* 30.2 (Feb. 2013), pp. 197–214. ISSN: 0739-0572. DOI: 10.1175/JTECH-D-12-00113.1.

[125] P. Konopka. “Analytical Gaussian Solutions for Anisotropie Diffusion in a Linear Shear Flow”. In: *Journal of Non-Equilibrium Thermodynamics* 20.1 (2009), pp. 78–91. ISSN: 1437-4358. DOI: 10.1515/jnet.1995.20.1.78.

[126] M. Z. Jacobson et al. “The Effects of Aircraft on Climate and Pollution. Part I: Numerical Methods for Treating the Subgrid Evolution of Discrete Size- and Composition-Resolved Contrails from All Commercial Flights Worldwide”. In: *Journal of Computational Physics* 230 (June 2011), pp. 5115–5132. ISSN: 0021-9991. DOI: 10.1016/j.jcp.2011.03.031.

[127] A. D. Naiman et al. “Parameterization of Subgrid Plume Dilution for Use in Large-Scale Atmospheric Simulations”. In: *Atmospheric Chemistry and Physics* 10 (Mar. 2010), pp. 2551–2560. ISSN: 1680-7316. DOI: 10.5194/acp-10-2551-2010.

[128] Jeff Gill and Jonathan Homola. “Issues in Polling Methodologies”. en. In: *The Oxford Handbook of Polling and Survey Methods*. Sept. 2018. ISBN: 9780190213299. DOI: 10.1093/oxfordhb/9780190213299.013.11.

[129] Anuja (Anuja Anil) Mahashabde. “Assessing Environmental Benefits and Economic Costs of Aviation Environmental Policy Measures”. eng. Thesis. Massachusetts Institute of Technology, 2009.

[130] George Casella and Roger L. Berger. *Statistical Inference*. en. Cengage Learning, Jan. 2021. ISBN: 978-0-357-75313-2.

[131] Official Airline Guide. *Worldwide Flight Schedule Data*. en-gb. https://www.oag.com/airline-schedules-data. 2015.

[132] S. Unterstrasser and N. Görsch. “Aircraft-Type Dependency of Contrail Evolution”. In: *Journal of Geophysical Research: Atmospheres* 119.24 (2014), pp. 14, 015–14, 027. ISSN: 2169-8996. DOI: 10.1002/2014JD022642.

[133] Petri Räisänen. “Effective Longwave Cloud Fraction and Maximum-Random Overlap of Clouds:A Problem and a Solution”. EN. In: *Monthly Weather Review* 126.12 (Dec. 1998), pp. 3336–3340. ISSN: 1520-0493, 0027-0644. DOI: 10.1175/1520-0493(1998)126<3336:ELCFAM>2.0.CO;2.

[134] H.R. Pruppacher and J.D. Klett. *Microstructure of Atmospheric Clouds and Precipitation*. Atmospheric and Oceanographic Sciences Library. Springer Netherlands, 2010. ISBN: 978-0-306-48100-0. DOI: 10.1007/978-0-306-48100-0_2.

[135] B. Kärcher. “A Trajectory Box Model for Aircraft Exhaust Plumes”. en. In: *Journal of Geophysical Research: Atmospheres* 100.D9 (1995), pp. 18835–18844. ISSN: 2156-2202. DOI: 10.1029/95JD01638.

[136] B. Kärcher et al. “Physicochemistry of Aircraft-Generated Liquid Aerosols, Soot, and Ice Particles: 2. Comparison with Observations and Sensitivity Studies”. In: *Journal of Geophysical Research: Atmospheres* 103.D14 (1998), pp. 17129–17147. ISSN: 2156-2202. DOI: 10.1029/98JD01045.

[137] Nicholas Cumpsty and Andrew Heyes. *Jet Propulsion*. en. Third edition. Cambridge University Press, July 2015. ISBN: 978-1-107-51122-4.

[138] David Gottlieb and Steven A. Orszag. *Numerical Analysis of Spectral Methods*. CBMS-NSF Regional Conference Series in Applied Mathematics. Society for Industrial and Applied Mathematics, Jan. 1977. ISBN: 978-0-89871-023-6. DOI: 10.1137/1.9781611970425.

[139] Mark Z. Jacobson. “Development and Application of a New Air Pollution Modeling System—II. Aerosol Module Structure and Design”. en. In: *Atmospheric Environment* 31.2 (Jan. 1997), pp. 131–144. ISSN: 1352-2310. DOI: 10.1016/1352-2310(96)00202-6.

[140] D. Gottlieb and J. S. Hesthaven. "Spectral Methods for Hyperbolic Problems". en. In: *Journal of Computational and Applied Mathematics*. Numerical Analysis 2000. Vol. VII: Partial Differential Equations 128.1 (Mar. 2001), pp. 83–131. ISSN: 0377-0427. DOI: 10.1016/S0377-0427(00)00510-0.

[141] Chia-Pang Kuo et al. "Assessing the Accuracy and Efficiency of Longwave Radiative Transfer Models Involving Scattering Effect with Cloud Optical Property Parameterizations". en. In: *Journal of Quantitative Spectroscopy and Radiative Transfer* 240 (Jan. 2020), p. 106683. ISSN: 0022-4073. DOI: 10.1016/j.jqsrt.2019.106683.

[142] H. W. Barker et al. "The Monte Carlo Independent Column Approximation: An Assessment Using Several Global Atmospheric Models". en. In: *Quarterly Journal of the Royal Meteorological Society* 134.635 (2008), pp. 1463–1478. ISSN: 1477-870X. DOI: 10.1002/qj.303.

[143] Lin Tian and Judith A. Curry. "Cloud Overlap Statistics". en. In: *Journal of Geophysical Research: Atmospheres* 94.D7 (1989), pp. 9925–9935. ISSN: 2156-2202. DOI: 10.1029/JD094iD07p09925.

[144] D. C. Lewellen, O. Meza, and W. W. Huebsch. "Persistent Contrails and Contrail Cirrus. Part I: Large-Eddy Simulations from Inception to Demise". In: *Journal of the Atmospheric Sciences* 71.12 (Dec. 2014), pp. 4399–4419. ISSN: 0022-4928, 1520-0469. DOI: 10.1175/JAS-D-13-0316.1.

[145] Ulrich Schumann and Kaspar Graf. "Aviation-Induced Cirrus and Radiation Changes at Diurnal Timescales". In: *Journal of Geophysical Research: Atmospheres* 118.5 (2013), pp. 2404–2421. ISSN: 2169-8996. DOI: 10.1002/jgrd.50184.

[146] Ulrich Schumann, Kaspar Graf, and Hermann Mannstein. "Potential to Reduce the Climate Impact of Aviation by Flight Level Changes". In: *3rd AIAA Atmospheric Space Environments Conference*. June 2011.

[147] Hermann Mannstein, Peter Spichtinger, and Klaus Gierens. "A Note on How to Avoid Contrail Cirrus". In: *Transportation Research Part D: Transport and Environment* 10.5 (Sept. 2005), pp. 421–426. ISSN: 1361-9209. DOI: 10.1016/j.trd.2005.04.012.

[148] Christine Fichter et al. "The Impact of Cruise Altitude on Contrails and Related Radiative Forcing". In: *Meteorologische Zeitschrift* 14.4 (Aug. 2005), pp. 563–572. DOI: 10.1127/0941-2948/2005/0048.

[149] B. Kärcher. "The Importance of Contrail Ice Formation for Mitigating the Climate Impact of Aviation". In: *Journal of Geophysical Research: Atmospheres* 121 (2016), pp. 3497–3505. ISSN: 2169-8996. DOI: 10.1002/2015JD024696.

[150] Roberto Paoli et al. "Three-Dimensional Large-Eddy Simulations of the Early Phase of Contrail-to-Cirrus Transition: Effects of Atmospheric Turbulence and Radiative Transfer". In: *Meteorologische Zeitschrift* (Dec. 2017), pp. 597–620. DOI: 10.1127/metz/2017/0764.

[151] "Major U.S. Airlines Commit to Net-Zero Carbon Emissions by 2050". In: *Airlines for America* (Mar. 30, 2021). URL: https://www.airlines.org/news/major-u-s-airlines-commit-to-net-zero-carbon-emissions-by-2050/ (visited on 04/22/2021).

[152] Michael Foust et al. "Development of the GE Aviation Low Emissions TAPS Combustor for Next Generation Aircraft Engines". In: *50th AIAA Aerospace Sciences Meeting Including the New Horizons Forum and Aerospace Exposition*. Aerospace Sciences Meetings (Jan. 2012). DOI: 10.2514/6.2012-936.

[153] Lukas Frederik Jakob Brink. "Modeling the Impact of Fuel Composition on Aircraft Engine NOx, CO and Soot Emissions". MA thesis. Massachusetts Institute of Technology, 2020.

[154] Luke Kulik. "Satellite-Based Detection of Contrails Using Deep Learning". Master's project. Department of Aeronautics and Astronautics: Massachusetts Institute of Technology, June 2019.

[155] Juris Meija et al. "Atomic Weights of the Elements 2013 (IUPAC Technical Report)". In: *Pure and Applied Chemistry* 88.3 (2016), pp. 265–291. ISSN: 0033-4545. DOI: 10.1515/pac-2015-0305.

[156] Jack Kerrebrock. *Aircraft Engines and Gas Turbines, Second Edition | The MIT Press*. en. Second. The MIT Press, 1992. ISBN: 978-0-262-11162-1.